Well-Posed Boundary Element Formulations in Electromagnetics

by

Francesco Andriulli

A dissertation submitted in partial fulfillment
of the requirements for the degree of
Doctor of Philosophy
(Electrical Engineering)
in The University of Michigan
2008

Doctoral Committee:

Professor Eric Michielssen, Chair
Professor Kamal Sarabandi
Associate Professor Divakar Viswanath
Assistant Professor Antony Grbic

Amatis meis vel Amantibus me

ACKNOWLEDGEMENTS

I would like to express my gratitude to my advisor, prof. Eric Michielssen: his support and guidance have been of great help during these years, and his scientific enthusiasm will remain as an invaluable source of inspiration in my career. I am also grateful to prof. Antony Grbic, prof. Kamal Sarabandi, and prof. Divakar Viswanath for the attention they devoted to my work by serving in my thesis committee.

Sincere thanks go to Dr. Hakan Bağcı who honored me with his friendship from the very first day of my doctoral journey. This work is greatly indebted to him who let me use his accelerated, parallel, 3D Method of Moments code, without which the numerical examples presented here would have been of a remarkably lower complexity.

For similar reasons I am thankful to Dr. Francesca Vipiana, her friendship and kindness have been very important during these years. Moreover the numerical results of Chapter V have benefited from her work since she completely recoded in FORTRAN, sensibly optimizing it, my original implementation in MATLAB of the hierarchical basis presented in this work.

I want to thank, in a special way, Kristof Cools. During all the time he spent here in Ann Arbor and every time we got in touch after that, the amount of fun we had exploring all sorts of exotic integral equations and related techniques has been remarkable. Often we got rewarded for our efforts, sometimes not, but all the work with Kristof will remain one of my happiest memories of my time here in Michigan.

Speaking about fun I feel I have to say "thank you" to Ignace Bogaert. I am very grateful for our fervent discussions on topics including, but not limited to, our common research interests and a plethora of philosophically intriguing questions, thanks Ignace.

Friends and fellow students of the Radiation Lab has been very supportive during this years and I would like to thank them all. I owe a particular acknowledgement to Onur Bakir, Karl Brakora, Joseph Brunett, Amelia Buerkle, Yuriy Goykhman, Mark Haynes, Morteza Nick, Scott Rudolph, Lora Schulwitz, Michael Thiel, Felipe Valenzuela, Wonbin Hong, and Abdulkadir Yucel.

With more than twenty years of school behind me, I desire to acknowledge all my educators. Some of them have been more inspiring than others, but I believe that all of them have left something to me. A special mention, however, goes to profs. Carla Buzano, Cristiana Grazziottin, Maria Gemma Gallino, and Ornella Robutti; thanks to them this work is not about bee's courtship rituals (which was the secret interest of my childhood that, I admit, is still somewhere in my "what to learn next" list). On the other hand, the fact that this work is about numerical electromagnetics is thanks to profs. Anita Tabacco (numerical) and Giuseppe Vecchi (electromagnetics) who, as mentors during my undergraduate studies in Torino, have channeled my interests towards this astonishingly beautiful investigation field, supporting me in my choice of specializing abroad: a sincere thank you.

All this work would not have been possible without the support and the encouragement of my family, the credit I should give to Angelo Andriulli, Carla Maria Andriulli, Carmela Guarino, Giuseppina Ricciardi, Maria Ricciardi, and Nicola Ricciardi, transcends what I could write over here.

TABLE OF CONTENTS

LIST OF FIGURES

Figure

LIST OF TABLES

Table

CHAPTER I

Background and Motivations

Computational Electromagnetics (CEM) is the scientific discipline that seeks the development and implementation of accurate and efficient Maxwell equation solvers. Maxwell's equations govern all electromagnetic theory and constitute the physical underpinnings of a plethora of electrical, electronic, communication, computer, optical, biological, and geophysical technologies. As a result, electromagnetic theory has strong predictive power and electromagnetic simulation tools are rapidly becoming indispensable in many scientific endeavors and engineering R&D settings. The advent of powerful computers encourages the development of new numerical techniques that enable the solution of electromagnetic, scattering, radiation, and guidance problems with increasing degrees of complexity and generality.

Boundary integral methods are well-suited for analyzing time harmonic and transient electromagnetic interactions with perfect electrically conducting (PEC) surfaces [28]. Indeed, they only require discretization of the scatterer surface - not the medium surrounding it - thereby resulting in (comparatively) small interaction matrices. In addition, these matrices can be applied rapidly to arbitrary vectors by means of a host of fast algorithms [41, 31, 33], thereby allowing the efficient iterative solution of the problem.

Among all integral equations proposed, the Electric Field Integral Equation (EFIE) plays a predominant role. The EFIE – by itself or linearly combined with a Magnetic Field Integral Equation (MFIE) to form a Combined Field Integral Equation (CFIE) – has been applied more than any other equation to the analysis of electromagnetic phenomena involving a vast class of geometries, both open and closed. This, together with the availability of a plethora of fast algorithms that permit the EFIE's numerical solution, explains the equation's popularity in the CEM community. However the EFIE is no panacea. In fact, the (discretized) equation is ill-conditioned in many situations of practical interest. This ill-conditioning stems for the *spatial* and the *frequency* dependency of the EFIE's spectrum.[1]

1.1 Spatial dependence of the spectrum

The EFIE operator maps a current into its radiated field and it is a fundamentally ill-posed and discontinuous operator. Intuitively, this means that properly chosen bounded and non-vanishing currents may give rise to unbounded or vanishing radiated fields. A radially oscillating current loop on a plane ($\hat{\boldsymbol{\theta}}\cos(n\rho)$ in 2D polar coordinates) is an example of a bounded current radiating an electric field which vanishes for increasing values of n, while its radially directed counterpart ($\hat{\boldsymbol{\rho}}\cos(n\rho)$) radiates an unbounded (reactive) electric field for increasing values of n. More rigorously, the EFIE is an unbounded operator that is compact on soleinoidal subspaces, which gives rise to a spectrum that accumulates at zero and infinity [36]. The EFIE is numerically solved by discretizing the geometry via a mesh (see Chapter II) and by solving the linear system obtained upon discretizing the current on this mesh and executing an appropriately chosen testing procedure. The spectral behavior of the EFIE operator translates into the linear system's matrix condition number (the

[1] In the time domain, the temporal step plays the role of the frequency. Refer to Chapters IV and V.

maximum over minimum singular value of the matrix). When the spectral resolution of the discretization increases, i.e. for denser meshes, the spectrum of the matrix better and better matches the spectrum of the continuous operator, which approaches infinity and zero. In other words, for denser discretizations the matrix condition number increases. In realistic cases the dimension of the matrix dictates that the linear system is to be solved iteratively. Since an high condition number translates into low convergence rates of iterative solvers [5], it follows that, for dense discretizations, the numerical solution of the EFIE becomes increasingly problematic. The discretization density tends to increase every time the geometry under consideration posesses roughness, singularities, or geometric features to be properly rendered by the discretization. Practical examples include the simulation of metamaterials, of fractal antennas, and of scatterers with sharp edges or tips.

1.2 Frequency dependence of the spectrum

The second source of ill conditioning for the EFIE is what in literature is known as "low-frequency breakdown" (see, for example, [57]). The electric field radiated by a current comprises vector and a scalar potential contributions[14], which are directly and inversely proportional to the frequency, respectively. Charge-free currents does not generate a scalar potential, so that the field that they radiate is vanishing small for decreasing frequencies. For all other currents, the scalar potential contribution is dominant and increasingly high for vanishing frequencies. As a consequence, a part of the EFIE spectrum will be directly proportional to the frequency while the remaining will be inversely proportional to the frequency. This can be proven in a more rigorous way by adopting a quasi-Helmholtz decomposition (such the loop-star bases) [57], and then using, for example, the Gershgorin's discs theorem [47]. As

in the previous case, the spectral behavior of the continuous EFIE operator comes over into that of the matrix of the linear system arising from the discretization. As a result, the condition number of this matrix will be increasingly high for decreasing frequencies.

1.3 Advancements proposed by this work

Problems relating to the ill-conditioned nature of the frequency domain EFIE system matrix resulting from dense discretizations, have been addressed in the past by using the Calderón identities (see Chapters II, III, and references therein). The main limitations of the existing approaches are:

- The numerical discretizations of the Calderón modified equations developed to date are not multiplicative in nature. This jeopardizes their integrability into preexisting solvers and forces the use of ad hoc discretizations/integration rules when discretizing different operator products.
- The use of Calderón techniques in CFIEs is limited to the combination of a preconditioned EFIE with a standard MFIE. This is due to the lack of identities involving CFIE operators as a whole.
- The potential use of Calderón techniques are never been explored in the time domain.

This work has investigated:

- A numerical implementation of a Calderón preconditioned EFIE that is completely multiplicative in nature, i.e. one that properly discretizes all the functional spaces involved in the integral mappings and that can be integrated, virtually effortlessly, into preexisting EM solvers. (Chapter II)

- A regularized CFIE obtained by leveraging on newly-developed integral identities including both EFIE and MFIE operators. (Chapter III)

- The use of Calderón identities in the time domain, with particular emphasis on the stability issue arising in marching on in time integral equation solvers. (Chapter IV)

The ill-conditioned nature of the EFIE system matrix for low frequencies has been addressed in the past by using quasi-Helmholtz decompositions (see Chapters V and references therein); the main drawbacks of these approaches lies in the poor spectral resolution of standard solenoidal/non-solenoidal decomposed discretizations. This work presents a new time-domain discretized EFIE leveraging properly designed wavelet spaces, aiming to increase the convergence rates of the iterative solvers with respect to the ones achievable with existing schemes. (Chapter V)

The above developments accomplished by this thesis solve many problems related to ill-posedness issues in present-day CEM solvers; as such, it represents a significative advancement in the CEM state of the art.

CHAPTER II

A Multiplicative Calderón Preconditioner for the Electric Field Integral Equation

Method of moments (MoM) based electric field integral equation (EFIE) solvers are widely used for analyzing time-harmonic electromagnetic radiation and scattering from perfect electrically conducting (PEC) surfaces [28]. These solvers' popularity stems from the fact that they only require surface discretizations, operate on (comparatively) small interaction matrices that can be applied rapidly to arbitrary vectors by using fast multipole and related algorithms [13, 31, 33], and yield solutions that automatically satisfy the radiation condition. That said, EFIE MoM solvers are no panacea. Indeed, the singular values of the EFIE operator comprise two branches, one accumulating at zero and the other at infinity [36]. The condition numbers of EFIE MoM interaction matrices therefore grow rapidly with the surface discretization density. As a result, these matrices often are ill-conditioned, thereby compromising the EFIE MoM solvers' accuracy when applied to structures with subwavelength geometric features.

The recent literature abounds with techniques for preconditioning EFIEs by leveraging Calderón identities [2, 15, 12, 8]. These techniques exploit the self-regularizing property of the EFIE, i.e. the fact that the square of the EFIE operator does not have eigenvalues accumulating at zero or infinity. Calderón preconditioned EFIEs give rise

to MoM matrices that are well-conditioned, independent of the discretization density. Unfortunately, none of the Calderón preconditioners proposed to date are easily integrated into existing MoM codes. Invariably, implementation bottlenecks can be traced to the need to construct a well-conditioned Gram matrix linking the domain and range of the EFIE operator, as is required when discretizing EFIE·EFIE. Unfortunately, when constructed using standard Rao-Wilton-Glisson basis functions, this Gram matrix is singular [12]. To overcome this problem, the EFIE operator often is split into its singular and hypersingular components and the resulting operator products, safe the square of the *continuous* hypersingular operator which vanishes, are approximated using ad hoc discretization/integration rules [2, 15]. This procedure is computationally expensive – it calls for additional matrix-vector products – and often inaccurate as the square of the *discretized* hypersingular operator typically does not vanish. Moreover, the resulting preconditioners are not multiplicative and therefore hard to integrate into existing EFIE MoM codes, in addition do not easily apply to open structures [2].

This chapter presents a Calderón multiplicative preconditioner (CMP) that is trivially integrated into existing EFIE MoM codes. The proposed CMP is rooted in the div- and quasi-curl-conforming basis proposed by Buffa and Christiansen [9] for constructing Calderón preconditioners that avoid the above pitfalls. Transformation rules linking BC and RWG basis on barycentrically refined and standard meshes are derived. Together, the BC basis and the transformation rules permit the construction of well-conditioned weighted squares of MoM-EFIE interaction matrices produced by *standard* RWG codes acting on barycentrically refined meshes. The weighting matrices comprise two sparse and readily computed transformation matrices linking standard RWG spaces on standard and barycentrically refined triangular

patch meshes, and one sparse and well-conditioned Gram matrix linking RWG and BC basis functions on a barycentrically refined triangular patch mesh. As an added advantage over existing Calderón preconditioners, the proposed preconditioner not only applies to closed structures, but (with minor modifications) to open ones as well.

2.1 Background

Let Γ and $\hat{\boldsymbol{n}}_{\boldsymbol{r}}$ denote the surface of an orientable PEC object and its outward pointing unit normal at $\boldsymbol{r}$, respectively. Assume that Γ resides in a homogeneous medium with electric permittivity ϵ and magnetic permeability μ, and is illuminated by a time-harmonic electric field $\boldsymbol{E}^i(\boldsymbol{r})$; here and in what follows a time dependence $e^{-i\omega t}$ is assumed and suppressed. The current density $\boldsymbol{J}(\boldsymbol{r})$ induced on Γ in response to $\boldsymbol{E}^i(\boldsymbol{r})$ produces the scattered field $\boldsymbol{E}^s(\boldsymbol{r})$. The components tangential to Γ of $\boldsymbol{E}^s(\boldsymbol{r})$ cancel those of $\boldsymbol{E}^i(\boldsymbol{r})$, or

$$\hat{\boldsymbol{n}}_{\boldsymbol{r}} \times \boldsymbol{E}^s = \mathcal{T}\left(\boldsymbol{J}\right) = -\hat{\boldsymbol{n}}_{\boldsymbol{r}} \times \boldsymbol{E}^i \tag{2.1}$$

where

$$\mathcal{T}(\boldsymbol{J}) = \mathcal{T}_s(\boldsymbol{J}) + \mathcal{T}_h(\boldsymbol{J}), \tag{2.2}$$

with

$$\mathcal{T}_s(\boldsymbol{J}) = i\omega\mu\, \hat{\boldsymbol{n}}_{\boldsymbol{r}} \times \int_\Gamma \frac{e^{-ik|\boldsymbol{r}-\boldsymbol{r}'|}}{4\pi\,|\boldsymbol{r}-\boldsymbol{r}'|}\boldsymbol{J}(\boldsymbol{r}')\,\mathrm{d}\boldsymbol{r}', \tag{2.3}$$

and

$$\mathcal{T}_h(\boldsymbol{J}) = -\frac{1}{i\omega\epsilon}\,\hat{\boldsymbol{n}}_{\boldsymbol{r}} \times \nabla \int_\Gamma \frac{e^{-ik|\boldsymbol{r}-\boldsymbol{r}'|}}{4\pi\,|\boldsymbol{r}-\boldsymbol{r}'|}\nabla_s \cdot \boldsymbol{J}(\boldsymbol{r}')\,\mathrm{d}\boldsymbol{r}'. \tag{2.4}$$

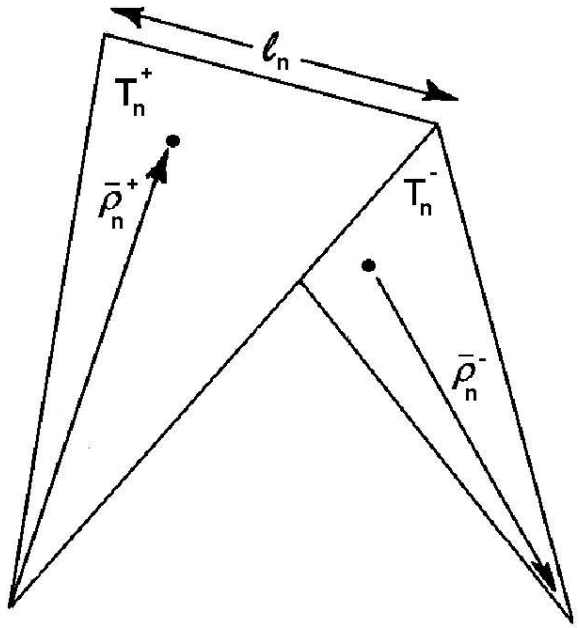

Figure 2.1: RWG basis function defined on the edge n, T^+ and T^- indicate the positive charge ($\nabla \cdot \boldsymbol{f}_n > 0$) and negative charge ($\nabla \cdot \boldsymbol{f}_n < 0$) cell respectively, l_n denotes the length of the edge.

and $k = 2\pi/\lambda = \omega\sqrt{\epsilon\mu}$. To solve EFIE (2.1) using the MoM, Γ is approximated by a mesh of planar triangles with minimum edge size δ, and $\boldsymbol{J}(\boldsymbol{r})$ is approximated as

$$\boldsymbol{J}(\boldsymbol{r}) \approx \sum_{n=1}^{N} I_n \boldsymbol{f}_n(\boldsymbol{r}) \tag{2.5}$$

where $\boldsymbol{f}_n(\boldsymbol{r})$, $n = 1, \ldots, N$ are Rao-Wilton-Glisson div-conforming basis functions defined on the mesh's N internal edges as [39] (Fig. 2.1)

$$\boldsymbol{f}_n(\boldsymbol{r}) = \begin{cases} \dfrac{l_n}{2A_n^+}\rho_n^+ & \boldsymbol{r} \in T_n^+ \\ \dfrac{l_n}{2A_n^-}\rho_n^- & \boldsymbol{r} \in T_n^- \\ 0 & \text{otherwise} \end{cases} . \tag{2.6}$$

Henceforth, X_{RWG} denotes the space spanned by these functions. To determine the expansion coefficients I_n, (2.5) is substituted into (2.1) and the resulting equation is tested with curl-conforming functions $\hat{\boldsymbol{n}}_{\boldsymbol{r}} \times \boldsymbol{f}_n$ yielding the $N \times N$ EFIE MoM system

$$\bar{\bar{\mathbf{Z}}}\,\bar{\mathbf{I}} = \bar{\mathbf{V}} \tag{2.7}$$

where

$$\left(\bar{\bar{\mathbf{Z}}}\right)_{i,j} = \left\langle \hat{\boldsymbol{n}}_{\boldsymbol{r}} \times \boldsymbol{f}_i, \mathcal{T}(\boldsymbol{f}_j) \right\rangle \tag{2.8}$$

$$\left(\bar{\mathbf{V}}\right)_i = -\left\langle \hat{\boldsymbol{n}}_{\boldsymbol{r}} \times \boldsymbol{f}_i, \hat{\boldsymbol{n}}_{\boldsymbol{r}} \times \boldsymbol{E}^i \right\rangle \tag{2.9}$$

$$\left(\bar{\mathbf{I}}\right)_j = I_j \tag{2.10}$$

Its appearance notwithstanding, (2.7) is the standard EFIE MoM system proposed in [39]. For large N, (2.7) only can be solved iteratively. Unfortunately, $\mathcal{T}$'s singular values accumulate around zero and infinity [36] and the matrix $\bar{\bar{\mathbf{Z}}}$ has a high condition number when $\delta \to 0$[1]. Under these conditions, the iterative solution of (2.7) converges very slowly [5, 40].

Since the ill-conditioning of $\bar{\bar{\mathbf{Z}}}$ is rooted in the spectral properties of $\mathcal{T}$, the above problem can be mitigated by transforming $\mathcal{T}$ into a more regular operator, e.g. by leveraging the Calderón identity [29]

$$\mathcal{T}^2(\boldsymbol{J}) = -\frac{\boldsymbol{J}}{4} + \mathcal{K}^2(\boldsymbol{J}) \tag{2.11}$$

where the operator

$$\mathcal{K}(\boldsymbol{J}) = \hat{\boldsymbol{n}}_{\boldsymbol{r}} \times \nabla \times \int_\Gamma \frac{e^{-ik|\boldsymbol{r}-\boldsymbol{r}'|}}{4\pi\,|\boldsymbol{r}-\boldsymbol{r}'|} \boldsymbol{J}(\boldsymbol{r}')\,\mathrm{d}\boldsymbol{r}' \tag{2.12}$$

is compact on smooth surfaces [36]. In other words $\mathcal{T}^2$ is a second kind operator and its spectrum accumulates at -0.25. Equation (2.11) suggests that $\mathcal{T}$ "preconditions itself" and that discretization of

$$\mathcal{T}^2(\boldsymbol{J}) = \mathcal{T}\left(-\hat{\boldsymbol{n}}_{\boldsymbol{r}} \times \boldsymbol{E}^i\right) \tag{2.13}$$

leads to well-conditioned EFIE MoM systems independently of δ. Unfortunately, the direct discretization of $\mathcal{T}^2$ is infeasible as $\mathcal{T}(\boldsymbol{f}_n)$ is not available in closed-form. That

[1] The condition number of $\bar{\bar{\mathbf{Z}}}$ is defined as the ratio of $\bar{\bar{\mathbf{Z}}}$'s largest and smallest singular values [26].

said, a variety of methods that discretize each factor in the product $\mathcal{T}^2$ using *ad hoc* integration rules and/or operatorial manipulations exists [2, 15, 8]. Unfortunately, none of them can be implemented directly starting from an implementation of (2.7). In fact, when div/curl-conforming RWGs are used to discretize the source/testing space of $\mathcal{T}$, the discretization of the operator $\mathcal{T}^2$ would require the inversion of a mixed div/curl-conforming Gram matrix $\bar{\bar{\mathbf{G}}}_{i,j} = \langle \hat{\boldsymbol{n}}_{\boldsymbol{r}} \times \boldsymbol{f}_i, \boldsymbol{f}_j \rangle$, which is singular. Recent attempts to solve this problem decompose $\mathcal{T}^2(\boldsymbol{J})$ as

$$\mathcal{T}^2(\boldsymbol{J}) = \mathcal{T}_s\mathcal{T}_s(\boldsymbol{J}) + \mathcal{T}_s\mathcal{T}_h(\boldsymbol{J}) + \mathcal{T}_h\mathcal{T}_s(\boldsymbol{J}) + \mathcal{T}_h\mathcal{T}_h(\boldsymbol{J}) \tag{2.14}$$

and discretize each product – $\mathcal{T}_h\mathcal{T}_h(\boldsymbol{J})$ which vanishes, aside (see below) – with a different technique. This procedure is problematic for the following reasons. First, it increases computational costs as additional matrix-vector products are called for. Second, it introduces additional errors since [discrete $\mathcal{T}_h\mathcal{T}_h(\boldsymbol{J})$] is set to zero even though its discretization consistent with that adopted for the other three products would have dictated [discrete $\mathcal{T}_h\mathcal{T}_h(\boldsymbol{J})$] $\neq 0$. Third and most important, it precludes the use of the original $\bar{\bar{\mathbf{Z}}}$ (or a matrix produced by a standard EFIE MoM code). These drawbacks – shared by all Calderón preconditioners developed to date – dramatically compromise these techniques's integrability into existing EFIE solvers and limit their present impact on the CEM state of the art.

2.2 A Calderón Multiplicative Preconditioner for Closed Structures

This section presents a discretization of (2.13) that explicitly uses a weighted square of $\bar{\bar{\mathbf{Z}}}$ defined in (2.8) on a properly constructed mesh; this matrix can be obtained from any pre-existing EFIE code. The weighting matrices required are highly sparse – they only contain $O(N)$ nonzero elements – and can be evaluated from simple, closed-form expressions. The proposed formulation can be trivially

integrated into existing frequency domain EFIE solvers and is easily extended to marching on in time-based EFIE solvers [21]. For simplicity the formulation in this section is restricted to uniformly discretized and closed structures (i.e. the edges in the mesh are approximately of the same length). The preconditioner extension to open structures and to nonuniform discretizations is discussed in Sections 2.3 and 2.4, respectively.

This section is organized as follows. Subsection 2.2.1 outlines the proposed preconditioning strategy. Subsection 2.2.2 proves an important inclusion relationship that permits RWG functions defined on an arbitrary triangular mesh to be expanded in terms of those defined on its barycentric refinement. Subsection 2.2.3 uses this result to obtain simple closed-from expression for all weighting matrices.

2.2.1 The preconditioner

Starting from an arbitrary mesh of planar triangles that discretize Γ - further termed the *initial mesh* - a *barycentric mesh* is obtained by adding the three medians to each triangle (Fig. 2.2). Note that a set of RWG basis functions $\boldsymbol{f}^b$ can be defined on this barycentric mesh; X^B_{RWG} will denote the space spanned by these functions. The proposed preconditioner adopts a discretization of the dual of the range of $\mathcal{T}$ on the barycentric mesh using the Buffa-Christiansen (BC) div-conforming basis functions [9]; below these basis functions will be denoted $\boldsymbol{f}_{BC}$ and the space they span will be denoted X_{BC}.

As stated before, the main problem in the discretization of $\mathcal{T}^2$ stems from the need to use div-/curl-conforming functions to discretize the source/testing space of $\mathcal{T}$ along with the fact that the determinant of the Gram matrix linking curl- and div-conforming RWGs vanishes. The latter is due to the fact that the space of N div-conforming RWGs contains a subspace of dimension approximately $N/3$ that is

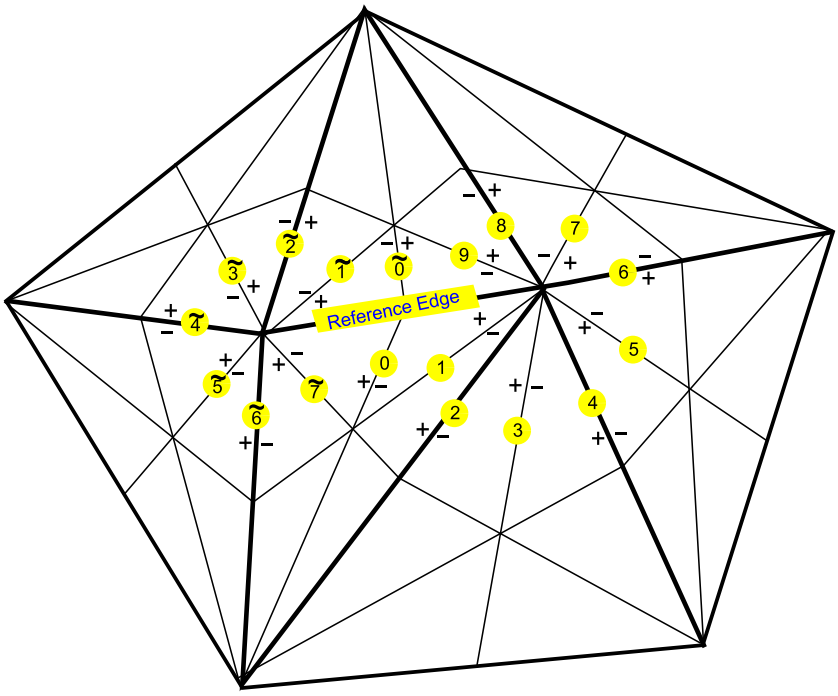

Figure 2.2: Barycentric edges used in the definition of the BC basis function associated with the reference edge. A plus/minus sign near the edge denotes a "positive/negative-charge cell" T_n^+/T_n^- for the barycentric RWG defined on the edge.

nearly orthogonal to the space of curl-conforming RWGs. The BC basis functions (which are fully described in Section 2.2.3) are defined on the edges of the initial mesh and are linear combinations of div-conforming RWGs defined on the barycentric mesh. These functions are strictly div-conforming (by construction); they also are quasi-curl-conforming in that they very much behave like curl-conforming RWGs (Figure 2.7(c)). As a consequence, the Gram matrix linking BC and curl-conforming RWGs is well-conditioned since it behaves like the Gram matrix linking curl- and curl-conforming RWGs whose condition number is notoriously low when the discretization is uniform [2]. These insights lead to the following discretization strategy for $\mathcal{T}^2$: the right operator $\mathcal{T}$ is discretized by using div-conforming RWGs $\boldsymbol{f}$ (source) and curl-conforming RWGs $\hat{\boldsymbol{n}}_{\boldsymbol{r}} \times \boldsymbol{f}$ (test), while the left operator is discretized by using div- and quasi-curl-conforming BCs $\boldsymbol{f}_{BC}$ (source) and curl- and quasi-div-conforming BCs

$\hat{\boldsymbol{n}}_{\boldsymbol{r}} \times \boldsymbol{f}_{BC}$ (test). The inverse Gram matrix between $\hat{\boldsymbol{n}}_{\boldsymbol{r}} \times \boldsymbol{f}$ and $\boldsymbol{f}_{BC}$ links the two discretizations. In other words

$$\left(\mathcal{T}^2\right)_{dis} = \bar{\bar{\mathbf{Z}}}_{BC}\ \bar{\bar{\mathbf{G}}}_m^{-1}\ \bar{\bar{\mathbf{Z}}} \tag{2.15}$$

where

$$\left(\bar{\bar{\mathbf{Z}}}\right)_{i,j} = \left\langle \hat{\boldsymbol{n}}_{\boldsymbol{r}} \times \boldsymbol{f}_i, \mathcal{T}(\boldsymbol{f}_j) \right\rangle \tag{2.16}$$

$$\left(\bar{\bar{\mathbf{Z}}}_{BC}\right)_{i,j} = \left\langle \hat{\boldsymbol{n}}_{\boldsymbol{r}} \times \boldsymbol{f}_{BCi}, \mathcal{T}(\boldsymbol{f}_{BCj}) \right\rangle \tag{2.17}$$

and

$$\left(\bar{\bar{\mathbf{G}}}_m\right)_{i,j} = \left\langle \hat{\boldsymbol{n}}_{\boldsymbol{r}} \times \boldsymbol{f}_i, \boldsymbol{f}_{BCj} \right\rangle. \tag{2.18}$$

The implementation of (2.15) can be reconducted to the computation of a single impedance matrix $\bar{\bar{\mathbf{Z}}}^b$ defined on the baricentric mesh, computable (and compressible) using standard codes. This is accomplished by using two transformation matrices $\bar{\bar{\mathbf{P}}} \in \mathbb{R}^{N^b \times N}$ and $\bar{\bar{\mathbf{R}}} \in \mathbb{R}^{N^b \times N}$ (to be defined) that express functions in X_{BC} and X_{RWG} as linear combinations of functions in X^B_{RWG}, respectively. The former set of coefficients has been derived in [9] and will be reviewed in Section 2.2.3; the latter set will be derived in Section 2.2.2. Using (2.15) and defining

$$\left(\bar{\bar{\mathbf{Z}}}^b\right)_{i,j} = \left\langle \hat{\boldsymbol{n}}_{\boldsymbol{r}} \times \boldsymbol{f}^b_i, \mathcal{T}(\boldsymbol{f}^b_j) \right\rangle \tag{2.19}$$

$$\left(\bar{\mathbf{V}}^b\right)_i = -\left\langle \hat{\boldsymbol{n}}_{\boldsymbol{r}} \times \boldsymbol{f}^b_i, \hat{\boldsymbol{n}}_{\boldsymbol{r}} \times \boldsymbol{E}^i \right\rangle, \tag{2.20}$$

$$\bar{\bar{\mathbf{Q}}} = \bar{\bar{\mathbf{P}}} \bar{\bar{\mathbf{G}}}_m^{-1} \bar{\bar{\mathbf{R}}}^T, \tag{2.21}$$

(2.13) is converted into matrix equation

$$\left(\bar{\bar{\mathbf{P}}}^T\ \bar{\bar{\mathbf{Z}}}^b\ \bar{\bar{\mathbf{Q}}}\ \bar{\bar{\mathbf{Z}}}^b\ \bar{\bar{\mathbf{R}}}\right) \bar{\mathbf{I}} = \left(\bar{\bar{\mathbf{P}}}^T\ \bar{\bar{\mathbf{Z}}}^b\ \bar{\bar{\mathbf{Q}}}\right) \bar{\mathbf{V}}^b \tag{2.22}$$

which is the proposed CMP. The vector $\bar{\bar{\mathbf{I}}} \in \mathbb{C}^N$ is the same as that appearing in (2.7), i.e. it contains expansion coefficients vector for RWGs defined on the *initial* mesh.

Closed form expressions for the elements of the (transformation and Gram) weighting matrices $\bar{\bar{\mathbf{R}}}$, $\bar{\bar{\mathbf{P}}}$, and $\bar{\bar{\mathbf{Q}}}$ will be obtained in Subsection 2.2.3. Before describing these matrices, the inclusion of the space X_{RWG} spanned by the RWGs defined on the initial mesh, and the space X^b_{RWG} spanned by RWGs on the barycentric mesh, will be proven and the coefficients that express functions of the former space as linear combinations of functions of the latter will be obtained.

2.2.2 The X_{RWG}-X^b_{RWG} Inclusion Relationship

Below it will be shown that

$$X_{RWG} \subset X^b_{RWG}. \tag{2.23}$$

The proof is constructive, that is the coefficients that realize the mapping from X^b_{RWG} to X_{RWG} will be found explicitly.

Consider an arbitrary RWG function $\boldsymbol{f} \in X_{RWG}$ defined on the initial mesh and the set $\boldsymbol{f}^B_i \in X^b_{RWG}$, $i = 1\ldots, 14$ of RWGs defined on the barycentric mesh with support *completely included* in that of $\boldsymbol{f}$ (Fig. 2.3). The function $\boldsymbol{f}$ is expressed as the linear combination

$$\boldsymbol{f} = \sum_{i=1}^{14} c_i \boldsymbol{f}^b_i. \tag{2.24}$$

Below, the scalars c_i are shown to have simple analytical expressions.

The notation adopted is the following (Fig. 2.3): cells are indexed with Greek letters, vertices are denoted by capital letters $\boldsymbol{A}$, $\boldsymbol{B}$, $\boldsymbol{C}$, $\boldsymbol{D}$, $\boldsymbol{E}$, $\boldsymbol{F}$, $\boldsymbol{G}$, $\boldsymbol{H}$, $\boldsymbol{I}$, $\boldsymbol{L}$, $\boldsymbol{M}$ (thought of as position vectors anchored to an arbitrary origin $\boldsymbol{O}$), internal edges are numbered 1 through 14, and "$\boldsymbol{x}$" denotes an arbitrary position vector (referenced w.r.t. to $\boldsymbol{O}$). Edge lengths in the barycentric mesh are denoted l_i, $i = 1, \ldots, 14$, and cell areas in the barycentric mesh are denoted A_q, $q = \alpha, \beta, \ldots, \pi$. The orientation of the barycentric RWGs is defined in Fig. 2.3 (a +/- near an edge defines a

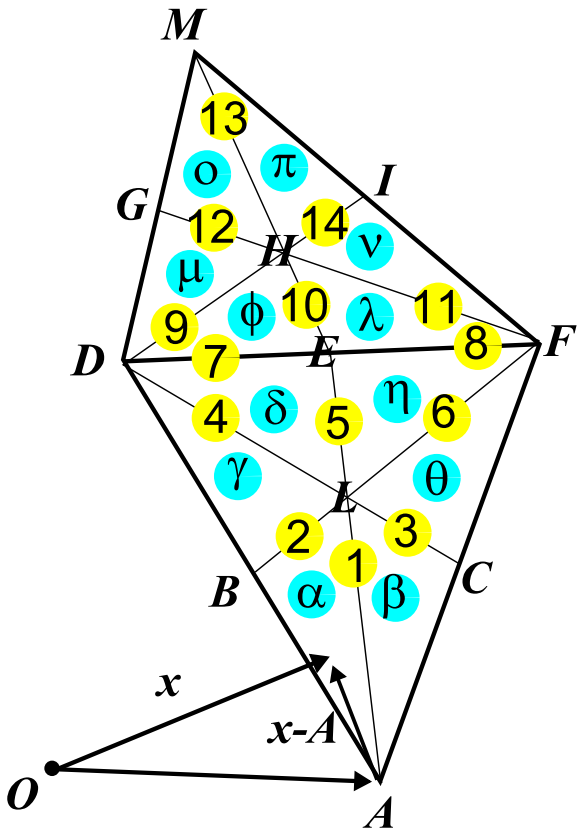

Figure 2.3: Edges of the RWGs defined on the barycentric mesh and used in the reconstruction of the RWG defined on the reference edge (7+8) of the initial mesh. A plus/minus sign near the edge denotes a "positive/negative-charge cell" T_n^+/T_n^- for the barycentric RWG defined on the edge.

"positive/negative-charge cell" T^+/T^- for the associated RWG); the RWG $\boldsymbol{f}$ defined on the initial mesh is oriented so that its + cell is the union of cells $\alpha, \beta, \gamma, \delta, \eta$, and θ. Finally define

$$A^+ = A_\alpha + A_\beta + A_\gamma + A_\delta + A_\eta + A_\theta = 6A_\alpha \tag{2.25}$$

$$A^- = A_\phi + A_\lambda + A_\mu + A_\nu + A_o + A_\pi = 6A_\phi \tag{2.26}$$

$$l = l_7 + l_8 = 2l_7 \tag{2.27}$$

The coefficients c_i, $i = 1, \ldots, 14$ will be determined by leveraging the polynomial equivalence principle [30] enforced on each cell included in the support of $\boldsymbol{f}$.

Cell α

From (2.6) the equivalence equation in cell α reads

$$-\frac{\boldsymbol{x}-\boldsymbol{A}}{A_\alpha} l_2 c_2 + \frac{\boldsymbol{x}-\boldsymbol{B}}{A_\alpha} l_1 c_1 = \frac{\boldsymbol{x}-\boldsymbol{A}}{A^+} l \quad \forall \boldsymbol{x} \in \alpha. \tag{2.28}$$

Taking $\boldsymbol{x} = \boldsymbol{A}$, it follows that

$$c_1 = 0. \tag{2.29}$$

Since $A^+ = 6A_\alpha$,

$$c_2 = -\frac{l}{A^+}\frac{A_\alpha}{l_2} = -\frac{l}{6l_2} \tag{2.30}$$

and from symmetry, it follows that

$$c_3 = \frac{l}{6l_3}, \qquad c_{13} = 0, \qquad c_{12} = -\frac{l}{6l_{12}}, \qquad c_{14} = \frac{l}{6l_{14}}. \tag{2.31}$$

Cell γ

The equivalence equation in the cell γ reads

$$\frac{\boldsymbol{x}-\boldsymbol{D}}{A_\gamma} l_2 c_2 - \frac{\boldsymbol{x}-\boldsymbol{B}}{A_\gamma} l_4 c_4 = \frac{\boldsymbol{x}-\boldsymbol{A}}{A^+} l \quad \forall \boldsymbol{x} \in \gamma. \tag{2.32}$$

Enforcing equality of the linear terms yields

$$l_2 A^+ c_2 - l_4 A^+ c_4 = l A_\gamma \tag{2.33}$$

so that

$$c_4 = -\frac{l}{A^+}\frac{A_\alpha + A_\gamma}{l_4} = -\frac{l}{3l_4}. \tag{2.34}$$

This value has to satisfy the equality of the constant terms

$$-\boldsymbol{D} l A^+ c_2 + \boldsymbol{B} l_4 A^+ c_4 = -\boldsymbol{A} l A_\gamma. \tag{2.35}$$

Substituting (2.30) and (2.34) into (2.35) yields

$$\boldsymbol{A} - \boldsymbol{B} = \boldsymbol{B} - \boldsymbol{D} \tag{2.36}$$

which is satisfied since the two vectors ($\boldsymbol{A}$-$\boldsymbol{B}$) and ($\boldsymbol{B}$-$\boldsymbol{D}$) are aligned and equal (due to the definition of median). From symmetry it follows that

$$c_6 = \frac{l}{3l_6}, \qquad c_9 = -\frac{l}{3l_9}, \qquad c_{11} = \frac{l}{3l_{11}}. \tag{2.37}$$

Cells δ, η, λ, ϕ

The equalities in these four cells give rise to the system

$$\begin{cases} -\dfrac{\boldsymbol{x}-\boldsymbol{H}}{A_\phi} l_7 c_7 + \dfrac{\boldsymbol{x}-\boldsymbol{D}}{A_\phi} l_{10} c_{10} - \dfrac{\boldsymbol{x}-\boldsymbol{E}}{A_\phi} l_9 c_9 = -\dfrac{\boldsymbol{x}-\boldsymbol{M}}{A^-} l & \forall \boldsymbol{x} \in \phi \\ \dfrac{\boldsymbol{x}-\boldsymbol{F}}{A_\eta} l_5 c_5 - \dfrac{\boldsymbol{x}-\boldsymbol{E}}{A_\eta} l_6 c_6 + \dfrac{\boldsymbol{x}-\boldsymbol{L}}{A_\eta} l_8 c_8 = \dfrac{\boldsymbol{x}-\boldsymbol{A}}{A^+} l & \forall \boldsymbol{x} \in \eta \\ \dfrac{\boldsymbol{x}-\boldsymbol{E}}{A_\delta} l_4 c_4 - \dfrac{\boldsymbol{x}-\boldsymbol{D}}{A_\delta} l_5 c_5 + \dfrac{\boldsymbol{x}-\boldsymbol{L}}{A_\delta} l_7 c_7 = \dfrac{\boldsymbol{x}-\boldsymbol{A}}{A^+} l & \forall \boldsymbol{x} \in \delta \\ -\dfrac{\boldsymbol{x}-\boldsymbol{H}}{A_\lambda} l_8 c_8 - \dfrac{\boldsymbol{x}-\boldsymbol{F}}{A_\lambda} l_{10} c_{10} + \dfrac{\boldsymbol{x}-\boldsymbol{E}}{A_\lambda} l_{11} c_{11} = -\dfrac{\boldsymbol{x}-\boldsymbol{M}}{A^-} l & \forall \boldsymbol{x} \in \lambda \end{cases}. \tag{2.38}$$

the equality of the linear terms yelds to the system

$$\begin{cases} l_7 c_7 - l_5 c_5 &= l/2 \\ l_7 c_7 - l_{10} c_{10} &= l/2 \\ l_5 c_5 + l_8 c_8 &= l/2 \\ l_8 c_8 + l_{10} c_{10} &= l/2 \end{cases} \tag{2.39}$$

which has solutions

$$c_5 = 0, \qquad c_7 = 1, \qquad c_8 = 1 \qquad c_{10} = 0. \tag{2.40}$$

The condition arising from the equality of the constant terms, obtained by substituting the values in (2.40) reads (after some manipulations)

$$\begin{cases} \boldsymbol{E} - \boldsymbol{H} &= (\boldsymbol{M} - \boldsymbol{E})/3 \\ (\boldsymbol{E} - \boldsymbol{A})/3 &= (\boldsymbol{L} - \boldsymbol{A})/2 \\ \boldsymbol{E} - \boldsymbol{L} &= (\boldsymbol{E} - \boldsymbol{A})/3 \\ (\boldsymbol{E} - \boldsymbol{M})/3 &= (\boldsymbol{H} - \boldsymbol{M})/2 \end{cases} \tag{2.41}$$

which is always satisfied in the barycentric mesh. In conclusion

$$\begin{aligned} \boldsymbol{f}(\boldsymbol{x}) &= -\frac{l}{6l_2}\boldsymbol{f}_2(\boldsymbol{x}) + \frac{l}{6l_3}\boldsymbol{f}_3(\boldsymbol{x}) - \frac{l}{3l_4}\boldsymbol{f}_4(\boldsymbol{x}) + \frac{l}{3l_6}\boldsymbol{f}_6(\boldsymbol{x}) + \boldsymbol{f}_7(\boldsymbol{x}) + \\ &\quad + \boldsymbol{f}_8(\boldsymbol{x}) - \frac{l}{3l_9}\boldsymbol{f}_9(\boldsymbol{x}) + \frac{l}{3l_{11}}\boldsymbol{f}_{11}(\boldsymbol{x}) - \frac{l}{6l_{12}}\boldsymbol{f}_{12}(\boldsymbol{x}) + \frac{l}{6l_{14}}\boldsymbol{f}_{14}(\boldsymbol{x}) \quad \forall \boldsymbol{x} \in \Gamma \end{aligned} \tag{2.42}$$

This concludes the proof.

An alternative method to obtain the coefficients in (2.42) consists of equating, on each edge of each barycentric RWG function $f_i(\boldsymbol{r})$, $i = 1, \ldots, 14$, the normal component of the RWG on the initial mesh $f(\boldsymbol{r})$ to that of (2.24). This follows from the fact that the degrees of freedom of the RWG functions are completely exhausted by the functions' normal component values evaluated on the functions' edges [9].

The validity of (2.23) enables the construction of the above-described preconditioner with weighting matrices detailed below.

2.2.3 Weighting matrices

This subsection describes the matrices $\bar{\bar{\mathbf{R}}}$, $\bar{\bar{\mathbf{P}}}$, and $\bar{\bar{\mathbf{Q}}}$ appearing in (2.22).

Matrix $\bar{\bar{\mathbf{R}}}$

As stated in Subsection 2.2.1, matrix $\bar{\bar{\mathbf{R}}}$ maps space X_{RWG} onto space X^b_{RWG}. $\bar{\bar{\mathbf{R}}}$'s column indices point to RWGs on the initial mesh, while $\bar{\bar{\mathbf{R}}}$'s row indices denote RWGs on the barycentric one. It follows that a column of $\bar{\bar{\mathbf{R}}}$ contains fourteen elements, viz the coefficients in (2.42). Note that $\bar{\bar{\mathbf{R}}}$ contains $O(N)$ elements and can be applied to a vector in $O(N)$ operations.

Matrix $\bar{\bar{\mathbf{P}}}$

The matrix $\bar{\bar{\mathbf{P}}}$ realizes the mapping between div-conforming RWGs defined on the barycentric mesh ($\boldsymbol{f} \in X^b_{RWG}$) and the div- and quasi-curl-conforming BC functions. The latter functions are linear combinations of div-conforming barycentric RWGs in X^b_{RWG}, but are associated with edges of the initial mesh (so that in number they equal the number of RWGs on the initial mesh). The BC are basis functions quasi-curl-conforming in the sense that the Gram matrix linking the BC basis functions and the curl-conforming RWGs defined on the initial mesh ($\hat{\boldsymbol{n}}_{\boldsymbol{r}} \times \boldsymbol{f}$, with $\boldsymbol{f} \in X_{RWG}$) is well-conditioned [9]. The coefficients that express the BC functions as linear combinations of RWGs on the barycentric mesh have been obtained in [9]; they will be reviewed here for the sake of completeness.

One BC function is associated with each edge of the initial mesh (the "reference edge" Fig. 2.2, below the conventions of Fig. 2.3 are re-used). Assume an orientation for the reference edge, i.e. define the "right" and the "left" vertices of the edge,

(note that since in this section the structure is assumed closed, both these vertices are internal to the mesh). Denote by N_c the number of cells of the initial mesh that have the "right" vertex among their vertices; in Fig. 2.2, $N_c = 5$. Similarly define $\tilde{N}_c$ for the "left" vertex; in Fig. 2.2 $\tilde{N}_c = 4$. Label the barycentric edges as in Fig. 2.2: $1, 2, \ldots, 2N_c - 1$ on the right and $\tilde{1}, \tilde{2}, \ldots, 2\tilde{N}_c - 1$ on the left. The two barycentric RWGs in the middle will be labelled 0 and $\tilde{0}$ (Fig. 2.2). The coefficients of the rightmost RWGs are

$$c_i = \frac{N_c - i}{2l_i N_c} \quad i = 1, \ldots, 2N_c - 1 \tag{2.43}$$

while those for the leftmost RWGs are

$$c_{\tilde{i}} = -\frac{\tilde{N}_c - \tilde{i}}{2l_{\tilde{i}}\tilde{N}_c} \quad i = 1, \ldots, 2\tilde{N}_c - 1. \tag{2.44}$$

The RWGs 0 and $\tilde{0}$ have coefficients $1/2l_0$ and $-1/2l_{\tilde{0}}$ respectively.

In the example of Fig. 2.2

$$\begin{array}{lllllll} c_0 = \dfrac{1}{2l_0} & c_1 = \dfrac{4}{10l_1} & c_2 = \dfrac{3}{10l_2} & c_3 = \dfrac{2}{10l_3} & c_4 = \dfrac{1}{10l_4} & c_5 = 0 & \\ c_6 = -\dfrac{1}{10l_6} & c_7 = -\dfrac{2}{10l_7} & c_8 = -\dfrac{3}{10l_8} & c_9 = -\dfrac{4}{10l_9} & c_{\tilde{0}} = -\dfrac{1}{2l_{\tilde{0}}} & c_{\tilde{1}} = -\dfrac{3}{8l_{\tilde{1}}} & \\ c_{\tilde{2}} = -\dfrac{2}{8l_{\tilde{2}}} & c_{\tilde{3}} = -\dfrac{1}{8l_{\tilde{3}}} & c_{\tilde{4}} = 0 & c_{\tilde{5}} = \dfrac{1}{8l_{\tilde{5}}} & c_{\tilde{6}} = \dfrac{2}{8l_{\tilde{6}}} & c_{\tilde{7}} = \dfrac{3}{8l_{\tilde{7}}}. & \end{array} \tag{2.45}$$

Column indices of the matrix $\bar{\bar{\mathbf{P}}}$ point to BC functions defined on the edges of the initial mesh, while its row indices denote RWGs on the barycentrically refined mesh. Thus a column of $\bar{\bar{\mathbf{P}}}$ contains the coefficients in (2.43) and (2.44). Note that, similar to $\bar{\bar{\mathbf{R}}}$, $\bar{\bar{\mathbf{P}}}$ also can be applied to a vector in $O(N)$ operations.

Consider the three BC basis functions $\boldsymbol{f}_{BCi}$, $i = 1 \ldots 3$, defined by the three reference edges of a cell of the standard mesh and oriented counterclockwise. From the definition of the coefficients in (2.45) it is easy to see that the function

$$\boldsymbol{f}_s = \sum_{i=1}^{3} \boldsymbol{f}_{BCi} \tag{2.46}$$

is solenoidal, i.e. $\nabla_s \cdot \boldsymbol{f}_s = 0$. Note that the function $\boldsymbol{f}_s$ is defined in the way the (non-solenoidal) "star" basis functions are defined for standard RWGs [48]. In other words the space of the div-conforming BC basis functions has a solenoidal subspace associated with the cells of the mesh. This situation is dual with respect to the standard div-conforming RWG space that has a solenoidal subspace associated with the nodes of the mesh (via the "loop" basis functions [48]). As detailed in [16], this property enables the above mentioned cancelation of the square of the discretized hypersingular operator.

Matrix $\bar{\bar{\mathbf{Q}}}$

The matrix $\bar{\bar{\mathbf{Q}}}$ maps the space of the curl-conforming RWGs (the dual of the range of $\mathcal{T}$) into the space of the div-conforming RWGs X^b_{RWG} (the domain of $\mathcal{T}$). From the definition in (2.18) it is easy to see that

$$\bar{\bar{\mathbf{G}}}_m = \left(\bar{\bar{\mathbf{R}}}^T \bar{\bar{\mathbf{G}}} \bar{\bar{\mathbf{P}}}\right) \tag{2.47}$$

where $\bar{\bar{\mathbf{G}}} \in \mathbb{R}^{N^b \times N^b}$ is the mixed Gram matrix linking div- and curl-conforming RWGs defined on the barycentric mesh

$$\bar{\bar{\mathbf{G}}}_{i,j} = \int_\Gamma \hat{\boldsymbol{n}}_{\boldsymbol{r}} \times \boldsymbol{f}^b_i(\boldsymbol{r}) \cdot \boldsymbol{f}^b_i(\boldsymbol{r})\, \mathrm{d}\boldsymbol{r}. \tag{2.48}$$

Consequently

$$\bar{\bar{\mathbf{Q}}} = \bar{\bar{\mathbf{P}}} \left(\bar{\bar{\mathbf{R}}}^T \bar{\bar{\mathbf{G}}} \bar{\bar{\mathbf{P}}}\right)^{-1} \bar{\bar{\mathbf{R}}}^T. \tag{2.49}$$

The integral in (2.48) can be computed analytically and $\bar{\bar{\mathbf{G}}}$ contains $O(N)$ elements. The inversion in (2.49) is never carried out explicitly; rather, the required matrix-vector product is effected via iterative solution of the system

$$\left(\bar{\bar{\mathbf{R}}}^T \bar{\bar{\mathbf{G}}} \bar{\bar{\mathbf{P}}}\right) \bar{\mathbf{x}} = \bar{\mathbf{y}}, \tag{2.50}$$

which can be effected in $O(N)$ operations, since $\bar{\bar{\mathbf{P}}}$, $\bar{\bar{\mathbf{G}}}$ and $\bar{\bar{\mathbf{R}}}$ are sparse and the condition number (and so the convergence rate of the iterative solver) of the Gram matrix $\bar{\bar{\mathbf{G}}}_m$ is independent of the number of unknowns [9] and is low for uniform discretizations (simple modifications are required for the treatment of nonuniform discretizations, see Section 2.4). In other words, the matrix $\bar{\bar{\mathbf{Q}}}$ can be applied to a vector in $O(N)$ operations.

2.2.4 Computational cost

The computational cost of solving the preconditioned equation (2.22) is that of multiplying the matrix in the LHS of (2.22) times the number of iterations. As mentioned previously, the cost of multiplying $\bar{\bar{\mathbf{R}}}$, $\bar{\bar{\mathbf{P}}}$, and $\bar{\bar{\mathbf{Q}}}$ by a vector scales as $O(N)$. Using the Multilevel Fast Multipole Method [13], the cost of multiplying $\bar{\bar{\mathbf{Z}}}^b$ by a vector scales as $C_Z + O(N)$ where C_Z is the cost of multiplying the initial mesh impedance matrix $\bar{\bar{\mathbf{Z}}}$ in (2.7) by a vector. Indeed, even though the dimension of $\bar{\bar{\mathbf{Z}}}^b$ is greater than that of $\bar{\bar{\mathbf{Z}}}$ by a factor 6, the additional degrees of freedom introduced in the barycentric mesh do not change the number of multipoles required for field expansion compared to that used when multiplying $\bar{\bar{\mathbf{Z}}}$. For this reason the cost of multiplying $\bar{\bar{\mathbf{Z}}}^b$ increases only by an *additive* linear term. It follows that the overall computational cost of solving (2.22) is

$$C_{TOT}^{CMP} = N_{it}^{CMP} \left(2C_Z + O(N)\right) \tag{2.51}$$

with N_{it}^{CMP} being the number of iterations necessary to achieve the convergence using the CMP. This cost should be compared to that of solving the standard system (2.7), viz.

$$C_{TOT} = N_{it} C_Z \tag{2.52}$$

where N_{it} is the number of iterations necessary to achieve the convergence without using the CMP. Since $N_{it}^{CMP} << N_{it}$, it follows that $C_{TOT} >> C_{TOT}^{CMP}$ justifying the use of the CMP.

2.3 A Calderón Multiplicative Preconditioner for Open Structures

This section extends the formulation of Section 2.2 to open Γ. This is possible since, although (2.11) is valid for closed Γ only, the decomposition (2.14) and the condition $\mathcal{T}_h^2 = 0$ hold true for both open and closed structures.

Section 2.2.1 applies to open Γ without modification. The sole difference between open and closed Γ arises in the definition of the BC functions. The proper definition of the BC functions and construction of the $\bar{\bar{\mathbf{P}}}$ matrix for open Γ is discussed first. Ramifications on the construction of the $\bar{\bar{\mathbf{Z}}}^b$, $\bar{\bar{\mathbf{R}}}$, and $\bar{\bar{\mathbf{Q}}}$ matrices are discussed thereafter.

As is customary, for open Γ, RWG basis are only associated with internal initial mesh edges; no degrees of freedom in the form of non-divergence-conforming half-RWG functions are associated with initial mesh boundary edges. The same holds true for the BC functions; it follows that for open Γ the number of RWG functions continues to equal the number of BC functions. Moreover, the construction of BC functions for edges having no node in common with the Γ's boundary proceeds as explained in Section 2.2.3. It is clear that the definition of the BC basis functions in Section 2.2.3 cannot apply to BC functions for edges sharing one or two vertices with Γ's boundary. For such edges, the BC functions need to be redefined. Contrary to RWG functions on open Γ, these BC functions do incorporate half-barycentric-RWGs associated with the barycentric mesh boundary edges. The coefficients of the barycentric full- and half-RWGs will be defined so as to ensure that, even in the

presence of the boundary, the BC basis functions still give rise to solenoidal functions when linearly combined around a cell as in (2.46). As stated above, this condition is necessary to ensure the cancelation of the square of the discretized hypersingular operator.

When the reference edge of a BC function incorporates one boundary vertex, then assume the edge is oriented so that the "right" vertex is on the boundary (Fig. 2.4). Let N_c denote the number of initial mesh cells that incorporate the right vertex; in Fig. 2.4, $N_c = 4$. Label the barycentric mesh edges incorporating the right vertex 1 through $2N_c + 1$, counterclockwise from the upper barycentric mesh boundary edge to the lower one; the two boundary edges are included in the labeling since two half-RWGs are associated with them. Let N_{ref} denote the edge of the barycentric mesh that coincides with the right half of the reference edge; in Fig. 2.4, $N_{ref} = 5$. Let $\tilde{N}_c$ denote the number of cells of the initial mesh that incorporate the left vertex; in Fig. 2.4, $\tilde{N}_c = 6$. Label the edges of the barycentric mesh incorporating the left vertex $\tilde{1}$ through $2\tilde{N}_c+1$, counterclockwise from the barycentric mesh edge just above the reference edge to the one just below. The two barycentric RWGs in the middle are labeled 0 and $\tilde{0}$ (Fig. 2.4). The BC function associated with the reference edge

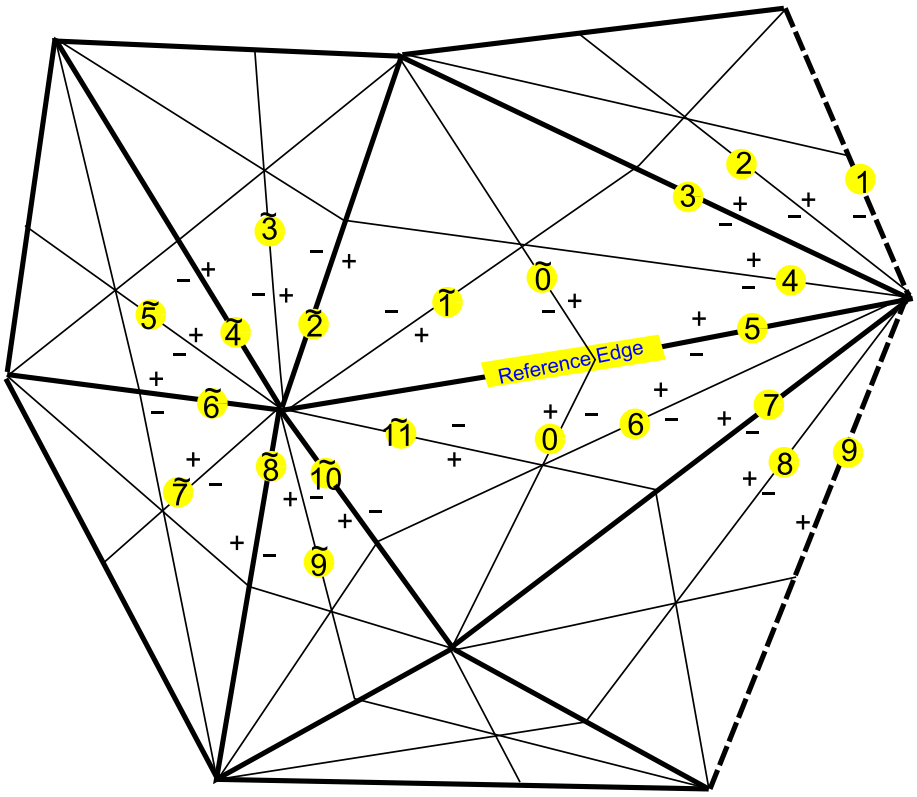

Figure 2.4: Barycentric edges used in the definition of the BC function when the reference edge has one vertex on the boundary. The hatched line denotes the boundary. A plus/minus sign near the edge denotes a "positive/negative-charge cell" T_n^+/T_n^- for the barycentric RWG defined on the edge. Note the presence of two half RWGs (labeled 1 and 9) defined on two boundary barycentric edges. A plus sign near a boundary barycentric edge indicates that the corresponding half-RWG follows the definition in (2.57), a minus sign indicates that the function defined in (2.57) has to be multiplied by -1.

comprises barycentric RWGs with coefficients

$$
\begin{aligned}
c_i &= \begin{cases} \dfrac{1-N_c}{l_i N_c} & i < N_{ref} \\ \dfrac{2-N_c}{2l_i N_c} & i = N_{ref} \\ \dfrac{1}{l_i N_c} & i > N_{ref} \end{cases} \qquad i = 1, \ldots, 2N_c + 1 \\
c_{\tilde{i}} &= -\frac{\tilde{N}_c - \tilde{i}}{2l_{\tilde{i}}\tilde{N}_c} \qquad\qquad i = 1, \ldots, 2\tilde{N}_c - 1 \\
c_0 &= \frac{1}{2l_0}, \\
c_{\tilde{0}} &= -\frac{1}{2l_{\tilde{0}}}.
\end{aligned}
\tag{2.53}
$$

In the example of Fig. 2.4,

$$
\begin{array}{lllll}
c_0 = \dfrac{1}{2l_0} & c_1 = -\dfrac{3}{4l_1} & c_2 = -\dfrac{3}{4l_2} & c_3 = -\dfrac{3}{4l_3} & c_4 = -\dfrac{3}{4l_4} \quad c_5 = -\dfrac{1}{4l_5} \\
c_6 = \dfrac{1}{4l_6} & c_7 = \dfrac{1}{4l_7} & c_8 = \dfrac{1}{4l_8} & c_9 = \dfrac{1}{4l_9} & c_{\tilde{0}} = -\dfrac{1}{2l_{\tilde{0}}} \quad c_{\tilde{1}} = -\dfrac{5}{12l_{\tilde{1}}} \\
c_{\tilde{2}} = -\dfrac{4}{12l_{\tilde{2}}} & c_{\tilde{3}} = -\dfrac{3}{12l_{\tilde{3}}} & c_{\tilde{4}} = -\dfrac{2}{12l_{\tilde{4}}} & c_{\tilde{5}} = -\dfrac{1}{12l_{\tilde{5}}} & c_{\tilde{6}} = 0 \quad c_{\tilde{7}} = \dfrac{1}{12l_{\tilde{7}}} \\
c_{\tilde{8}} = \dfrac{2}{12l_{\tilde{8}}} & c_{\tilde{3}} = \dfrac{3}{12l_{\tilde{9}}} & c_{\tilde{4}} = \dfrac{4}{12l_{\tilde{1}\tilde{0}}} & c_{\tilde{1}\tilde{1}} = \dfrac{5}{12l_{\tilde{1}\tilde{1}}}. &
\end{array}
\tag{2.54}
$$

When the reference edge of a BC function incorporates two boundary vertices, let N_c ($\tilde{N}_c$) denote the number of initial mesh cells that incorporate its right (left) vertex; in Fig. 2.5, $N_c = 4$ ($\tilde{N}_c = 3$). Label the barycentric mesh edges that incorporate the right (left) vertex 1 through $2N_c + 1$ ($2\tilde{N}_c + 1$), counterclockwise from one boundary edge to the other; the two boundary edges are included since two half-barycentric mesh RWGs are associated with them. Let N_{ref} ($\tilde{N}_{ref}$) denote the edge of the barycentric mesh that coincides with the right (left) half of the reference edge; in Fig. 2.5 $N_{ref} = 7$ ($\tilde{N}_{ref} = \tilde{3}$). The two barycentric RWGs in the center are labeled

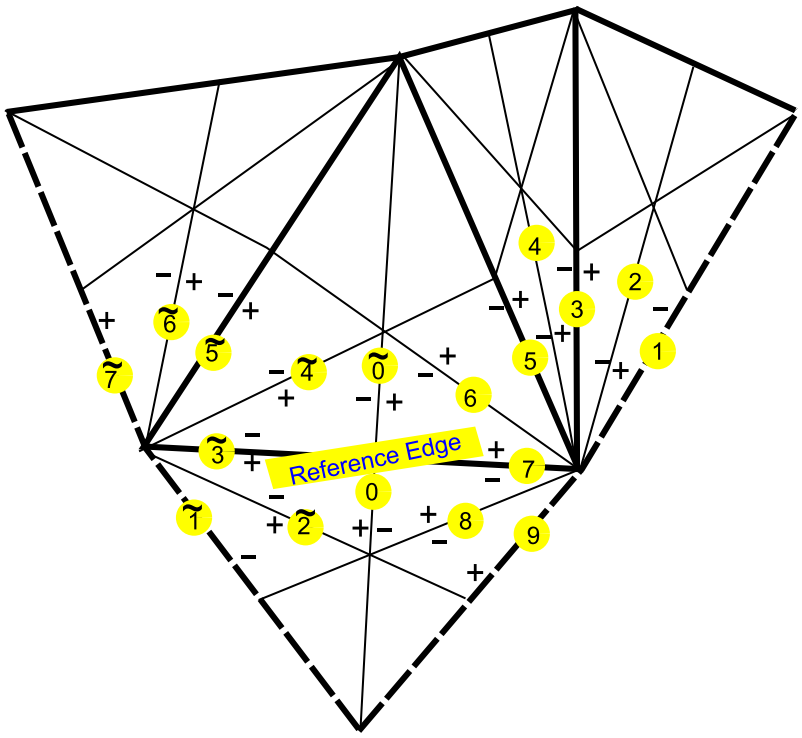

Figure 2.5: Barycentric edges used in the definition of the BC function when the reference edge has two vertices on the boundary. The hatched line denotes the boundary. A plus/minus sign near the edge denotes a "positive/negative-charge cell" T_n^+/T_n^- for the barycentric RWG defined on the edge. Note the presence of four half RWGs (labeled $1, 9, \tilde{1}, \tilde{7}$) defined on four boundary barycentric edges. A plus sign near a boundary barycentric edge indicates that the corresponding half-RWG follows the definition in (2.57), a minus sign indicates that the function defined in (2.57) has to be multiplied by -1.

0 and $\tilde{0}$ (Fig. 2.5). The BC function associated with the reference edge comprises

barycentric RWGs with coefficients

$$c_i = \begin{cases} \dfrac{1-N_c}{l_i N_c} & i < N_{ref} \\ \dfrac{2-N_c}{2l_i N_c} & i = N_{ref} \\ \dfrac{1}{l_i N_c} & i > N_{ref} \end{cases}, \quad i = 1, \ldots, 2N_c + 1$$

$$c_{\tilde{i}} = \begin{cases} -\dfrac{1-\tilde{N}_c}{l_{\tilde{i}} \tilde{N}_c} & \tilde{i} < \tilde{N}_{ref} \\ -\dfrac{2-\tilde{N}_c}{2l_{\tilde{i}} \tilde{N}_c} & \tilde{i} = \tilde{N}_{ref} \\ -\dfrac{1}{l_{\tilde{i}} \tilde{N}_c} & \tilde{i} > \tilde{N}_{ref} \end{cases}, \quad \tilde{i} = 1, \ldots, 2\tilde{N}_c + 1 \tag{2.55}$$

$$c_0 = \frac{1}{2l_0},$$

$$c_{\tilde{0}} = -\frac{1}{2l_{\tilde{0}}}.$$

In the example of Fig. 2.5

$$\begin{array}{lllllll} c_0 = \dfrac{1}{2l_0} & c_1 = -\dfrac{3}{4l_1} & c_2 = -\dfrac{3}{4l_2} & c_3 = -\dfrac{3}{4l_3} & c_4 = -\dfrac{3}{4l_4} & c_5 = -\dfrac{3}{4l_5} \\ c_6 = -\dfrac{3}{4l_6} & c_7 = -\dfrac{1}{4l_7} & c_8 = \dfrac{1}{4l_8} & c_9 = \dfrac{1}{4l_9} & c_{\tilde{0}} = -\dfrac{1}{2l_{\tilde{0}}} & c_{\tilde{1}} = \dfrac{2}{3l_{\tilde{1}}} \\ c_{\tilde{2}} = \dfrac{2}{3l_{\tilde{2}}} & c_{\tilde{3}} = \dfrac{1}{6l_{\tilde{3}}} & c_{\tilde{4}} = -\dfrac{1}{3l_{\tilde{4}}} & c_{\tilde{5}} = -\dfrac{1}{3l_{\tilde{5}}} & c_{\tilde{6}} = -\dfrac{1}{3l_{\tilde{6}}} & c_{\tilde{7}} = -\dfrac{1}{3l_{\tilde{7}}}. \end{array} \tag{2.56}$$

The half-RWG functions alluded to before are defined as (Fig. 2.6):

$$\boldsymbol{f}_b^{half}(\boldsymbol{r}) = \begin{cases} \dfrac{l_b}{2A_b}\rho_b & \boldsymbol{r} \in T_b \\ 0 & \text{otherwise} \end{cases}. \tag{2.57}$$

As the redefined BC functions incorporate half-RWGs on the barycentric mesh, matrix $\bar{\bar{\mathbf{Z}}}^b$ needs to account for them; the dimension of $\bar{\bar{\mathbf{Z}}}^b$ thus equals the total number of barycentric mesh edges (including the boundary edges). In the open

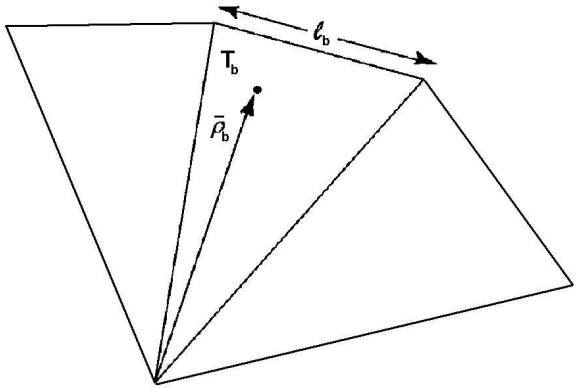

Figure 2.6: Half RWG function defined on the cell T_b of area A_b and associated with the boundary edge b of length l_b.

structure case the CMP equation (2.22) remains formally the same. The $\bar{\bar{\mathbf{R}}}$ and $\bar{\bar{\mathbf{Q}}}$ matrices remain defined as in the closed structure case. Since there are no half-RWGs associated with the initial mesh, and since every RWG defined on an internal edge of the initial mesh can be written as a linear combination of barycentric full-RWGs only (no barycentric half-RWGs are necessary), the $\bar{\bar{\mathbf{R}}}$ matrix for open Γ contains rows of zeros with indices corresponding to columns of $\bar{\bar{\mathbf{Z}}}^b$ pointing to barycentric half-RWGs. The mixed Gram matrix $\bar{\bar{\mathbf{G}}}$, required in the definition of $\bar{\bar{\mathbf{Q}}}$, now has additional rows and columns due to the presence of half-RWGs. It can easily be obtained, like in the closed structure case, from analytic expressions.

2.4 Nonuniform Discretization Densities

In most practical cases, it is necessary to deal with discretizations that are not only dense, but also nonuniform. This often happens when analyzing electrically large objects with localized fine geometric features. In this case the discretization of this region can be orders of magnitude denser than that on the rest of the structure. Under these circumstances, minor modifications are required to the method presented in Sections 2.2 and 2.3.

The spectrum of the matrix

$$\left(\bar{\bar{\mathbf{G}}}_m^T\right)^{-1} \bar{\bar{\mathbf{Z}}}_{BC}\ \bar{\bar{\mathbf{G}}}_m^{-1}\ \bar{\bar{\mathbf{Z}}}, \tag{2.58}$$

where

$$\left(\bar{\bar{\mathbf{G}}}_m^T\right)_{i,j} = \left(\bar{\bar{\mathbf{G}}}_m\right)_{j,i} = \left\langle \hat{\boldsymbol{n}}_{\boldsymbol{r}} \times \boldsymbol{f}_j, \boldsymbol{f}_{BCi} \right\rangle = -\left\langle \hat{\boldsymbol{n}}_{\boldsymbol{r}} \times \boldsymbol{f}_{BCi}, \boldsymbol{f}_j \right\rangle . \tag{2.59}$$

converges to the spectrum of the operator $\mathcal{T}^2$ in (2.11) (as the leftmost Gram matrix restores the orthonormality between the source and test functions) and thus the matrix is well-conditioned for both uniform and nonuniform discretizations. We may obtain the desired modification to the CMP for nonuniform discretizations using (2.58) instead of (2.15). Fortunately the inversion of $\bar{\bar{\mathbf{G}}}_m^T$ is not really necessary. In fact, consider a non singular matrix $\bar{\bar{\mathbf{Y}}} \in \mathbb{R}^{N\times N}$; a simple property of condition numbers ensures that [26]

$$\begin{aligned} k\left(\bar{\bar{\mathbf{Y}}}\bar{\bar{\mathbf{Z}}}_{BC}\ \bar{\bar{\mathbf{G}}}_m^{-1}\ \bar{\bar{\mathbf{Z}}}\right) &= k\left(\bar{\bar{\mathbf{Y}}}\bar{\bar{\mathbf{G}}}_m^T\left(\bar{\bar{\mathbf{G}}}_m^T\right)^{-1}\bar{\bar{\mathbf{Z}}}_{BC}\ \bar{\bar{\mathbf{G}}}_m^{-1}\ \bar{\bar{\mathbf{Z}}}\right) < \\ &< k\left(\bar{\bar{\mathbf{Y}}}\bar{\bar{\mathbf{G}}}_m^T\right) k\left(\left(\bar{\bar{\mathbf{G}}}_m^T\right)^{-1}\bar{\bar{\mathbf{Z}}}_{BC}\ \bar{\bar{\mathbf{G}}}_m^{-1}\ \bar{\bar{\mathbf{Z}}}\right). \end{aligned} \tag{2.60}$$

This implies that the matrix $\bar{\bar{\mathbf{Y}}}\bar{\bar{\mathbf{Z}}}_{BC}\ \bar{\bar{\mathbf{G}}}_m^{-1}\ \bar{\bar{\mathbf{Z}}}$ is well-conditioned provided that the matrix $\bar{\bar{\mathbf{Y}}}\bar{\bar{\mathbf{G}}}_m^T$ is well-conditioned. In the case of a uniform discretization the matrix $\bar{\bar{\mathbf{G}}}_m$ (and thus $\bar{\bar{\mathbf{G}}}_m^T$) is provably well-conditioned [9] and thus $\bar{\bar{\mathbf{Y}}}$ can be set equal to the identity. This justifies the use of (2.15) in the case of uniform discretizations. In the case of nonuniform discretizations, however, the (nearly diagonal) matrix $\bar{\bar{\mathbf{G}}}_m$ has an ill-scaled diagonal and thus tends to be increasingly ill-conditioned as the ratio between the maximum and minimum mesh edge length increases. This problem can be simply solved by diagonally preconditioning $\bar{\bar{\mathbf{G}}}_m$, i.e. by setting

$$\left(\bar{\bar{\mathbf{Y}}}\right)_{i,j} = \left(\bar{\bar{\mathbf{D}}}\right)_{i,j} = \begin{cases} \dfrac{1}{\left(\bar{\bar{\mathbf{G}}}_m\right)_{i,j}} & i = j \\ 0 & \text{otherwise} \end{cases} . \tag{2.61}$$

In other words, $\bar{\bar{\mathbf{D}}}\bar{\bar{\mathbf{G}}}_m$ (and so $\bar{\bar{\mathbf{D}}}\bar{\bar{\mathbf{G}}}_m^T$) is well-conditioned and thus (2.60) implies that

$$\bar{\bar{\mathbf{D}}}\ \bar{\bar{\mathbf{Z}}}_{BC}\ \bar{\bar{\mathbf{G}}}_m^{-1}\ \bar{\bar{\mathbf{Z}}} \tag{2.62}$$

is a well-conditioned matrix. Following the steps that turn (2.15) into (2.22), it follows that the CMP equation (2.22) should be modified to

$$\bar{\bar{\mathbf{D}}}\left(\bar{\bar{\mathbf{P}}}^T\ \bar{\bar{\mathbf{Z}}}^b\ \bar{\bar{\mathbf{Q}}}\ \bar{\bar{\mathbf{Z}}}^b\ \bar{\bar{\mathbf{R}}}\right)\bar{\mathbf{I}} = \bar{\bar{\mathbf{D}}}\left(\bar{\bar{\mathbf{P}}}^T\ \bar{\bar{\mathbf{Z}}}^b\ \bar{\bar{\mathbf{Q}}}\right)\bar{\mathbf{V}}^b \tag{2.63}$$

to be well-conditioned for both uniform and nonuniform discretizations (in fact (2.63) becomes equivalent to (2.22) when the discretization is uniform since $\bar{\bar{\mathbf{D}}}$ is approximately equal to the identity matrix multiplied by a scalar).

The matrix $\bar{\bar{\mathbf{D}}}$ is simply the inverse of the matrix $\left(\bar{\bar{\mathbf{R}}}^T\bar{\bar{\mathbf{G}}}\bar{\bar{\mathbf{P}}}\right)$'s diagonal in (2.47) and can be computed in $O(N)$ operations since the matrices $\bar{\bar{\mathbf{R}}}^T$, $\bar{\bar{\mathbf{G}}}$, and $\bar{\bar{\mathbf{P}}}$ have a constant number of elements on every row and on every column. The definition and the computation of the other matrices required by (2.63) remains unchanged from the ones presented in Sections 2.2 and 2.3. The sole exception is the solution of the linear system in (2.50) which is necessary in the computation of $\bar{\bar{\mathbf{Q}}}$; the auxiliary linear system

$$\bar{\bar{\mathbf{D}}}\left(\bar{\bar{\mathbf{R}}}^T\bar{\bar{\mathbf{G}}}\bar{\bar{\mathbf{P}}}\right)\bar{\mathbf{x}} = \bar{\bar{\mathbf{D}}}\bar{\mathbf{y}}, \tag{2.64}$$

should be solved instead, in order to ensure a well-conditioned right hand side matrix $\bar{\bar{\mathbf{D}}}\left(\bar{\bar{\mathbf{R}}}^T\bar{\bar{\mathbf{G}}}\bar{\bar{\mathbf{P}}}\right) = \bar{\bar{\mathbf{D}}}\bar{\bar{\mathbf{G}}}_m$.

2.5 Numerical Results

This section presents several examples that demonstrate the effectiveness of the proposed preconditioning scheme and its applicability to complex problems. The results presented here are obtained using a parallel and adaptive integral method

(AIM) accelerated EFIE MoM solver [19], which uses the proposed CMP or a standard diagonal preconditioner [37]. This solver uses a transpose-free quasi-minimal residual (TFQMR)-based iterative method [25] to solve the EFIE MoM systems. Where not otherwise specified, the CMP formulation in (2.22) has been used. All simulations were carried out on a cluster of dual-core 2.8-GHz AMD Opteron 2220 SE processors located at the University of Michigan Center for Advanced Computing.

2.5.1 Sphere

This section demonstrates the benefits of the proposed scheme when applied to closed structures. A sphere of radius $R = \lambda/20$ is excited by a z polarized plane wave incident from the $-x$ direction. The simulation is repeated for seven uniform discretizations with element size changing from $\delta = 0.00115\lambda$ to $\delta = 0.02\lambda$. The numbers of standard RWG functions for the densest and coarsest (non-barycentric) meshes are $N = 502000$ and $N = 89$, respectively. Fig. 2.8(a) presents the condition numbers of the diagonal preconditioned and CMP preconditioned EFIE MoM matrices versus δ. Note that since the computation of the condition number of large matrices is very costly, only those of matrices for the five coarsest meshes are presented. As is clearly seen in the figure, even for moderately dense discretizations the condition number of the diagonal preconditioned EFIE MoM matrix is orders of magnitude larger than that of the CMP preconditioned EFIE one. Fig. 2.8(b) shows the number of iterations required for the relative residual error of the MoM systems' solutions to reach 10^{-6}. In agreement with the condition numbers presented in Fig. 2.8(a), the number of iterations required to solve the diagonal preconditioned EFIE MoM system is reduced by approximately 15 times at $\delta = 0.02\lambda$ and approximately 120 times at $\delta = 0.00375\lambda$ (second densest mesh). Note that for the densest mesh, the iterative solver did not converge in 5000 iterations while solving

δ	Number RWGs on the standard mesh	Standard EFIE solution time (s)	CMP solution time (s)
0.02λ	1140	26.98	11.26
0.015λ	10062	495.22	59.89
0.00375λ	100596	21699.2	799.40
0.00115λ	520257	-	1868.48

Table 2.1: Sphere: CPU times required for the solution of the diagonal preconditioned and CMP preconditioned EFIE MoM systems.

the diagonal preconditioned EFIE MoM system; on the other hand the solution of CMP preconditioned EFIE MoM system still required only 10 iterations. Fig. 2.8(b) shows that the CMP compares favorably also with an incomplete LU preconditioning. Note that the iterative solution of the incomplete LU system matrices requires an increasing number of iterations for increasing mesh density. The high cost of the incomplete LU preconditioning allows only the comparison for the five coarsest meshes. To demonstrate the accuracy of proposed preconditioning scheme, the radar cross sections obtained by solving the diagonal preconditioned and CMP preconditioned EFIE MoM systems at $\delta = 0.00375\lambda$ are compared in Fig. 2.8(c). The relative norm of the difference between the two curves is less than 0.1%. Table 2.1 compares the CPU times required for the solution of the diagonal preconditioned and CMP preconditioned EFIE MoM systems for different discretization densities demonstrating the benefits of the proposed preconditioning scheme.

2.5.2 Plate

This section demonstrates the effectiveness of the proposed scheme when applied to open structures. A plate with side length $L = \lambda/10$ resides in the xy plane and its sides are aligned with the x-y coordinate axes. The plate is excited by an y-polarized plane wave incident from the z direction. The simulation is repeated for six uniform discretizations with element size changing from $\delta = 0.00018\lambda$ to $\delta = 0.0018\lambda$. The numbers of standard RWG functions for the densest and coarsest (non-barycentric)

δ	Number RWGs on the standard mesh	Standard EFIE solution time (s)	CMP solution time (s)
0.0012λ	13250	502.92	275.82
0.0009λ	20084	605.25	252.89
0.0007λ	34006	725.59	212.54
0.0005λ	61117	1707.42	341.56
0.0003λ	137492	4218.25	602.67
0.0002λ	550930	11431.22	1638.28

Table 2.2: Plate: CPU times required for the solution of the CMP preconditioned and diagonal preconditioned EFIE MoM systems.

meshes are $N = 550930$ and $N = 13250$, respectively. Fig. 2.9 shows the number of iterations required for the relative residual error of the MoM systems' solutions to reach 10^{-6}. The relative norm of the difference between the solutions of the diagonal preconditioned and CMP preconditioned EFIE MoM systems is less than 0.5%. Table 2.2 compares the CPU times required for the solution of the diagonal preconditioned and CMP preconditioned EFIE MoM systems for different discretization densities demonstrating the benefits of the proposed preconditioning scheme.

2.5.3 Space Shuttle

This section demonstrates the applicability of the proposed scheme to realistic structures through the analysis of scattering from a space shuttle model (Fig. 2.10(a)) excited by an x-polarized plane wave incident from z direction at frequency $f =$ 15 MHz. The shuttle length is 3λ at the frequency of excitation. A slot and waveguide are located on one side of the shuttle's fuselage, evidenced by an arrow in Fig. 2.10(a) and detailed in Figs. 2.10(c) and 2.10(d). The shuttle is discretized with an average element size around $\lambda/10$, except for the region near the slot and waveguide, where the average element size is around $\lambda/1200$. The number of standard RWG functions is $N = 29,409$. Since the discretization is nonuniform, the CMP (2.63) has been used. The iterative solver required $6,032$ and 89 iterations for the relative residual error of the diagonal and CMP preconditioned EFIE MoM systems'

solutions to reach 10^{-6} (Fig. 2.10(b)). The CPU times required for the solution of the diagonal preconditioned and CMP preconditioned EFIE MoM systems are 10h 18m and 53m respectively. Fig. 2.10(e) shows the absolute value of the current induced on the shuttle's surface in dB scale from three different views. The relative norm of the difference between the solutions of the diagonal preconditioned and CMP preconditioned EFIE MoM systems is 0.1024%.

2.5.4 Split-Ring/Wire Metamaterial

This section demonstrates the applicability of the proposed scheme to realistic structures through the analysis of scattering from a block of split-ring/wire metamaterial (Fig. 2.11(a)). The metamaterial is excited by an z-polarized plane wave incident from the x direction at frequency $f = 942$ MHz. The dimensions of the metamaterial blocks are $1.9\lambda \times 1.9\lambda \times 0.7\lambda$. The minimum element size of the discretization is around $\lambda/90$ at the frequency of excitation. The number of standard RWG functions for this discretization is $N = 614,088$. The iterative solver required $14,250$ and 447 iterations for the relative residual error of the diagonal preconditioned and CMP preconditioned EFIE MoM systems' solutions to reach 10^{-4} (Fig. 2.11(b)). The CPU times required for the solution of the diagonal preconditioned and CMP preconditioned EFIE MoM systems are 12h 40m and 2h 7m respectively. Figure 2.11(c) shows the absolute value of the current induced on the surfaces of rings and wires in dB scale from three different views. The relative norm of the difference between the solutions of the diagonal preconditioned and CMP preconditioned EFIE MoM systems is 0.3587%.

2.5.5 Radar Dish

This section demonstrates the applicability of the proposed scheme to open and realistic structures. A radar dish (Fig. 2.12(a)) is excited by an z-polarized plane wave incident from the y direction at frequency $f = 1.2$ GHz; the dish diameter is 4λ at the frequency of excitation. The maximum and minimum edge size of the discretization are around $\lambda/10$ and $\lambda/650$ respectively. The number of standard RWG functions is $N = 47009$. The need for fine discretization is justified by the need of properly model the curvature of the radar central feed. Since the radar dish is non uniformly discretized, the CMP (2.63) has been used. The iterative solver required 3251 and 60 iterations for the relative residual error of the diagonal preconditioned and CMP preconditioned EFIE MoM systems' solutions to reach 10^{-6} (Fig. 2.12(c)). The CPU times required for the solution of the diagonal preconditioned and CMP preconditioned EFIE MoM systems are 4h 55m and 38m respectively. Fig. 2.12(b) shows the absolute value of the current induced on the radar dish's surface in dB scale. The relative norm of the difference between the solutions of the diagonal preconditioned and CMP preconditioned EFIE MoM systems is 0.1639%.

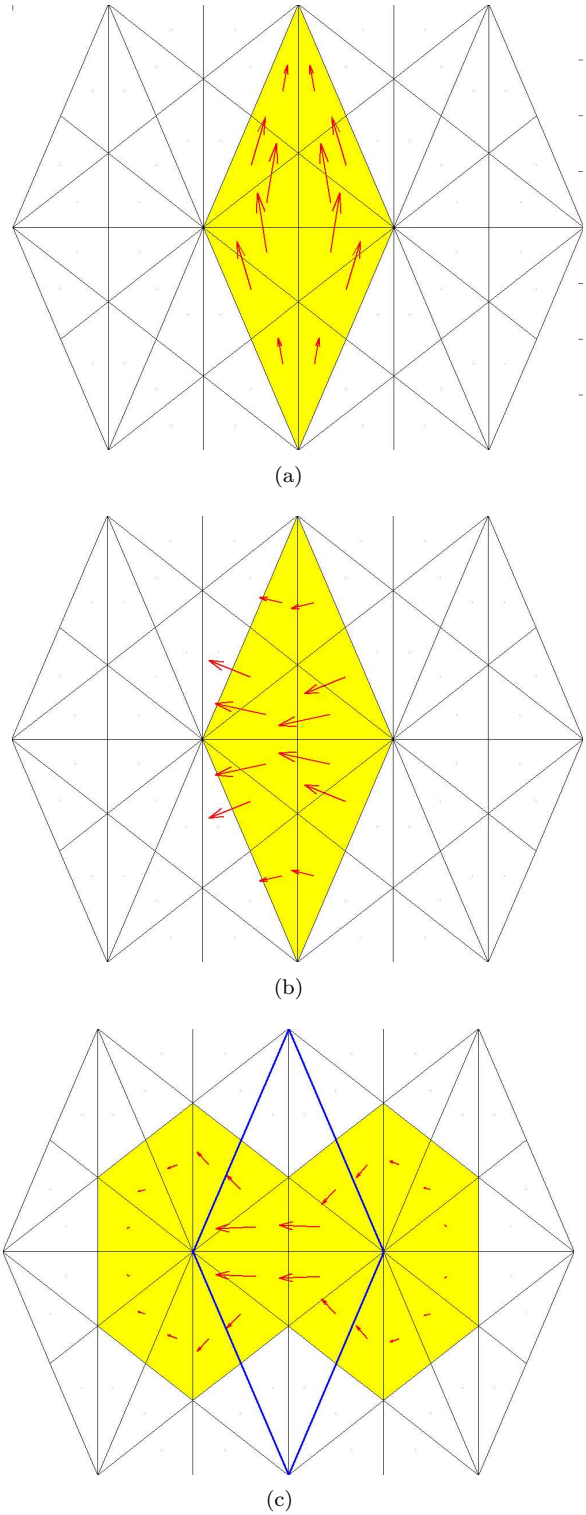

(a)

(b)

(c)

Figure 2.7: (a) RWG div-conforming basis function ($\boldsymbol{f}$), (b) RWG curl-conforming basis function ($\hat{\boldsymbol{n}}_{\boldsymbol{r}} \times \boldsymbol{f}$), (c) BC quasi-curl-conforming basis function (linear combination of div-conforming RWGs defined on the barycentric mesh)

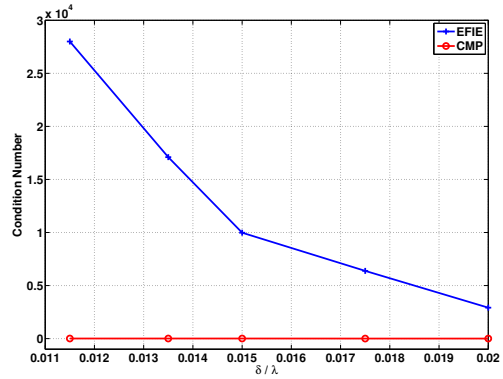

(a) Condition numbers

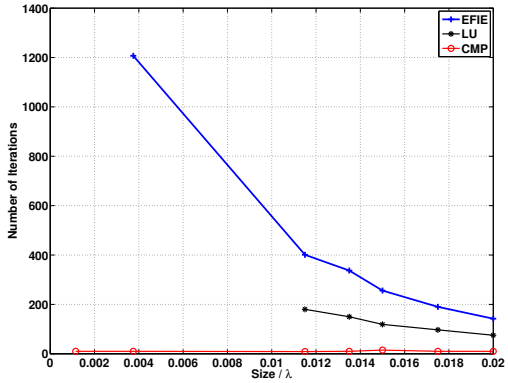

(b) Number of iterations

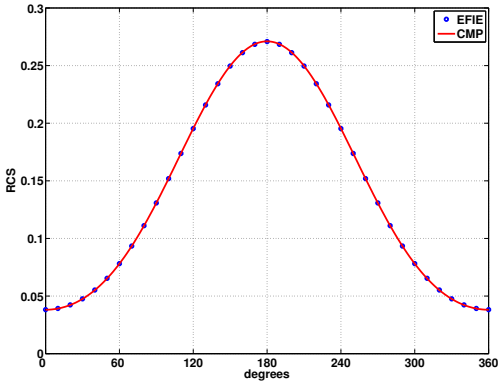

(c) Radar Cross Section (RCS)

Figure 2.8: Analysis of scattering from a sphere. (a) Condition numbers of the diagonal preconditioned and CMP preconditioned EFIE MoM matrices vs δ/λ. (b) Number of iterations required for the relative residual error of the diagonal preconditioned, incomplete LU-preconditioned and CMP preconditioned EFIE MoM systems solutions to reach 10^{-6} vs δ/λ. (c) Comparison of the RCS obtained by solving the diagonal preconditioned and CMP preconditioned EFIE MoM systems at $\delta = 0.00375\lambda$.

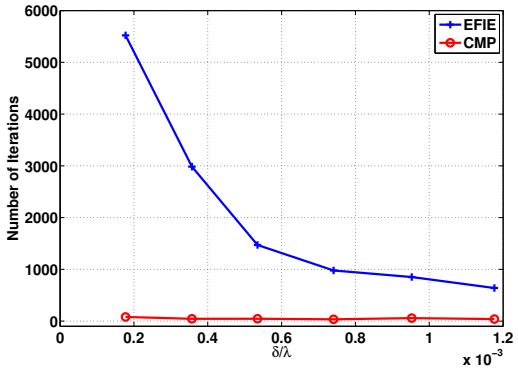

Figure 2.9: Analysis of scattering from a plate. Number of iterations required for the relative residual error of the EFIE MoM and preconditioned EFIE MoM systems solutions to reach 10^{-6} vs δ/λ.

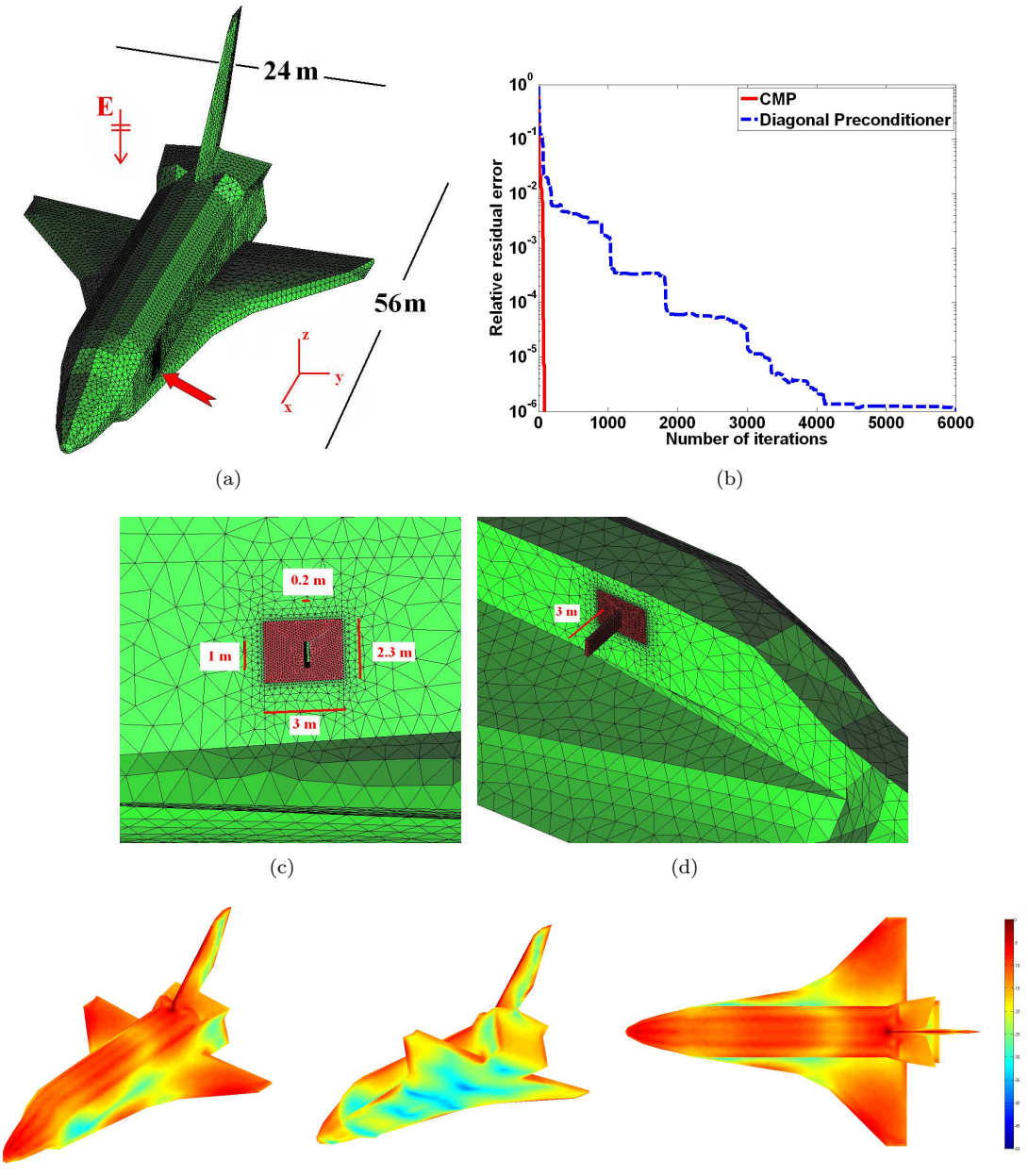

Figure 2.10: Analysis of scattering from a space shuttle with a slot waveguide.(a) Problem description. (b) Number of iterations. (c) Slot waveguide detail (outer view). (d) Slot waveguide detail (inner view). (e) Absolute value of the current density induced on the shuttle's surface from three different views (in dB scale).

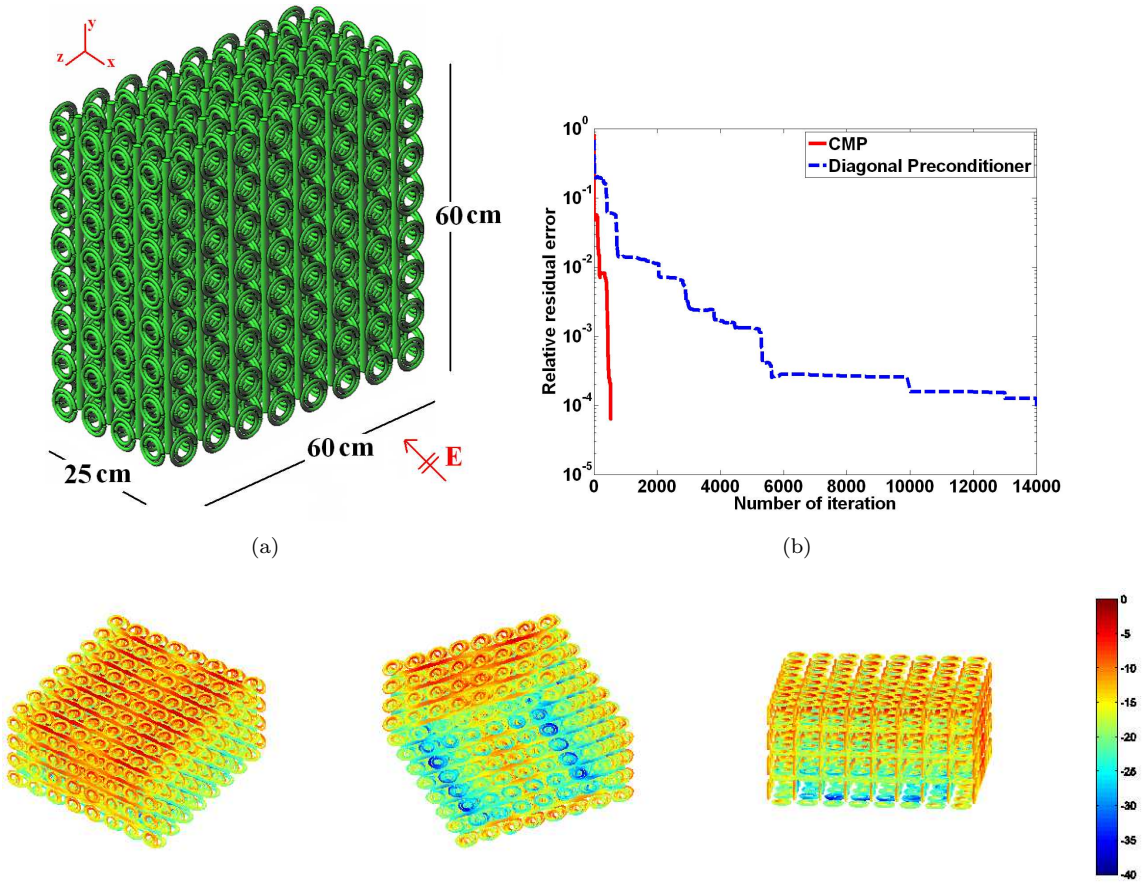

(a) (b)

(c)

Figure 2.11: Analysis of scattering from a split-ring wire metamaterial. (a) Problem description. (b) Number of iterations. (c) Absolute value of the current density induced on the surfaces of rings and wires from three different views (in dB scale).

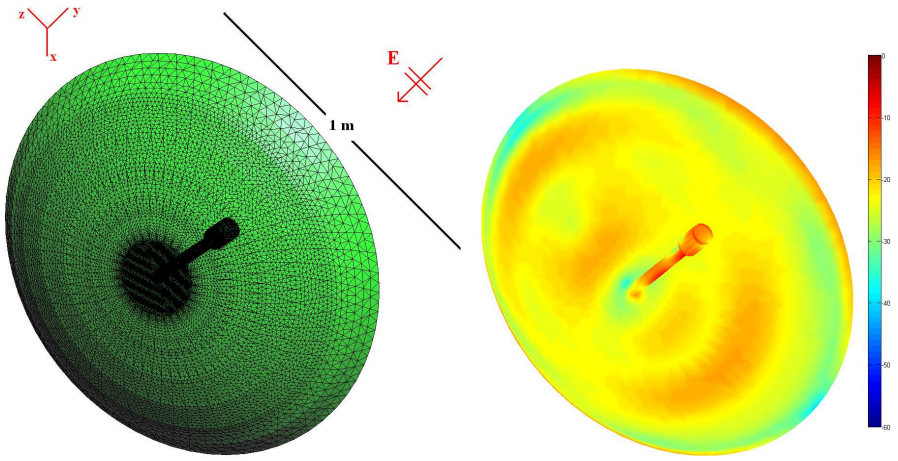

(a) Problem description

(b) Absolute value of the current density (in dB scale)

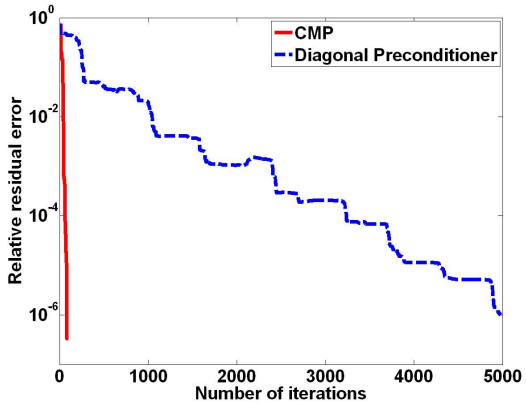

(c)

Figure 2.12: Analysis of scattering from radar dish. (a) Problem description. (b) Absolute value of the current density induced on the radar dish's surface from three different views (in dB scale). (c) Number of iterations.

CHAPTER III

A Regularized Combined Field Integral Equation for Scattering from 2D Perfect Electrically Conducting Objects

Among the many boundary integral equations for analyzing PEC scattering phenomena ever proposed, the electric and magnetic field integral equations (EFIE and MFIE) are used most extensively [28, 35]. These equations however pose two problems of note. First, EFIEs are often ill-posed and boundless due to the presence of compact and hypersingular terms [14]. Consequently, matrices obtained upon discretizing EFIEs are increasingly ill-conditioned for denser discretizations (see Chapter II). Second, EFIEs and MFIEs are singular when applied to closed surfaces at frequencies corresponding to eigenvalues of appropriately constructed interior Maxwell problems [14]. As a result, matrices obtained upon discretizing EFIEs and MFIEs are ill-conditioned for frequencies approaching these eigenvalues. While combined field integral equations (CFIEs), viz. judiciously constructed linear combinations of EFIEs and MFIEs [32], are provably nonsingular [14], they remain boundless when their EFIE component contains a hypersingular term. As a result, matrices obtained upon discretizing CFIEs (often) remain ill-conditioned for dense discretizations. In the past, a variety of methods aimed at constructing regularized EFIEs, i.e. modifications of original EFIEs that are well-posed and bounded, have been proposed. These methods often use readily constructed approximations of the inverse of the EFIE's

hypersingular part, e.g. by inverting a static EFIE [14, 49], by using quasi-Helmholtz decompositions (rearranged loop-star/tree) [57] or wavelet-based [3] source representations, or by leveraging the Calderón identities [29]. Construction of preconditioners via the Calderón identities, which expresses the fact that the EFIE operator is self-regularizing, i.e. that its square is a compact perturbation of the identity, may have implementation advantages over the previously cited approaches [2] and is the focus much current research [2, 15, 8]. A potential strategy for constructing a nonsingular and regular CFIE is to linearly combine a Calderón -regularized EFIE with the standard MFIE. Unfortunately, a classically Calderón -regularized EFIE cannot be combined directly with the MFIE as the "EFIE squared" acquires the resonances of the MFIE [29] and the resulting combined equation is not resonance-free. Hence, a procedure to localize the preconditioner is called for [2, 15, 8]. Localization approaches however involve a geometry-dependent trade-off between localization strength (to obtain a resonance-free equation) and proper description of nonlocal multiple scattering interactions (for structures that admit them) to ensure regularity of the equation; for this reason "the optimal localization of the EFIE operator can vary significantly" [2]. A novel Calderón -regularized CFIE not only nonsingular but also well-conditioned for dense discretizations is presented. Contrary to the above-cited efforts, the proposed preconditioner acts directly on the CFIE, not on the EFIE. This said, the philosophy behind the regularization process remains the same: the inverse of the hypersingular part has to be (at least) approximated. As is proven in Section 3.2, for the entire CFIE the part of the operator containing the hypersingularity can be inverted *exactly*. Numerical evidences show that acting with the regularizer on the entire CFIE does not introduce additional resonances. In other words there is not need for localization procedures and the formulation proposed can be applied on

different structures without a preliminary, case by case, optimization study.

In the following a time dependence $e^{-i\omega t}$ (with ω the angular frequency and i the imaginary unit) is assumed and suppressed. Cartesian unit vectors are denoted $\hat{\mathbf{x}}$, $\hat{\mathbf{y}}$, and $\hat{\mathbf{z}}$. Vectors confined to the $x-y$ plane are denoted $\boldsymbol{\rho} = x\hat{\mathbf{x}} + y\hat{\mathbf{y}}$.

3.1 Background

Consider an infinite 2D perfect electrically conducting (PEC) smooth cylinder that resides in a homogeneous medium with permittivity ε and permeability μ. The cylinder extends along the $\hat{\mathbf{z}}$axis and its cross section is described by a closed contour Γ in the $x-y$ plane defined by location vectors $\boldsymbol{\rho}(t)$ where t is a length coordinate; whenever possible, t-dependencies are omitted

Upon illumination of the cylinder by a TM_z electromagnetic wave with electric field $\boldsymbol{E}^i(\boldsymbol{\rho}) = E_z^i(\boldsymbol{\rho})\hat{\mathbf{z}}$, an electric current $\boldsymbol{J}_{TM}(\boldsymbol{\rho}) = J_z(\boldsymbol{\rho})\hat{\mathbf{z}}$ is induced on Γ; J_z satisfies the following electric and magnetic field integral equations:

$$\mathcal{T}_{tz}\left(J_z\right) \triangleq \hat{\mathbf{t}}_{\boldsymbol{\rho}} \frac{k}{4} \int_{\Gamma} H_0^1\left(k\left|\boldsymbol{\rho}-\boldsymbol{\rho}'\right|\right) J_z\left(\boldsymbol{\rho}'\right)\, \mathrm{d}\boldsymbol{\rho}' = \hat{\mathbf{t}}_{\boldsymbol{\rho}} \frac{E_z^i\left(\boldsymbol{\rho}\right)}{\eta}, \tag{3.1}$$

(TM-EFIE), and

$$\begin{aligned} \left(\frac{\mathcal{I}}{2} + \mathcal{K}_{zz}\right)\left(J_z\right) &\triangleq \hat{\mathbf{z}} \frac{J_z\left(\boldsymbol{\rho}\right)}{2} + \hat{\mathbf{z}}\, i \frac{k}{4} \hat{\mathbf{z}} \cdot \hat{\mathbf{n}}_{\boldsymbol{\rho}} \times \int_{\Gamma} H_1^1\left(k\left|\boldsymbol{\rho}-\boldsymbol{\rho}'\right|\right) \frac{\boldsymbol{\rho}-\boldsymbol{\rho}'}{\left|\boldsymbol{\rho}-\boldsymbol{\rho}'\right|} \times \hat{\mathbf{z}} J_z\left(\boldsymbol{\rho}'\right) d\boldsymbol{\rho}' \\ &= \hat{\mathbf{z}} H_t^i\left(\boldsymbol{\rho}\right) \end{aligned} \tag{3.2}$$

(TM-MFIE).

In the above equations, $\boldsymbol{\rho}(t), \boldsymbol{\rho}'(t') \in \Gamma$, $k = \omega\sqrt{\varepsilon\mu}$ is the wavenumber, $\eta = \sqrt{\mu/\varepsilon}$ is the surrounding medium's characteristic impedance, $\hat{\mathbf{n}}_{\boldsymbol{\rho}}$ and $\hat{\mathbf{t}}_{\boldsymbol{\rho}} = \hat{\mathbf{z}} \times \hat{\mathbf{n}}_{\boldsymbol{\rho}}$ are outward and counterclockwise pointing unit vectors normal and tangential to Γ (at $\boldsymbol{\rho}$), $H_0^1\left(.\right)$ and $H_1^1\left(.\right)$ are zeroth and first order Hankel functions of the first kind [1] ,

and $H_t^i(\boldsymbol{\rho}) = \hat{\mathbf{t}}_{\boldsymbol{\rho}} \cdot \frac{\nabla E_z^i \times \hat{\mathbf{z}}}{i\omega\mu}$ is the transverse incident magnetic field tangential to Γ (at $\boldsymbol{\rho}$).

Likewise, upon illumination by a TE_z electromagnetic wave with magnetic field $\boldsymbol{H}^i(\boldsymbol{\rho}) = H_z^i(\boldsymbol{\rho})\,\hat{\mathbf{z}}$, an electric current $\boldsymbol{J}_{TE}(\boldsymbol{\rho}) = J_t(\boldsymbol{\rho})\,\hat{\mathbf{t}}_{\boldsymbol{\rho}}$ is induced on Γ; J_t satisfies the following magnetic and electric field integral equations:

$$\begin{aligned}\left(\frac{\mathcal{I}}{2} + \mathcal{K}_{tt}\right)(J_t) &\triangleq \hat{\mathbf{t}}_{\boldsymbol{\rho}} \frac{J_t(\boldsymbol{\rho})}{2} \\ &+ \hat{\mathbf{t}}_{\boldsymbol{\rho}} i\frac{k}{4} \hat{\mathbf{t}}_{\boldsymbol{\rho}} \cdot \hat{\mathbf{n}}_{\boldsymbol{\rho}} \times \int_\Gamma H_1^1(k\,|\boldsymbol{\rho} - \boldsymbol{\rho}'|) \frac{\boldsymbol{\rho} - \boldsymbol{\rho}'}{|\boldsymbol{\rho} - \boldsymbol{\rho}'|} \times \hat{\mathbf{t}}_{\boldsymbol{\rho}'} J_t(\boldsymbol{\rho}')\, d\boldsymbol{\rho}' \quad (3.3) \\ &= \hat{\mathbf{t}}_{\boldsymbol{\rho}} \left(-H_z^i(\boldsymbol{\rho})\right)\end{aligned}$$

(TE-MFIE), and

$$\begin{aligned}\mathcal{T}_{zt}(J_t) &\triangleq \hat{\mathbf{z}} \left(-\frac{k}{4}\right) \hat{\mathbf{z}} \cdot \hat{\mathbf{n}}_{\boldsymbol{\rho}} \times \int_\Gamma H_0^1(k\,|\boldsymbol{\rho} - \boldsymbol{\rho}'|)\, \hat{\mathbf{t}}_{\boldsymbol{\rho}'} J_t(\boldsymbol{\rho}')\; d\boldsymbol{\rho}' + \\ &+ \hat{\mathbf{z}} \frac{1}{4} \hat{\mathbf{z}} \cdot \hat{\mathbf{n}}_{\boldsymbol{\rho}} \times p.v. \int_\Gamma H_1^1(k\,|\boldsymbol{\rho} - \boldsymbol{\rho}'|)\, \frac{\boldsymbol{\rho} - \boldsymbol{\rho}'}{|\boldsymbol{\rho} - \boldsymbol{\rho}'|}\, \frac{\partial J_t(\boldsymbol{\rho}'(t))}{\partial t}\; d\boldsymbol{\rho}' \quad (3.4) \\ &= \hat{\mathbf{z}} \left(-\frac{E_t^i(\boldsymbol{\rho})}{\eta}\right).\end{aligned}$$

(TE-EFIE).

Here, $E_t^i(\boldsymbol{\rho}) = \hat{\mathbf{t}}_{\boldsymbol{\rho}} \cdot \frac{\hat{\mathbf{z}} \times \nabla H_z^i}{i\omega\varepsilon}$ is the transverse incident electric field tangential to Γ (at $\boldsymbol{\rho}$) and $p.v.$ indicates the principal value of the integral.

Equations (3.1) through (3.4) can be cast in matrix form. Defining

$$\mathcal{K} \triangleq \begin{pmatrix} \mathcal{K}_{tt} & 0 \\ 0 & \mathcal{K}_{zz} \end{pmatrix} \quad (3.5)$$

and

$$\mathcal{T} \triangleq \begin{pmatrix} 0 & \mathcal{T}_{tz} \\ \mathcal{T}_{zt} & 0 \end{pmatrix}, \quad (3.6)$$

equations (3.1)-(3.2) and (3.4)-(3.2) can be expressed as

$$\left(\frac{\mathcal{I}}{2}+\mathcal{K}\right)\left(\begin{array}{c} J_t \\ J_z \end{array}\right)=\left(\begin{array}{c} -H_z^i\hat{\mathbf{t}}_{\boldsymbol{\rho}} \\ H_t^i\hat{\mathbf{z}} \end{array}\right)=\hat{\mathbf{n}}_{\boldsymbol{\rho}}\times\left(\begin{array}{c} H_z^i\hat{\mathbf{z}} \\ H_t^i\hat{\mathbf{t}}_{\boldsymbol{\rho}} \end{array}\right) \tag{3.7}$$

and

$$\mathcal{T}\left(\begin{array}{c} J_t \\ J_z \end{array}\right)=\left(\begin{array}{c} E_z^i\hat{\mathbf{t}}_{\boldsymbol{\rho}} \\ -E_t^i\hat{\mathbf{z}} \end{array}\right)\frac{1}{\eta}=-\hat{\mathbf{n}}_{\boldsymbol{\rho}}\times\left(\begin{array}{c} E_z^i\hat{\mathbf{z}} \\ E_t^i\hat{\mathbf{t}}_{\boldsymbol{\rho}} \end{array}\right)\frac{1}{\eta}, \tag{3.8}$$

respectively. The operators $\mathcal{K}$ and $\mathcal{T}$ in (3.9) and (3.10) satisfy the Calderón identities [29].

$$\mathcal{T}^2-\mathcal{K}^2=-\frac{\mathcal{I}}{4}, \tag{3.9}$$

$$\mathcal{T}\mathcal{K}+\mathcal{K}\mathcal{T}=0. \tag{3.10}$$

Approximate solutions to Equations (3.2) through (3.4) can be obtained using the method of moments [28]. The scalar unknowns $J_z(\boldsymbol{\rho})$ and $J_t(\boldsymbol{\rho})$ are expanded in terms of N basis functions $p_i(\boldsymbol{\rho}),\ \ i=1,\ \ldots,\ N$

$$J_z(\boldsymbol{\rho})=\sum_{i=1}^{N} I_i^z p_i(\boldsymbol{\rho}), \tag{3.11}$$

$$J_t(\boldsymbol{\rho})=\sum_{i=1}^{N} I_i^t p_i(\boldsymbol{\rho}). \tag{3.12}$$

After substituting (3.11) and (3.12) into (3.2)-(3.4) and testing each equation with the N basis functions p_i , the following four linear systems are obtained:

$$\boldsymbol{\mathcal{T}}_{tz}\boldsymbol{I}^z=\boldsymbol{V}_{\mathcal{T}}^z, \tag{3.13}$$

$$\left(\frac{\boldsymbol{\mathcal{I}}}{2}+\boldsymbol{\mathcal{K}}_{zz}\right)\boldsymbol{I}^z=\boldsymbol{V}_{\mathcal{K}}^z, \tag{3.14}$$

$$\left(\frac{\boldsymbol{\mathcal{I}}}{2}+\boldsymbol{\mathcal{K}}_{tt}\right)\boldsymbol{I}^t=\boldsymbol{V}_{\mathcal{K}}^t. \tag{3.15}$$

$$\boldsymbol{\mathcal{T}}_{zt}\boldsymbol{I}^t=\boldsymbol{V}_{\mathcal{T}}^t, \tag{3.16}$$

Here $\boldsymbol{\mathcal{T}}_{tz}$, $\boldsymbol{\mathcal{K}}_{zz}$, $\boldsymbol{\mathcal{K}}_{tt}$, $\boldsymbol{\mathcal{T}}_{zt}$, and $\boldsymbol{\mathcal{I}}$ are $N \times N$ matrices, and $\boldsymbol{I}^z$, $\boldsymbol{I}^t$, $\boldsymbol{V}^z_{\mathcal{T}}$, $\boldsymbol{V}^z_{\mathcal{K}}$, $\boldsymbol{V}^t_{\mathcal{K}}$, $\boldsymbol{V}^t_{\mathcal{T}}$, are N dimensional column vectors, defined as

$$(\boldsymbol{\mathcal{T}}_{tz})_{ij} = \int_{\Gamma} p_i(\boldsymbol{\rho})\ \hat{\mathbf{t}}_{\boldsymbol{\rho}} \cdot \mathcal{T}_{tz}(p_j)(\boldsymbol{\rho})\ d\boldsymbol{\rho}, \tag{3.17}$$

$$(\boldsymbol{\mathcal{K}}_{zz})_{ij} = \int_{\Gamma} p_i(\boldsymbol{\rho})\ \hat{\mathbf{z}} \cdot \mathcal{K}_{zz}(p_j)(\boldsymbol{\rho})\ d\boldsymbol{\rho}, \tag{3.18}$$

$$(\boldsymbol{\mathcal{K}}_{tt})_{ij} = \int_{\Gamma} p_i(\boldsymbol{\rho})\ \hat{\mathbf{t}}_{\boldsymbol{\rho}} \cdot \mathcal{K}_{tt}(p_j)(\boldsymbol{\rho})\ d\boldsymbol{\rho}, \tag{3.19}$$

$$(\boldsymbol{\mathcal{T}}_{zt})_{ij} = \int_{\Gamma} p_i(\boldsymbol{\rho})\ \hat{\mathbf{z}} \cdot \mathcal{T}_{zt}(p_j)(\boldsymbol{\rho})\ d\boldsymbol{\rho}, \tag{3.20}$$

$$(\boldsymbol{V}^z_{\mathcal{T}})_i = \frac{1}{\eta}\int_{\Gamma} p_i(\boldsymbol{\rho})\ E^i_z(\boldsymbol{\rho})\ d\boldsymbol{\rho}, \tag{3.21}$$

$$(\boldsymbol{V}^z_{\mathcal{K}})_i = \int_{\Gamma} p_i(\boldsymbol{\rho})\ H^i_t(\boldsymbol{\rho})\ d\boldsymbol{\rho}, \tag{3.22}$$

$$\left(\boldsymbol{V}^t_{\mathcal{K}}\right)_i = -\int_{\Gamma} p_i(\boldsymbol{\rho})\ H^i_z(\boldsymbol{\rho})\ d\boldsymbol{\rho}, \tag{3.23}$$

$$\left(\boldsymbol{V}^t_{\mathcal{T}}\right)_i = -\frac{1}{\eta}\int_{\Gamma} p_i(\boldsymbol{\rho})\ E^i_t(\boldsymbol{\rho})\ d\boldsymbol{\rho}, \tag{3.24}$$

$$(\boldsymbol{I}^z)_i = I^z_i, \tag{3.25}$$

$$\left(\boldsymbol{I}^t\right)_i = I^t_i. \tag{3.26}$$

For the sake of simplicity, the ensuing derivation assumes that the basis functions $p_i(\boldsymbol{\rho}), \quad i = 1, \ldots, N$ are orthonormal; as a result, the matrix $\boldsymbol{\mathcal{I}}$ in (3.14) and (3.15) is the identity. The general case of a non-orthonormal basis is managed by introducing the Gram matrix (see e.g. [2]). The discretization of (3.5) and (3.6) is immediately deduced by the discretization of (1)-(4). In fact it is sufficient to consider the block matrices

$$\boldsymbol{\mathcal{K}} \triangleq \begin{pmatrix} \boldsymbol{\mathcal{K}}_{tt} & 0 \\ 0 & \boldsymbol{\mathcal{K}}_{zz} \end{pmatrix} \tag{3.27}$$

and

$$\boldsymbol{\mathcal{T}} \triangleq \begin{pmatrix} 0 & \boldsymbol{\mathcal{T}}_{tz} \\ \boldsymbol{\mathcal{T}}_{zt} & 0 \end{pmatrix}. \tag{3.28}$$

The Calderòn identities (3.9) and (3.10), with $\mathcal{T}$ and $\mathcal{K}$ replaced by $\boldsymbol{\mathcal{T}}$ and $\boldsymbol{\mathcal{K}}$ hold approximately, with an error of the order of the discretization error from $\mathcal{T}$ and $\mathcal{K}$ to $\boldsymbol{\mathcal{T}}$ and $\boldsymbol{\mathcal{K}}$.

Equation (3.8) is ill-posed, i.e. neither $\mathcal{T}$ nor its inverse (when it exists) are continuous operators [36]. More specifically, referring to the definition in (3.6), $\mathcal{T}_{zt}$ is hypersingular while $\mathcal{T}_{tz}$ is compact. For this reason their discretized versions $\boldsymbol{\mathcal{T}}_{tz}$ in (3.13) and $\boldsymbol{\mathcal{T}}_{zt}$ in (3.16) have a high condition number for dense discretizations.

In addition, all of the equations (3.2)-(3.4) have a nontrivial null space when the wavenumber corresponds to an eigenvalue of the Laplacian operator for the internal region with Dirichlet (TM-EFIE, TE-MFIE) or Neuman (TE-EFIE, TM-MFIE) boundary conditions. This problem can be solved by using combined field integral equations; for the TE_z and TM_z polarizations these equations read (see e.g. [35]):

$$\text{TE-CFIE:} \quad \left[\hat{\mathbf{z}} \cdot \left(\frac{\mathcal{I}}{2} + \mathcal{K}_{zz}\right) + \alpha\, \hat{\mathbf{t}}_{\boldsymbol{\rho}} \cdot \mathcal{T}_{tz}\right](J_z) = H_t^i(\boldsymbol{\rho}) + \alpha \frac{E_z^i(\boldsymbol{\rho})}{\eta} \tag{3.29}$$

$$\text{TM-CFIE:} \quad \left[\hat{\mathbf{t}}_{\boldsymbol{\rho}} \cdot \left(\frac{\mathcal{I}}{2} + \mathcal{K}_{tt}\right) + \alpha\, \hat{\mathbf{z}} \cdot \mathcal{T}_{zt}\right](J_t) = -H_z^i(\boldsymbol{\rho}) - \alpha \frac{E_t^i(\boldsymbol{\rho})}{\eta} \tag{3.30}$$

with $\alpha > 0$.

Equations (3.29) and (3.30) have no null space. Equation (3.29) is well-posed since it is the sum of the second kind operator $\frac{\mathcal{I}}{2} + \mathcal{K}_{zz}$ and the compact operator $\mathcal{T}_{tz}$. Equation (3.30), in contrast, contains the hypersingular operator $\mathcal{T}_{zt}$ and for this reason its discretized version remains ill-conditioned for dense discretizations.

Equations (3.29) and (3.30) can be derived starting from the matrix form operators

$\mathcal{K}$ and $\mathcal{T}$. In fact defining the combined field integral operator as

$$\mathcal{C} = \left(\frac{\mathcal{I}}{2} + \mathcal{K} + \alpha \mathcal{T} \right), \tag{3.31}$$

it follows from definition (3.5) and (3.6) of the operators $\mathcal{K}$ and $\mathcal{T}$ that the scalar operators in (3.29) and (3.30) can be obtained testing the operator $\mathcal{C}$ in (3.31) with the vector $\hat{\mathbf{t}}_{\boldsymbol{\rho}} + \hat{\mathbf{z}}$:

$$\begin{aligned} &\left(\hat{\mathbf{t}}_{\boldsymbol{\rho}} + \hat{\mathbf{z}}\,, \hat{\mathbf{t}}_{\boldsymbol{\rho}} + \hat{\mathbf{z}}\right) \cdot \left(\frac{\mathcal{I}}{2} + \mathcal{K} + \alpha \mathcal{T} \right) = \\ &\left(\hat{\mathbf{t}}_{\boldsymbol{\rho}} \cdot \left(\frac{\mathcal{I}}{2} + \mathcal{K}_{tt} \right) + \alpha\, \hat{\mathbf{z}} \cdot \mathcal{T}_{zt}\,, \hat{\mathbf{z}} \cdot \left(\frac{\mathcal{I}}{2} + \mathcal{K}_{zz} \right) + \alpha\, \hat{\mathbf{t}}_{\boldsymbol{\rho}} \cdot \mathcal{T}_{tz} \right). \end{aligned} \tag{3.32}$$

This kind of testing is reminiscent of the TETHNENH approach for analyzing scattering from 3D dielectric bodies [46] . The operator $\mathcal{C}$, tested with $\hat{\mathbf{t}}_{\boldsymbol{\rho}} + \hat{\mathbf{z}}$ is resonant free, because so are the operators in (3.29) and (3.30).

It follows from Section I that the operators $\mathcal{T}$ and $\mathcal{C}$ are hypersingular. A method for regularizing the operator $\mathcal{C}$ is presented below. Note that this operator acts on both the TM_z and TE_z polarization. After regularization, testing by $\hat{\mathbf{t}}_{\boldsymbol{\rho}} + \hat{\mathbf{z}}$ will give rise to two scalar regularized equations, one for each polarizations, just as in (3.32).

3.2 Regularization of the combined field integral equation

This section presents a procedure for regularizing the hypersingular operator acting on J_t in (3.30). The regularized equation thus obtained will be immune from ill-conditioning due to dense discretizations.

Define the pseudo combined field integral equation (pCFIE) as

$$p\mathcal{C}\left(\mathbf{x}\right) \triangleq \left(\frac{\mathcal{I}}{2} + \alpha\, i\, \mathcal{K} + \alpha \mathcal{T} \right) \mathbf{x} = \mathbf{q}. \tag{3.33}$$

Here $\mathbf{x}$ represents the unknown and $\mathbf{q}$ an arbitrary RHS.

Left multiplying the pCFIE (3.33) by $(i\,\mathcal{K}+\mathcal{T})$ yields

$$\left(\frac{i\,\mathcal{K}+\mathcal{T}}{2}+\alpha\,(i\,\mathcal{K}+\mathcal{T})^2\right)\mathbf{x}=(i\,\mathcal{K}+\mathcal{T})\,\mathbf{q}. \tag{3.34}$$

Using (3.9) and (3.10) it follows that

$$(i\,\mathcal{K}+\mathcal{T})^2=\mathcal{T}^2+i\mathcal{T}\,\mathcal{K}+i\mathcal{K}\,\mathcal{T}-\mathcal{K}^2=-\frac{\mathcal{I}}{4}. \tag{3.35}$$

Multiplying (3.34) by 2α and subtracting the resulting equation from (3.33) yields

$$\frac{(1+\alpha^2)}{2}\mathbf{x}=\mathbf{q}-2\alpha\,(i\,\mathcal{K}+\mathcal{T})\,\mathbf{q} \tag{3.36}$$

or, equivalently

$$p\mathcal{C}^{-1}=\frac{2}{1+\alpha^2}\,(\mathcal{I}-2\alpha\,\,(i\,\mathcal{K}+\mathcal{T}))\,. \tag{3.37}$$

Recast the operator $\mathcal{C}$ in (3.31) as

$$\mathcal{C}=\left(\frac{\mathcal{I}}{2}+\mathcal{K}\,+\alpha\mathcal{T}\right)=\left(\frac{\mathcal{I}}{2}+\alpha\,i\,\mathcal{K}+\alpha\mathcal{T}+(1-\alpha\,i)\mathcal{K}\right)=p\mathcal{C}+(1-\alpha\,i)\mathcal{K}. \tag{3.38}$$

Here the definition of the pseudo-combined field operator $p\mathcal{C}$ in (3.33) has been used. Since $\mathcal{K}$ is compact, the pseudo-combined field operator $p\mathcal{C}$ fully describes the hypersingular behavior of the combined field operator $\mathcal{C}$. Note that the explicit expression (3.37) for the inverse $p\mathcal{C}^{-1}$ shows that the product $p\mathcal{C}^{-1}\mathcal{K}$ is regular, this from the regularity of $\mathcal{T}\,\mathcal{K}$ [36]. It thus follows that the operator

$$p\mathcal{C}^{-1}\mathcal{C}=\mathcal{I}+(1-\alpha\,i)p\mathcal{C}^{-1}\mathcal{K} \tag{3.39}$$

is well conditioned for dense discretizations or, in other words, that $p\mathcal{C}^{-1}$ is regularizer for $\mathcal{C}$ by inverting its hypersingularity.

Scalar regularized operators can be obtained by multiplying the regularized operator $p\mathcal{C}^{-1}\mathcal{C}$ in (3.39) by $\hat{\mathbf{t}}_{\boldsymbol{\rho}}+\hat{\mathbf{z}}$. Upon subdividing the matrix $p\mathcal{C}^{-1}$ in blocks along

the transverse ($\hat{\mathbf{t}}_{\boldsymbol{\rho}}$) and axial ($\hat{\mathbf{z}}$) components

$$p\mathcal{C}^{-1} = \begin{pmatrix} \left(p\mathcal{C}^{-1}\right)_{tt} & \left(p\mathcal{C}^{-1}\right)_{tz} \\ \left(p\mathcal{C}^{-1}\right)_{zt} & \left(p\mathcal{C}^{-1}\right)_{zz} \end{pmatrix}, \tag{3.40}$$

and testing $p\mathcal{C}^{-1}\mathcal{C}$ with $\hat{\mathbf{t}}_{\boldsymbol{\rho}} + \hat{\mathbf{z}}$, it is seen that the TE_z regularized combined field operator $r\mathcal{C}_{\mathcal{T}\mathrm{E}}$ is

$$r\mathcal{C}_{TE} \triangleq \left[\left(\left(p\mathcal{C}^{-1}\right)_{tt} + \left(p\mathcal{C}^{-1}\right)_{zt} \right) \left(\frac{\mathcal{I}}{2} + \mathcal{K}_{tt} \right) + \alpha \, \left(\left(p\mathcal{C}^{-1}\right)_{tz} + \left(p\mathcal{C}^{-1}\right)_{zz} \right) \mathcal{T}_{zt} \right] \tag{3.41}$$

while the regularized combined field integral equation for the TE_z polarization (TE-RCFIE) is

$$r\mathcal{C}_{TE}\left(J_t\right) = -\left(\left(p\mathcal{C}^{-1}\right)_{tt} + \left(p\mathcal{C}^{-1}\right)_{zt} \right) H_z^i\left(\boldsymbol{\rho}\right) - \alpha \, \left(\left(p\mathcal{C}^{-1}\right)_{tz} + \left(p\mathcal{C}^{-1}\right)_{zz} \right) \frac{E_t^i\left(\boldsymbol{\rho}\right)}{\eta}. \tag{3.42}$$

An similar equation can be obtained for the TM_z polarization; this equation is considered less interesting since the original combined field (3.29) does not contain any hypersingular terms and therefore is not presented here.

The discretized version of (3.42) can be implemented starting from the discretizaton of $\mathcal{T}$ and $\mathcal{K}$. In fact after obtaining the matrices $\boldsymbol{\mathcal{K}}_{tt}$, $\boldsymbol{\mathcal{T}}_{tz}$, $\boldsymbol{\mathcal{T}}_{zt}$, $\boldsymbol{\mathcal{K}}_{zz}$ using definitions (3.17)-(3.20), $\boldsymbol{\mathcal{K}}$ and $\boldsymbol{\mathcal{T}}$ can be obtained according to (3.27) and (3.28). By summing $\boldsymbol{\mathcal{K}}$ and $\boldsymbol{\mathcal{T}}$ according to (3.37) (replacing $\mathcal{T}$ and $\mathcal{K}$ with $\boldsymbol{\mathcal{K}}$ and $\boldsymbol{\mathcal{T}}$) the discretized version $p\boldsymbol{\mathcal{C}}^{-1}$ of $p\mathcal{C}^{-1}$ is obtained. Dividing this matrix in four equal square blocks

$$p\boldsymbol{\mathcal{C}}^{-1} = \begin{pmatrix} \left(p\boldsymbol{\mathcal{C}}^{-1}\right)_{tt} & \left(p\boldsymbol{\mathcal{C}}^{-1}\right)_{tz} \\ \left(p\boldsymbol{\mathcal{C}}^{-1}\right)_{zt} & \left(p\boldsymbol{\mathcal{C}}^{-1}\right)_{zz} \end{pmatrix} \tag{3.43}$$

yields the numerical counterparts of $\left(p\mathcal{C}^{-1}\right)_{tt}$, $\left(p\mathcal{C}^{-1}\right)_{tz}$, $\left(p\mathcal{C}^{-1}\right)_{zt}$, and $\left(p\mathcal{C}^{-1}\right)_{zz}$. The

regularized combined field matrix is obtained using (3.41)

$$r\boldsymbol{\mathcal{C}}_{TE} = \left[\left(\left(p\boldsymbol{\mathcal{C}}^{-1} \right)_{tt} + \left(p\boldsymbol{\mathcal{C}}^{-1} \right)_{zt} \right) \left(\frac{\mathcal{I}}{2} + \boldsymbol{\mathcal{K}}_{tt} \right) + \alpha \, \left(\left(p\boldsymbol{\mathcal{C}}^{-1} \right)_{tz} + \left(p\boldsymbol{\mathcal{C}}^{-1} \right)_{zz} \right) \boldsymbol{\mathcal{T}}_{zt} \right]. \tag{3.44}$$

The discretized TE-RCFIE reads

$$r\boldsymbol{\mathcal{C}}_{TE} \boldsymbol{I}^t = \boldsymbol{V}^t_{r\mathcal{C}} \tag{3.45}$$

where $\boldsymbol{I}^t$ is defined in (3.26) and $\boldsymbol{V}^t_{r\mathcal{C}}$ is defined using (3.24), and (3.42) as

$$\boldsymbol{V}^t_{r\mathcal{C}} \triangleq \left[\left(\left(p\boldsymbol{\mathcal{C}}^{-1} \right)_{tt} + \left(p\boldsymbol{\mathcal{C}}^{-1} \right)_{zt} \right) \boldsymbol{V}^t_{\mathcal{K}} + \alpha \, \left(\left(p\boldsymbol{\mathcal{C}}^{-1} \right)_{tz} + \left(p\boldsymbol{\mathcal{C}}^{-1} \right)_{zz} \right) \boldsymbol{V}^t_{\mathcal{T}} \right]. \tag{3.46}$$

Testing with $\hat{\mathbf{t}} + \hat{\mathbf{z}}$ does not alter the regular behavior of (3.39) which is consequently inherited by (3.41) and its discretized counterpart (3.44). In the next section this fact will be demonstrated numerically. Note that the explicit expression (3.37) for $p\mathcal{C}^{-1}$ makes the entire regularization procedure of practical use, since the numerical inversion of $p\mathcal{C}^{-1}$ is avoided and the computational overhead associated with applying the regularizer does not alter the computational complexity of the original problem. A semi-analytical study of the regularized combined field integral equation shows it to be resonant free for circular cylinders. Unfortunately, we have not been able to prove theoretically that the equation is resonant free for arbitrarily shaped scatterers, even though all our numerical experiments, including those reported below, support this hypothesis.

3.3 Numerical Results

This section demonstrates the behavior of the TE-RCFIE (3.45) for a variety of structures. The set p_i of basis functions used to discretize the equation are the normalized constant pulse basis functions defined on faceted surfaces [28]. The con-

ditioning of the matrices is measured using the condition number [26]

$$k(\mathbf{A}) = \left\|\mathbf{A}^{-1}\right\| \|\mathbf{A}\| \qquad \mathbf{A} \in \mathrm{R}^{N\times N} \tag{3.47}$$

where $\|\,.\,\|$ represent the spectral norm defined as the ratio between the maximum and the minimum singular value of $\mathbf{A}$.

Consider a circular cylinder; for this structure, the condition number of the matrix resulting from discretizing the TE-RCFIE (3.45) with $\alpha = 1$ was computed for different electrical radii $Radius/\lambda$ and compared to that of the matrices resulting from the MFIE, EFIE, and CFIE (3), (4), and (30); pulse basis functions of size $\lambda/10$ were used. The results depicted in Figure 3.1 indicate that, for this structure, both the TE-CFIE and the TE-RCFIE are resonance free. Below, it will be shown that, in contrast to the TE-CFIE, the TE-RCFIE also is well-posed.

The cylinder is exited by a plane wave with magnetic field $\mathbf{H}_{TE} = \hat{\mathbf{z}}\, e^{ikx}$. The reliability of the solution obtained with the TE-RCFIE is checked in Figure 3.2 where the relative error of the computed current is plotted against the electric radius.

Because the choice $\alpha = 1$ may seem arbitrary, the TE-CFIE and the TE-RCFIE were applied to a circular with electrical radius of 0.61 (where both the TE-EFIE and TE-MFIE resonate) for varying α. From Figure 3.3, which depicts the condition numbers of the TE-CFIE and TE-RCFIE matrices versus α, it is evident that the behavior of both equations only weakly depends on the combination parameter. A minimum in the condition number nevertheless is reached around $\alpha = 1$ – a value often quoted in the literature. This justifies the above choice for α; $\alpha = 1$ also will be used below.

The condition number of the TE-RCFIE for dense discretizations for the circular cylinder was compared to that of the TE-EFIE, TE-MFIE and TE-CFIE. Figure 3.4 shows the condition number of each matrix versus the inverse of the patch size. The

electrical radius is 0.39, which corresponds to a resonance of the TE-MFIE. Note that the TE-CFIE shares the hypersingular behavior of the TE-EFIE, which is the cause of the condition number growth for decreasing patch sizes. The relative error of the current is shown in Figure 3.5. The deviation of the TE-MFIE solution from the exact one is evident, while all the other equations and the TE-RCFIE in particular only exhibit a small relative error. For the discretization densities used here, the solution error of the RCFIE is as small as 1% (Figure 3.5).

The TE-RCFIE further has been tested on the structures in Figures 3.6 and 3.7 viz. a semi-ring and a wavy circular cylinder respectively. The semi-ring was obtained by translating a circle of radius $2R/3$ along a semi-circle of radius R. The wavy cylinder is defined by the polar coordinate relationship $\rho = \rho_0 \left(1 + \cos\left(5\vartheta\right)/4\right)$, where ρ_0 represents the average radius. As in the case of the cylinder, a scan for different electric radii has been performed for both these structures, in order to verify the stability of the TE-RCFIE. The patch size used in this test is $\lambda/10$. The results are in Figure 3.6 for the semi-ring and in Figure 3.7 for the wavy cylinder. As in the case of the circular cylinder, it is evident that the condition number of the TE-CFIE and the TE-RCFIE remains constant while those of the TE-EFIE and TE-MFIE peak when a resonance is crossed.

The behavior of the TE-RCFIE for small patch sizes similarly has been tested for both structures. The condition number of TE-EFIE, TE-MFIE, TE-CFIE and TE-RCFIE is plotted versus the inverse of the patch size. The results are presented in Figures 3.8 and 3.9 for the semi-ring and for the wavy cylinder, respectively. The TE-RCFIE is evidently well-conditioned independently of the patch size.

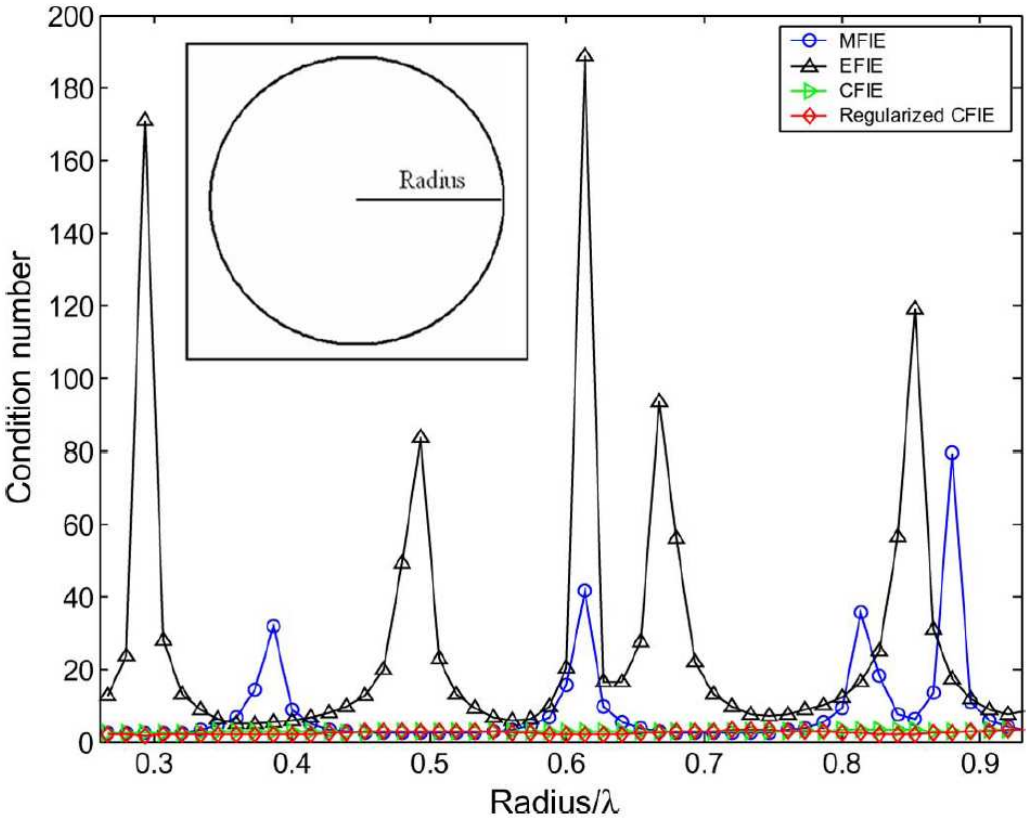

Figure 3.1: Circular Cylinder: condition number of different integral equations for different values of the electric radius $Radius/\lambda$.

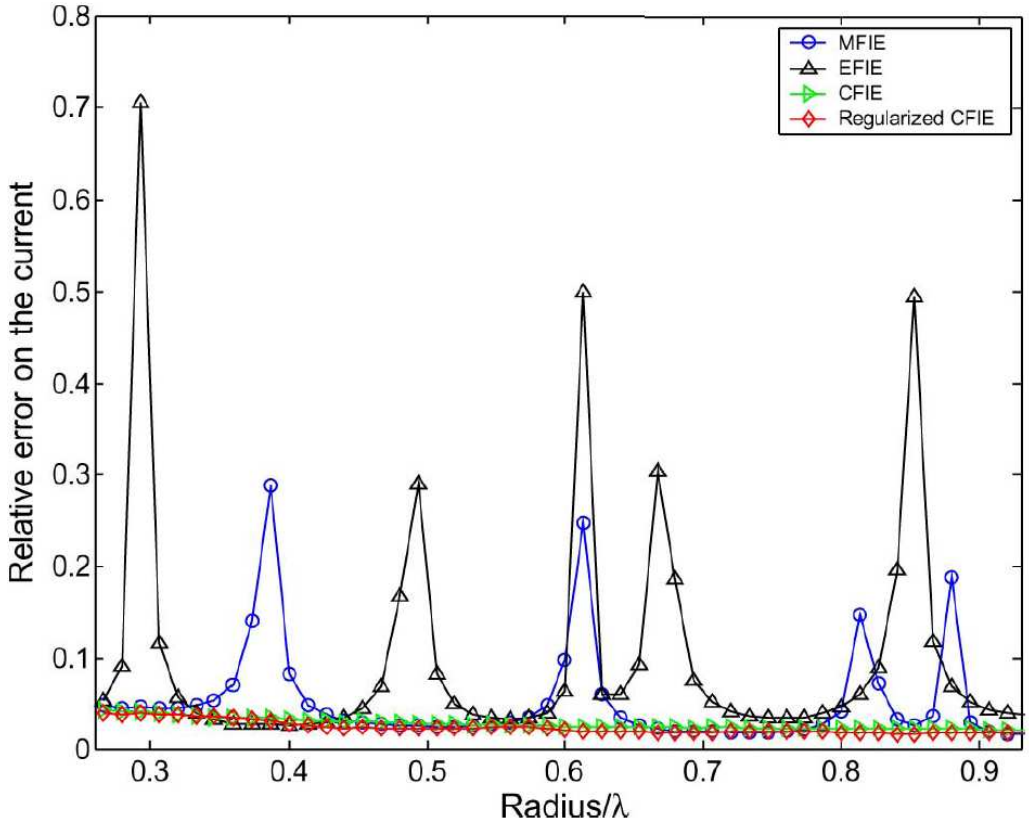

Figure 3.2: Circular Cylinder: relative error on the current for different values of the of the electric radius $Radius/\lambda$.

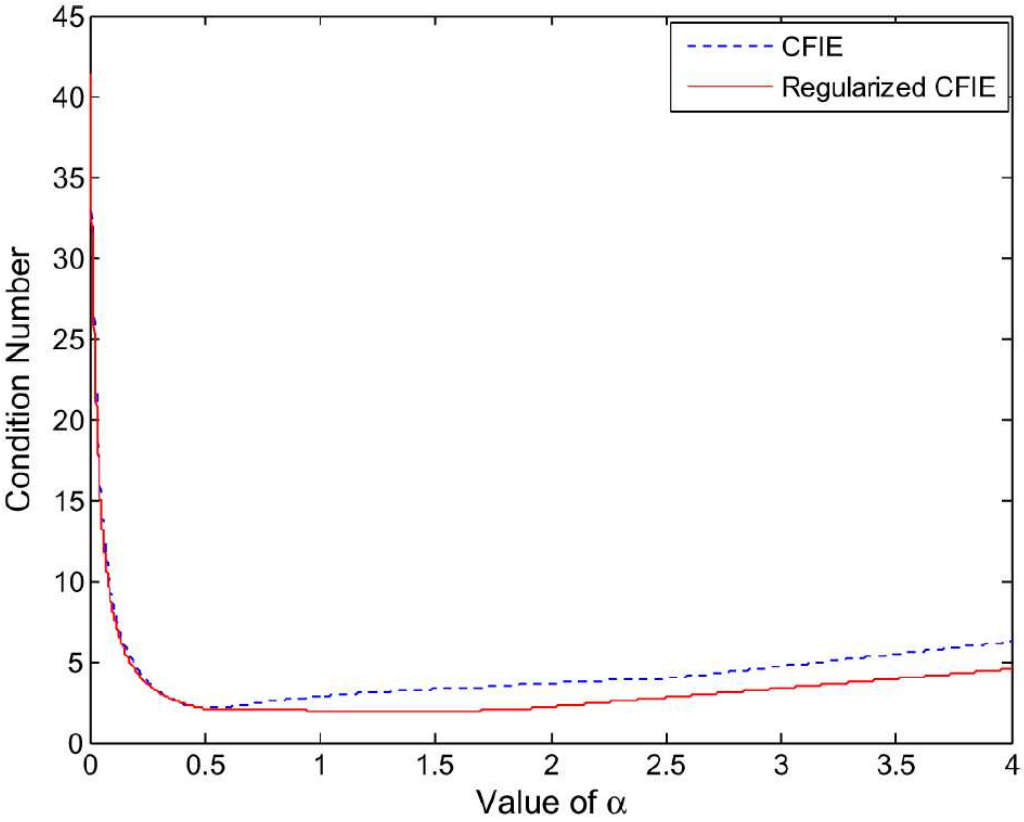

Figure 3.3: Circular Cylinder: condition number of CFIE and RCIFIE for different values of the parameter α.

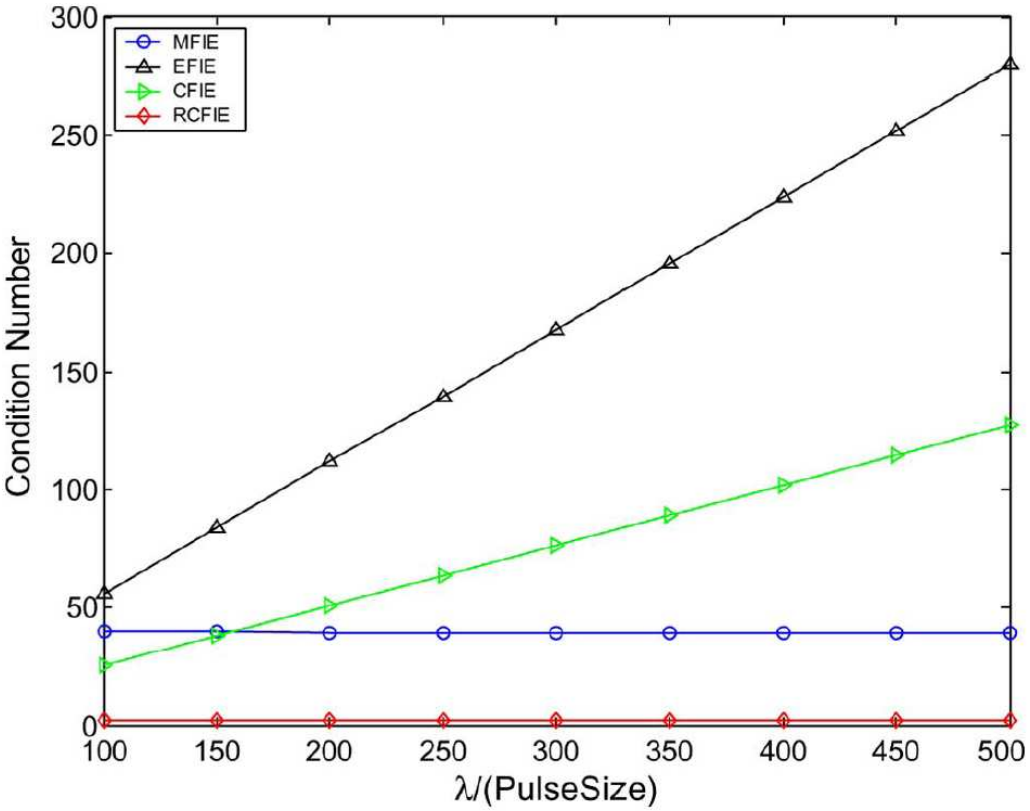

Figure 3.4: Circular Cylinder: condition number of different integral equations for different values of the pulse size.

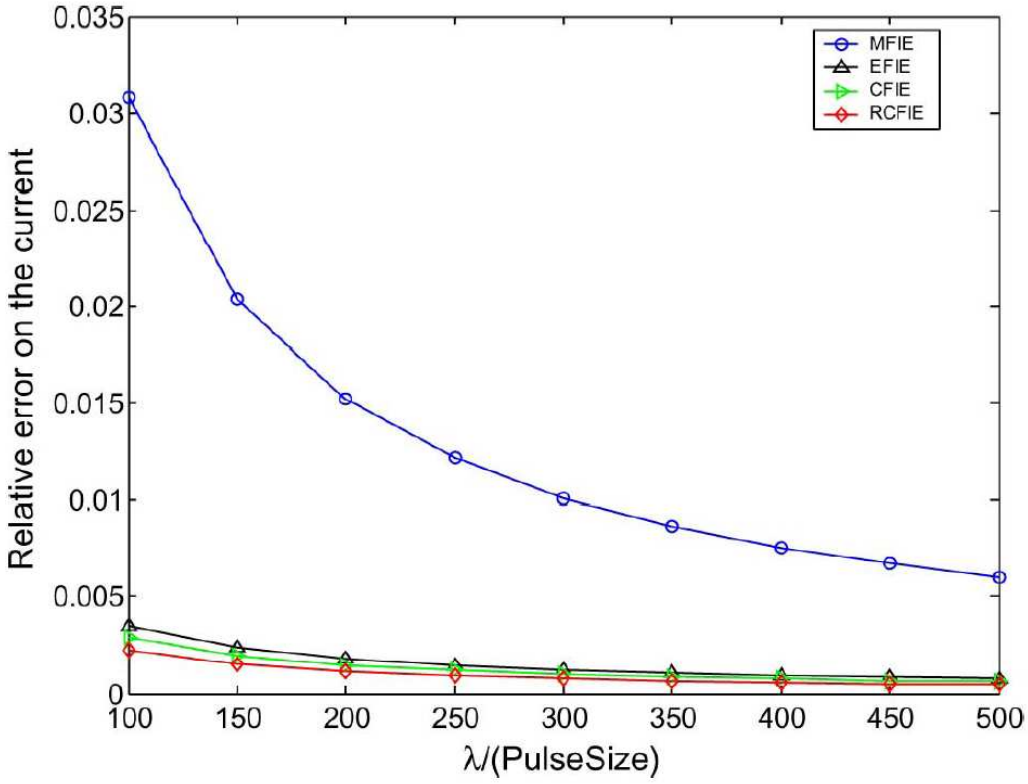

Figure 3.5: Circular Cylinder: relative error on the current for different integral equations for different values of the pulse size.

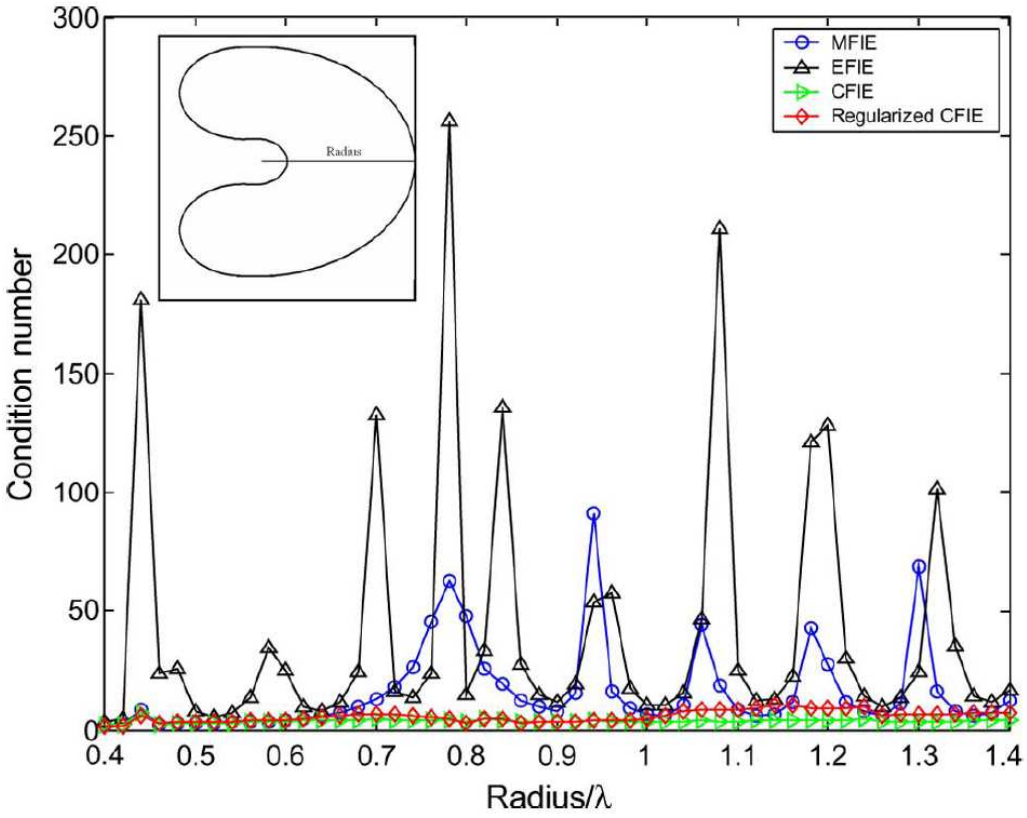

Figure 3.6: Semi-ring: condition number of different integral equations for different values of the outer electric radius $Radius/\lambda$

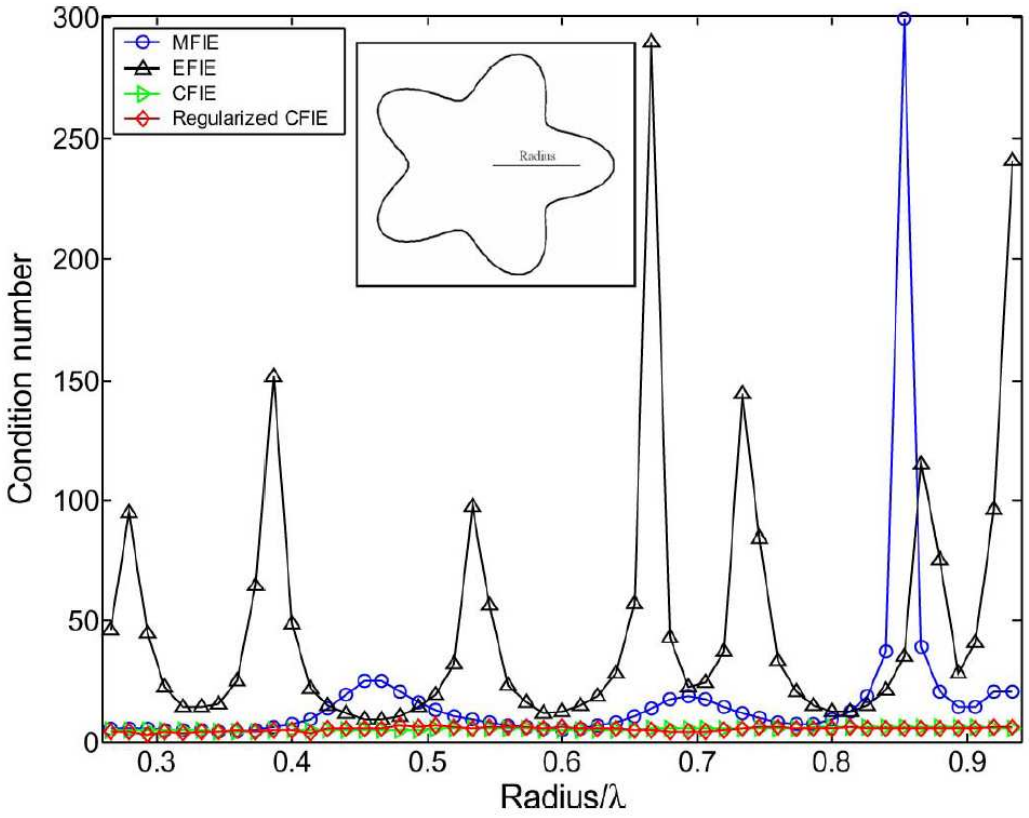

Figure 3.7: Waved cylinder: condition number of different integral equations for different values of the average electric radius $Radius/\lambda$.

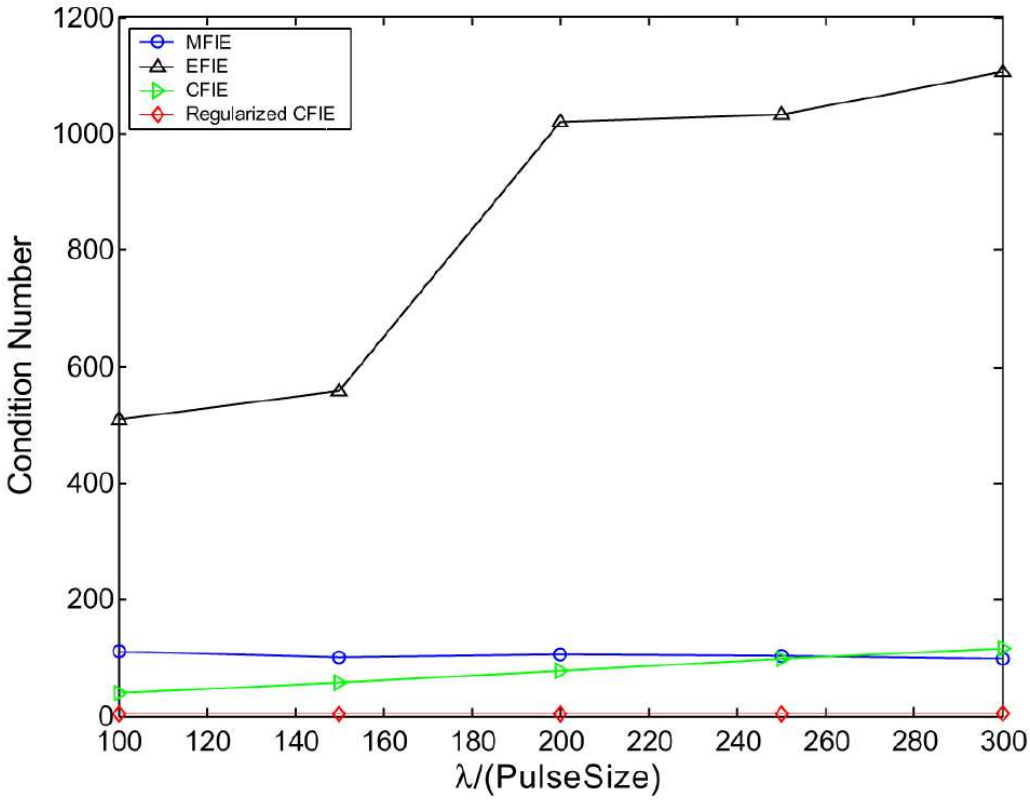

Figure 3.8: Semi-ring: condition number of different integral equations for different values of the pulse size.

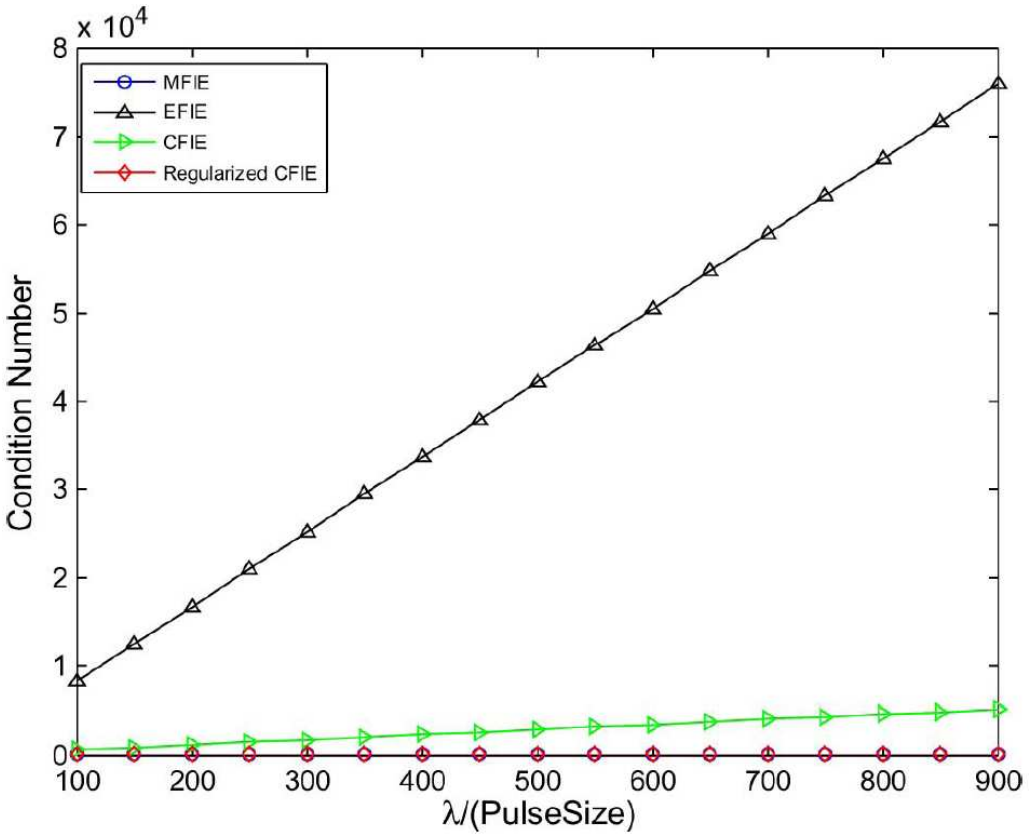

Figure 3.9: Waved cylinder: condition number of different integral equations for different values of the pulse size.

CHAPTER IV

Calderón Stabilized Time Domain Integral Equation Solvers

Marching on in time (MOT) based time domain integral equation solvers present an increasingly appealing technology for analyzing broadband electromagnetic radiation and scattering phenomena involving perfect electrically conducting (PEC) surfaces. Compared to their differential equation counterparts, these solvers automatically impose radiation conditions, do not require fields to be discretized throughout homogeneous volumes, and are highly immune to numerical dispersion. In addition, the computational efficiency of time domain integral equation solvers has soared following the development of plane wave time domain [24] and time domain adaptive integral methods [55] capable of rapidly evaluating transient fields due to wideband source constellations. Historically, MOT-EFIE solvers have been plagued by instabilities, some of which are rooted in the continuous time domain EFIE being solved while others stem from their (improper) discretization. The latter type of instabilities typically manifest itself as rapidly oscillating and exponentially growing solutions of MOT-EFIE systems. These instabilities have been studied extensively [18, 42, 53] and no longer present an issue in modern MOT-EFIE solvers. This study therefore concerns instabilities stemming from the spectral nature of the continuous time domain EFIE operator. These instabilities are either "DC" or "resonant" in nature.

DC instabilities are constant or linear-in-time solutions of MOT-EFIE systems that approximately reside in the null space of the (non-causal) time domain EFIE kernel; they arise because divergence free static currents produce zero electric fields. In the past, these instabilities have been partially cured by using loop-tree decompositions [10] and enforcing boundary conditions on normal magnetic field components [38]. Unfortunately, these methods do not completely annihilate the static null space of the time domain EFIE operator, and therefore do not guarantee that MOT-EFIE solutions are free of DC remnants. This chapter presents a modified time domain EFIE that resolves static and linear in time currents; upon discretization the resulting MOT-EFIE system therefore is immune to DC instabilities. The new equation is obtained by leveraging the time-domain Calderón formulas in conjunction with the "dot-trick", viz. a careful rearrangement of temporal derivative operators appearing in sequences of time domain EFIE operators. Resonant instabilities are harmonically oscillating solutions of MOT-EFIE systems that approximately reside in the null space of the (non-causal) time domain EFIE kernel; they arise because perfectly conducting cavities support discrete interior resonances. Resonant instabilities previously were subdued using time domain combined field integral equations (CFIEs) [44]. Unfortunately, the time domain MOT-CFIE systems, while giving rise to stable solutions, often were slowly convergent due to the presence of a hypersingular time domain EFIE kernel. This chapter presents a modified time domain CFIE that resolves interior resonances and is devoid of a hypersingular component; upon discretization the resulting MOT-CFIE system is free from resonant instabilities and rapidly convergent. The new equation is obtained by leveraging the time domain Calderón identities in conjunction with a simple space-time field localization procedure.

4.1 Preliminary Background

Consider a perfect electrically conducting closed body (PEC), occupying a domain Ω with boundary Γ residing in a homogeneous medium with frequency-independent permittivity ε, permeability μ and corresponding impedance $\eta = \sqrt{\mu/\varepsilon}$. The incident electric field $\boldsymbol{E}^i(\boldsymbol{r}, t)$ is zero for all $t < 0$ and is essentially band-limited with maximal frequency $f_{\max}$ and corresponding minimal wavelength $\lambda_{\min}$. It induces the current density $\boldsymbol{J}(\boldsymbol{r}, t)$ on the boundary of the PEC. This current distribution radiates the scattered field $\boldsymbol{E}^s(\boldsymbol{r}, t)$.

Define the operators $\mathcal{T}$ as

$$\mathcal{T} = \mathcal{T}_s + \mathcal{T}_h \tag{4.1}$$

with

$$\mathcal{T}_s\left[\boldsymbol{F}\right](\boldsymbol{r}, t) = -\frac{1}{4\pi c}\hat{\boldsymbol{n}} \times \int_\Gamma dS' \frac{\partial_t \boldsymbol{F}(\boldsymbol{r}', t - R/c)}{R} \tag{4.2}$$

$$\mathcal{T}_h\left[\boldsymbol{F}\right](\boldsymbol{r}, t) = \frac{c}{4\pi}\hat{\boldsymbol{n}} \times \int_\Gamma dS' \nabla \frac{\int_{-\infty}^{t-R/c} \nabla'_s \cdot \boldsymbol{F}(\boldsymbol{r}', t) dt'}{R}. \tag{4.3}$$

Here R equals $|\boldsymbol{r} - \boldsymbol{r}'|$, c is the speed of light, $\nabla_s \cdot$ the surface divergence operator, and $\hat{\boldsymbol{n}}$ is the outward pointing surface normal. The integral in the expressions for $\mathcal{T}_h$ should be interpreted in the Cauchy principal value sense.

The tangential component on the surface of the scatterer is $\hat{\boldsymbol{n}} \times \boldsymbol{E}^s(\boldsymbol{r}, t) = \eta\mathcal{T}[\boldsymbol{J}](\boldsymbol{r}, t)$. The total tangential electric field fulfills the following boundary condition:

$$\begin{aligned} \boldsymbol{0} &= \hat{\boldsymbol{n}} \times \boldsymbol{E}^i(\boldsymbol{r}, t) + \hat{\boldsymbol{n}} \times \boldsymbol{E}^s(\boldsymbol{r}, t) \\ &= \hat{\boldsymbol{n}} \times \boldsymbol{E}^i(\boldsymbol{r}, t) + \eta\mathcal{T}\left[\boldsymbol{J}\right](\boldsymbol{r}, t), \quad \forall \boldsymbol{r} \in \Gamma, \forall t > 0, \end{aligned} \tag{4.4}$$

Equation (4.4) is referred to as the time-domain electric field integral equation (time domain EFIE). To solve (4.4) the marching-on-in-time recipe is applied. The un-

known current density $\boldsymbol{J}(\boldsymbol{r},t)$ is approximated by N_T temporal and N_S spatial basis functions:

$$\boldsymbol{J}(\boldsymbol{r},t) \approx \sum_{i=1}^{N_T}\sum_{n=1}^{N_S} J_{i,n} T_i(t) \boldsymbol{f}_n(\boldsymbol{r}). \tag{4.5}$$

where $\boldsymbol{f}_n(\boldsymbol{r})$, $n = 1,\ldots,N_S$ are the spatial div-conforming basis functions and $T_i(t)$, $i = 1,\ldots,N_t$ are the temporal basis functions that satisfy

$$T_i(t) = T\left(t - i\Delta t\right) \tag{4.6}$$

with $T(t) = 0\ \forall t < \Delta t$. Here Δt denotes the time step size which is related to the maximum frequency f_{max} as

$$\Delta t = \frac{1}{\chi f_{max}}, \tag{4.7}$$

with $10 \leq \chi \leq 20$. In the following the functions $\boldsymbol{f}_n$ and T_i are the Rao-Wilton-Glisson (RWG) (Chapter II, eq. (2.6)) and the higher order polynomial interpolants [23] respectively; other choices, however, are possible (see for example [27, 53]) for which the techniques explained in this chapter remain valid.

To determine the expansion coefficients $J_{i,n}$ (4.5) is substituted into (4.4) and the resulting equation is tested in space with the curl-conforming functions $\hat{\boldsymbol{n}}_{\boldsymbol{r}} \times \boldsymbol{f}_n$ and evaluated at time $t_j = j\Delta t$ yielding

$$\sum_{k=0}^{j-1} \bar{\bar{\mathbf{T}}}_k \cdot \bar{\mathbf{J}}_{j-k} + \bar{\mathbf{E}}_j = \bar{\mathbf{0}}, \quad j = 1, ..., N_T \tag{4.8}$$

with

$$
\begin{aligned}
(\bar{\bar{\mathbf{T}}}_k)_{m,n} &= \langle \delta(t-j\Delta t)\hat{\boldsymbol{n}}\times \boldsymbol{f}_m(\boldsymbol{r})\,|\mathcal{I}|\,T_{j-k}(t)\boldsymbol{f}_n(\boldsymbol{r})\rangle \\
&= -\frac{1}{4\pi c}\iint_{\Gamma^2} dSdS'\boldsymbol{f}_m(\boldsymbol{r})\cdot\boldsymbol{f}_n(\boldsymbol{r})\frac{\partial_t T(k\Delta t - R/c)}{R}, \\
&\quad -\frac{c}{4\pi}\iint_{\Gamma^2} dSdS'\nabla_s\cdot\boldsymbol{f}_m(\boldsymbol{r})\nabla'_s\cdot\boldsymbol{f}_n(\boldsymbol{r})\frac{\int_{-\infty}^{k\Delta t-R/c}T(t')\,\mathrm{d}t'}{R} \qquad (4.9)\\
(\bar{\mathbf{E}}_j)_m &= \left\langle \delta(t-j\Delta t)\hat{\boldsymbol{n}}\times\boldsymbol{f}_m(\boldsymbol{r})|\frac{1}{\eta}\hat{\boldsymbol{n}}\times\boldsymbol{E}^i(\boldsymbol{r},t)\right\rangle \\
&= \frac{1}{\eta}\int_\Gamma dS\boldsymbol{f}_m(\boldsymbol{r})\cdot\boldsymbol{E}^i(\boldsymbol{r},j\Delta t)/\eta \qquad (4.10)
\end{aligned}
$$

and $(\bar{\mathbf{J}}_j)_n = J_{j,n}$. Since $T(t) = 0, \forall t < -\Delta t$, all matrices $\bar{\bar{\mathbf{T}}}_k$ are identically zero when $k < 0$. The number $k_{\max}$ of non-zero interaction matrices $\bar{\bar{\mathbf{T}}}_k$ is of the order $D/c\Delta t$, where D is the diameter of the scatterer. The current expansion coefficients at time $t = \Delta t$ can directly be solved from the equation corresponding to $j = 1$. Using the knowledge of the current expansion coefficients at $t = \Delta t$, the coefficients at $t = 2\Delta t$ can be found from the equation with $j = 2$. By repeating this process, all expansion coefficients can be found. This is called marching-on-in-time (MOT). Every time step, a linear system of dimension N_S with coefficient matrix $\bar{\bar{\mathbf{T}}}_0$ has to be solved. Note that successively solving (4.8) for $j = 1, ..., N_T$ amounts to solving the following lower triangle block matrix system using back-substitution.

$$
\begin{pmatrix}
\bar{\bar{\mathbf{T}}}_0 & & & \\
\bar{\bar{\mathbf{T}}}_1 & \bar{\bar{\mathbf{T}}}_0 & & \\
\bar{\bar{\mathbf{T}}}_2 & \bar{\bar{\mathbf{T}}}_1 & \bar{\bar{\mathbf{T}}}_0 & \\
\vdots & \vdots & \vdots & \ddots
\end{pmatrix}\cdot
\begin{pmatrix}
\bar{\mathbf{J}}_1 \\ \bar{\mathbf{J}}_2 \\ \bar{\mathbf{J}}_3 \\ \vdots
\end{pmatrix} +
\begin{pmatrix}
\bar{\mathbf{E}}_1 \\ \bar{\mathbf{E}}_2 \\ \bar{\mathbf{E}}_3 \\ \vdots
\end{pmatrix} = 0, \qquad (4.11)
$$

or in short

$$
\bar{\bar{\mathbf{T}}}\bar{\mathbf{J}} + \bar{\mathbf{E}} = 0. \qquad (4.12)
$$

The evaluation of the matrix elements in (4.9) requires the computation of an integral in time (present in $\mathcal{T}_h$); this is computationally inefficient [45]. For this reason,

instead of the time domain EFIE in (4.4), the differentiated time domain EFIE is often preferred

$$\dot{\mathcal{T}}\left[\boldsymbol{J}\right](\boldsymbol{r},t) = -\frac{1}{\eta}\hat{\boldsymbol{n}}_{\boldsymbol{r}} \times \frac{\partial \boldsymbol{E}^i}{\partial t} \tag{4.13}$$

with

$$\dot{\mathcal{T}}\left[\boldsymbol{J}\right](\boldsymbol{r},t) = \dot{\mathcal{T}}_s\left[\boldsymbol{J}\right](\boldsymbol{r},t) + \dot{\mathcal{T}}_h\left[\boldsymbol{J}\right](\boldsymbol{r},t), \tag{4.14}$$

$$\dot{\mathcal{T}}_h\left[\boldsymbol{J}\right](\boldsymbol{r},t) = \frac{c}{4\pi}\hat{\boldsymbol{n}} \times \int_\Gamma dS' \nabla \frac{\nabla'_s \cdot \boldsymbol{J}(\boldsymbol{r}', t - R/c)}{R}, \tag{4.15}$$

$$\dot{\mathcal{T}}_s\left[\boldsymbol{J}\right](\boldsymbol{r},t) = -\frac{1}{4\pi c}\hat{\boldsymbol{n}} \times \int_\Gamma \mathrm{d}S' \frac{\partial_t^2 \boldsymbol{J}(\boldsymbol{r}', t - R/c)}{R}. \tag{4.16}$$

The differentiated time domain EFIE (4.13) can be solved with the same method outlined above for (4.4). In particular all the equations remain valid provided that $\mathcal{T}$ is replaced by $\dot{\mathcal{T}}$ and the symbols $\bar{\bar{\mathbf{T}}}$, $\bar{\mathbf{E}}$ with $\dot{\bar{\bar{\mathbf{T}}}}$, $\dot{\bar{\mathbf{E}}}$. In particular the discretized counterpart of (4.13) will read

$$\dot{\bar{\bar{\mathbf{T}}}}\bar{\mathbf{J}} + \dot{\bar{\mathbf{E}}} = 0. \tag{4.17}$$

The MOT-TDEFIE system (4.4) and its differentiated version (4.13) often are plagued by instabilities, i.e. non decaying solutions $\bar{\mathbf{J}}$ ($\lim_{j\to\infty} \bar{\mathbf{J}}_j \neq 0$) in the presence of decaying forcing terms $\bar{\mathbf{E}}$ ($\lim_{j\to\infty} \bar{\mathbf{E}}_j = 0$).

Instabilities due to incorrect discretization of the TDEFIE operator aside, MOT-TDEFIE instabilities are rooted in the the spectral properties of $\mathcal{T}$ and cannot be avoided (without modifying the operator itself). These instabilities can be classified based on the behavior of the solution $\bar{\mathbf{J}}$ to the undriven equation $\bar{\bar{\mathbf{T}}}\bar{\mathbf{J}} = \bar{\mathbf{0}}$ using the "companion matrix" technique [51]. To study the behavior of solutions to the undriven equation $\bar{\bar{\mathbf{T}}}\bar{\mathbf{J}} = \bar{\mathbf{0}}$, define

$$\bar{\bar{\mathbf{J}}}_j = \begin{pmatrix} \bar{\mathbf{J}}_j & \bar{\mathbf{J}}_{j-1} & \bar{\mathbf{J}}_{j-2} & \dots \end{pmatrix}^T. \tag{4.18}$$

The equality

$$\begin{pmatrix} \bar{\bar{\mathbf{T}}}_0 & & & & \\ & \bar{\bar{\mathbf{I}}} & & & \\ & & \bar{\bar{\mathbf{I}}} & & \\ & & & \ddots & \\ & & & & \bar{\bar{\mathbf{I}}} \end{pmatrix} \bar{\bar{\mathbf{J}}}_j = \begin{pmatrix} -\bar{\bar{\mathbf{T}}}_1 & -\bar{\bar{\mathbf{T}}}_2 & -\bar{\bar{\mathbf{T}}}_3 & \dots & -\bar{\bar{\mathbf{T}}}_{k_{max}} \\ \bar{\bar{\mathbf{I}}} & & & & \\ & \bar{\bar{\mathbf{I}}} & & & \\ & & \bar{\bar{\mathbf{I}}} & \ddots & \\ & & & \bar{\bar{\mathbf{I}}} & \end{pmatrix} \bar{\bar{\mathbf{J}}}_{j-1} \tag{4.19}$$

follows from (4.8). Solving (4.19) for $\bar{\bar{\mathbf{J}}}_j$ yields the difference equation

$$\bar{\bar{\mathbf{J}}}_j = \bar{\bar{\mathbf{T}}}_C \bar{\bar{\mathbf{J}}}_{j-1} \tag{4.20}$$

where the companion matrix $\bar{\bar{\mathbf{T}}}_C$ is

$$\bar{\bar{\mathbf{T}}}_C = \begin{pmatrix} -\left(\bar{\bar{\mathbf{T}}}_0\right)^{-1}\bar{\bar{\mathbf{T}}}_1 & -\left(\bar{\bar{\mathbf{T}}}_0\right)^{-1}\bar{\bar{\mathbf{T}}}_2 & -\left(\bar{\bar{\mathbf{T}}}_0\right)^{-1}\bar{\bar{\mathbf{T}}}_3 & \dots & -\left(\bar{\bar{\mathbf{T}}}_0\right)^{-1}\bar{\bar{\mathbf{T}}}_{k_{max}} \\ \bar{\bar{\mathbf{I}}} & & & & \\ & \bar{\bar{\mathbf{I}}} & & & \\ & & \bar{\bar{\mathbf{I}}} & \ddots & \\ & & & \bar{\bar{\mathbf{I}}} & \end{pmatrix}. \tag{4.21}$$

The general solution of (4.20) is [34]

$$\bar{\bar{\mathbf{J}}}_{j-1} = \sum_n \left(\lambda_n^c\right)^j \bar{\mathbf{v}}_n^c + \sum_n \left(\lambda_n^i\right)^j \left(\bar{\mathbf{v}}_{n1}^i + \bar{\mathbf{v}}_{n2}^i j + \dots\right) \tag{4.22}$$

where $\{\lambda_n^c\}$ are the eigenvalues of $\bar{\bar{\mathbf{T}}}_C$ relative to complete eigenspaces, $\{\bar{\mathbf{v}}_n^c\}$ are the corresponding eigenvectors, $\{\lambda_n^i\}$ are eigenvalues of $\bar{\bar{\mathbf{T}}}_C$ relative to incomplete eigenspaces (if any), and $\{\bar{\mathbf{v}}_{nk}^i\}$ the corresponding generalized eigenvectors [26]. The eigenvalues of $\bar{\bar{\mathbf{T}}}_C$ are known as $\bar{\bar{\mathbf{T}}}$'s *polynomial eigenvalues*. An identical analysis can be performed for $\dot{\bar{\bar{\mathbf{T}}}}$. The matrices $\bar{\bar{\mathbf{T}}}$ (or $\dot{\bar{\bar{\mathbf{T}}}}$) can be classified as follows:

- Class 1: the polynomial spectrum of $\bar{\bar{\mathbf{T}}}$ (or $\dot{\bar{\bar{\mathbf{T}}}}$) contains at least one λ so that $|\lambda| > 1$. The solution $\bar{\bar{\mathbf{J}}}$ is unstable and grows exponentially as $j \to \infty$.

- Class 2: the polynomial spectrum of $\bar{\bar{\mathbf{T}}}$ (or $\dot{\bar{\bar{\mathbf{T}}}}$) contains at least one λ so that $|\lambda| = 1$ and no eigenvalues reside outside the unit circle of the complex plane. The solution $\bar{\bar{\mathbf{J}}}$ is unstable and grows at most polynomially as $j \to \infty$.

- Class 3: the polynomial spectrum of $\bar{\bar{\mathbf{T}}}$ (or $\dot{\bar{\bar{\mathbf{T}}}}$) is strictly contained in the unit circle of the complex plane, i.e. $|\lambda| < 1 \quad \forall\lambda$. The solution $\bar{\bar{\mathbf{J}}}$ is stable and decays as $j \to \infty$.

The matrix $\bar{\bar{\mathbf{T}}}$ (or $\dot{\bar{\bar{\mathbf{T}}}}$) produced by modern MOT-TDEFIE solvers belongs at the best to Class 2. Moreover $\bar{\bar{\mathbf{T}}}$ (or $\dot{\bar{\bar{\mathbf{T}}}}$) can become of Class 1 when eigenvalues that theoretically should reside *on* the unit circle shift slightly outward. Below, new MOT time domain integral equation solvers that produce matrices of Class 3, completely immune to Class 1 and 2 instabilities while producing accurate solutions even when applied to dense meshes, are developed.

The null space of the TDEFIE operator $\mathcal{T}$ comprises static solenoidal currents, i.e. currents $\boldsymbol{J}(\boldsymbol{r}, t)$ satisfying

$$\frac{\partial \boldsymbol{J}}{\partial t} = \nabla_s \cdot \boldsymbol{J} = 0. \tag{4.23}$$

As $\bar{\bar{\mathbf{T}}}'s$ ordinary spectrum is mapped onto its polynomial spectrum via a Z-transform-like mapping the spectrum of $\bar{\bar{\mathbf{T}}}_C$ would have contained a number of eigenvalues in $1+0i$ equal to the number N_{sol} of linearly independent solenoidal currents spanned by the spatial basis functions $\boldsymbol{f}_n^{RWG}$; this argument tacitly assumes that the discretization process itself is error-free. A similar argument applies to the differentiated TDEFIE operator $\dot{\mathcal{T}}$ for which the null space is populated by the linear-in-time solenoidal currents, i.e. currents satisfying

$$\frac{\partial^2 \boldsymbol{J}}{\partial t^2} = \nabla_s \cdot \boldsymbol{J} = 0. \tag{4.24}$$

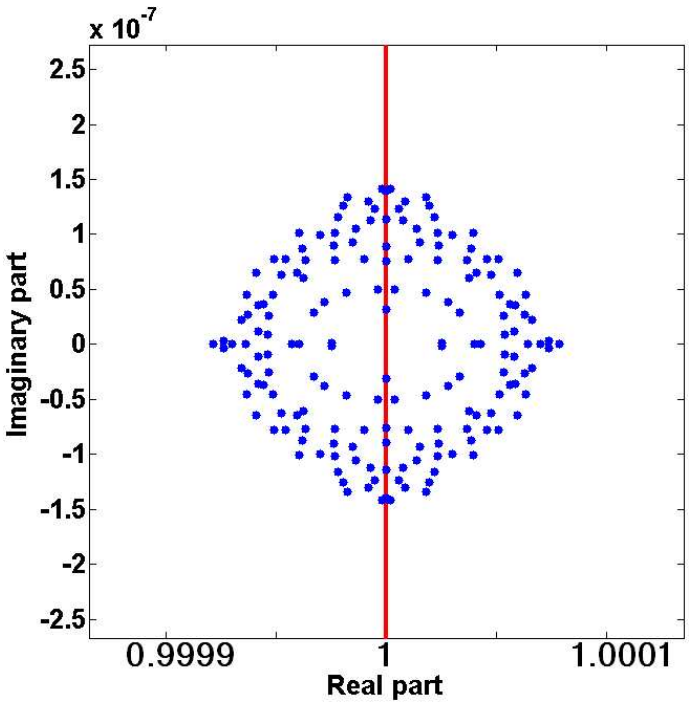

Figure 4.1: Polynomial eigenvalues of differentiated TDEFIE (applied to the sphere in Fig. 4.2(a)) near $1+0i$ in the complex plane (note the scale along both axes). Their number is equal to the number of linearly independent solenoidal currents spanned by the spatial basis functions $\boldsymbol{f}_n^{RWG}$.

In the absence of discretization errors, the spectrum of $\dot{\dot{\mathbf{T}}}_C$ would contain N_{sol} incomplete eigenvalues $1+0i$, each corresponding to a Jordan block of size 2, producing N_{sol} incomplete eigenvectors describing constant functions plus an additional N_{sol} one describing linear functions. In practice, that is, in the presence of discretization errors, this does not happen since linear functions are not in the span of the temporal basis functions $T(t)$. As a consequence, the polynomial spectrum of $\dot{\dot{\mathbf{T}}}$ shows an eigenvalue constellation of $2N_{sol}$ polynomial complete eigenvalues symmetrically distributed around $1+0i$ (Fig. 4.1). This pattern is understood from the exponential approximation of a linear curve

$$t = \frac{e^t - e^{-t}}{2} + O(t^2), \quad t \to 0,\, t \in \mathbb{C}. \tag{4.25}$$

since $e^0 = 1+0i$. A direct consequence of this observation is that half of the

constellation resides *outside* the unit circle; this effect becomes more outspoken for increasing Δt. For this reason it is desiderable to construct an equation that does not have these eigenvalues in the polynomial spectrum. Instabilities of the MOT-TDEFIE and its differentiated version associated with eigenvalues $1 + 0i$ are termed *DC instabilities*.

It is also well-known that both the time domain EFIE and the differentiated time domain EFIE admit resonant currents as solution of the undriven problem [44]. This is an immediate consequence of the continuity of the tangential component of the electric field across medium interfaces. This continuity implies that both (4.4) and (4.13) are valid equations for the internal problem, as well [14]. In other words, the *spurious* resonant currents of the exterior problem are exactly the *physical* resonant currents of the internal one. In the absence of discretization errors, the Z-transform-like mapping yields a polynomial eigenvalue of the form $\lambda = e^{i\theta}$, $\theta \neq 0$ for each of these resonances. The error introduced by the discretization, however, can shift these poles outside the unit circle[43]. For this reason, it is desiderable to construct an equation that does not have these eigenvalues in the polynomial spectrum. Instabilities of the TDEFIE and of the differentiated TDEFIE associated with these eigenvalues will be termed *resonant instabilities*.

It could be argued that the instabilities evidenced in (4.22) cannot be physically excited when casual incident fields generated by an external source are used to drive (4.4); however, this excitation occurs in practice due to errors introduced by the discretization.

4.2 A DC stable EFIE

To construct a TDEFIE that upon discretization is immune to DC instabilities, define the operators

$$\tilde{\mathcal{T}}_h[\boldsymbol{F}](\boldsymbol{r},t) = \frac{c}{4\pi}\hat{\boldsymbol{n}} \times \int_\Gamma dS' \nabla \frac{\nabla'_s \cdot \boldsymbol{F}(\boldsymbol{r}',t)}{R} \tag{4.26}$$

$$\tilde{\mathcal{T}}_s[\boldsymbol{F}](\boldsymbol{r},t) = -\frac{1}{4\pi c}\hat{\boldsymbol{n}} \times \int_\Gamma \mathrm{d}S' \frac{\boldsymbol{F}(\boldsymbol{r}',t-R/c)}{R}. \tag{4.27}$$

The equalities

$$\mathcal{T}_h\mathcal{T}_s = \tilde{\mathcal{T}}_h\tilde{\mathcal{T}}_s \tag{4.28}$$

$$\mathcal{T}_s\mathcal{T}_h = \tilde{\mathcal{T}}_s\tilde{\mathcal{T}}_h \tag{4.29}$$

hold as spatial integrations and temporal differentiations in (4.2) and (4.3) commute. Using (4.28)-(4.29) and $\mathcal{T}_h^2 = 0$, $\mathcal{T}^2$ can be expressed as

$$\mathcal{T}^2 = \mathcal{T}_s^2 + \mathcal{T}_h\mathcal{T}_s + \mathcal{T}_s\mathcal{T}_h + \mathcal{T}_h^2 = \mathcal{T}_s^2 + \tilde{\mathcal{T}}_h\tilde{\mathcal{T}}_s + \tilde{\mathcal{T}}_s\tilde{\mathcal{T}}_h. \tag{4.30}$$

Equation (4.30) suggests discretization of the modified equation, henceforth termed the "dottrick TDEFIE",

$$0 = \mathcal{T}[\hat{\boldsymbol{n}}_{\boldsymbol{r}} \times \boldsymbol{E}^i](\boldsymbol{r},t) + \eta\left(\mathcal{T}_s^2 + \tilde{\mathcal{T}}_h\tilde{\mathcal{T}}_s + \tilde{\mathcal{T}}_s\tilde{\mathcal{T}}_h\right)[\boldsymbol{J}](\boldsymbol{r},t) \tag{4.31}$$

as

$$\left(\bar{\bar{\mathbf{T}}}_s\bar{\bar{\mathbf{G}}}^{-1}\bar{\bar{\mathbf{T}}}_s + \bar{\bar{\bar{\mathbf{T}}}}_h\bar{\bar{\mathbf{G}}}^{-1}\bar{\bar{\bar{\mathbf{T}}}}_s + \bar{\bar{\bar{\mathbf{T}}}}_s\bar{\bar{\mathbf{G}}}^{-1}\bar{\bar{\bar{\mathbf{T}}}}_h\right)\bar{\mathbf{J}} = \bar{\bar{\mathbf{T}}}\bar{\mathbf{E}}. \tag{4.32}$$

Here $\bar{\bar{\mathbf{T}}}_s$, $\bar{\bar{\bar{\mathbf{T}}}}_h$, and $\bar{\bar{\bar{\mathbf{T}}}}_s$ are defined as

$$\bar{\bar{\mathbf{T}}}_s = \begin{pmatrix} \bar{\bar{\mathbf{T}}}_{s0} & & & \\ \bar{\bar{\mathbf{T}}}_{s1} & \bar{\bar{\mathbf{T}}}_{s0} & & \\ \bar{\bar{\mathbf{T}}}_{s2} & \bar{\bar{\mathbf{T}}}_{s1} & \bar{\bar{\mathbf{T}}}_{s0} & \\ \vdots & \vdots & \vdots & \ddots \end{pmatrix}, \tag{4.33}$$

$$\bar{\bar{\mathbf{T}}}_h = \begin{pmatrix} \bar{\bar{\mathbf{T}}}_{h0} & & & \\ \bar{\bar{\mathbf{T}}}_{h1} & \bar{\bar{\mathbf{T}}}_{h0} & & \\ \bar{\bar{\mathbf{T}}}_{h2} & \bar{\bar{\mathbf{T}}}_{h1} & \bar{\bar{\mathbf{T}}}_{h0} & \\ \vdots & \vdots & \vdots & \ddots \end{pmatrix}, \tag{4.34}$$

$$\bar{\bar{\mathbf{T}}}_s = \begin{pmatrix} \bar{\bar{\mathbf{T}}}_{s0} & & & \\ \bar{\bar{\mathbf{T}}}_{s1} & \bar{\bar{\mathbf{T}}}_{s0} & & \\ \bar{\bar{\mathbf{T}}}_{s2} & \bar{\bar{\mathbf{T}}}_{s1} & \bar{\bar{\mathbf{T}}}_{s0} & \\ \vdots & \vdots & \vdots & \ddots \end{pmatrix}, \tag{4.35}$$

where

$$\begin{aligned}
(\bar{\bar{\mathbf{T}}}_{sk})_{m,n} &= \left\langle \delta(t-j\Delta t)\hat{\boldsymbol{n}} \times \boldsymbol{f}_m^{RWG}(\boldsymbol{r})\, |\mathcal{T}_s|\, T_{j-k}^{LAG}(t) \boldsymbol{f}_n^{RWG}(\boldsymbol{r}) \right\rangle \\
&= -\frac{1}{4\pi c} \iint_{\Gamma^2} dS dS' \boldsymbol{f}_m^{RWG}(\boldsymbol{r}) \cdot \boldsymbol{f}_n^{RWG}(\boldsymbol{r}') \frac{\dot{T}^{LAG}(k\Delta t - R/c)}{R}, \qquad (4.36) \\
(\bar{\bar{\mathbf{T}}}_{hk})_{m,n} &= \left\langle \delta(t-j\Delta t)\hat{\boldsymbol{n}} \times \boldsymbol{f}_m^{RWG}(\boldsymbol{r}) \left| \tilde{\mathcal{T}}_h \right| T_{j-k}^{LAG}(t) \boldsymbol{f}_n^{RWG}(\boldsymbol{r}) \right\rangle \\
&= -\frac{c}{4\pi} \iint_{\Gamma^2} dS dS' \nabla_s \cdot \boldsymbol{f}_m^{RWG}(\boldsymbol{r}) \nabla'_s \cdot \boldsymbol{f}_n^{RWG}(\boldsymbol{r}') \frac{T^{LAG}(k\Delta t - R/c)}{R}, \qquad (4.37) \\
(\bar{\bar{\mathbf{T}}}_{sk})_{m,n} &= \left\langle \delta(t-j\Delta t)\hat{\boldsymbol{n}} \times \boldsymbol{f}_m^{RWG}(\boldsymbol{r}) \left| \tilde{\mathcal{T}}_s \right| T_{j-k}^{LAG}(t) \boldsymbol{f}_n^{RWG}(\boldsymbol{r}) \right\rangle \\
&= -\frac{1}{4\pi c} \iint_{\Gamma^2} dS dS' \boldsymbol{f}_m^{RWG}(\boldsymbol{r}) \cdot \boldsymbol{f}_n^{RWG}(\boldsymbol{r}') \frac{T^{LAG}(k\Delta t - R/c)}{R}. \qquad (4.38)
\end{aligned}$$

The matrix $\bar{\bar{\mathbf{G}}}$ is

$$\bar{\bar{\mathbf{G}}} = \begin{pmatrix} \bar{\bar{\mathbf{G}}}_0 & & & \\ & \bar{\bar{\mathbf{G}}}_0 & & \\ & & \bar{\bar{\mathbf{G}}}_0 & \\ & & & \ddots \end{pmatrix}, \tag{4.39}$$

where $\bar{\bar{\mathbf{G}}}_0$ is a properly chosen Gram matrix. The choice of $\bar{\bar{\mathbf{G}}}$ is a delicate issue addressed in [16].

Equation (4.32) has several advantages over (4.12) and its differentiated version. First, (4.32) can be solved rapidly by iterative solvers (because of arguments like the

ones presented in [16]). Second, it contains no temporal integral and therefore can be conveniently implemented. And third, as will be shown next, it is immune to DC instabilities: given a static or linear-in-time $\boldsymbol{J}(\boldsymbol{r},t)$ satisfying

$$\left(\mathcal{T}_s^2+\tilde{\mathcal{T}}_h\tilde{\mathcal{T}}_s+\tilde{\mathcal{T}}_s\tilde{\mathcal{T}}_h\right)[\boldsymbol{J}](\boldsymbol{r},t)=0 \quad \Rightarrow \quad \boldsymbol{J}(\boldsymbol{r},t)=0. \tag{4.40}$$

In other words, the static and linear-in-time null spaces of $\mathcal{T}$ and $\dot{\mathcal{T}}$ are not present in $\mathcal{T}_s^2+\tilde{\mathcal{T}}_h\tilde{\mathcal{T}}_s+\tilde{\mathcal{T}}_s\tilde{\mathcal{T}}_h$, and (4.31) is a DC-stable equation.

It is sufficient to prove (4.40) only for static currents $\boldsymbol{J}(\boldsymbol{r},t)=\boldsymbol{J}(\boldsymbol{r})$. Indeed, if $\boldsymbol{J}(\boldsymbol{r},t)$ is linear-in-time then

$$\left(\mathcal{T}_s^2+\tilde{\mathcal{T}}_h\tilde{\mathcal{T}}_s+\tilde{\mathcal{T}}_s\tilde{\mathcal{T}}_h\right)[\boldsymbol{J}](\boldsymbol{r},t)=0 \tag{4.41}$$

implies

$$\partial_t\left(\mathcal{T}_s^2+\tilde{\mathcal{T}}_h\tilde{\mathcal{T}}_s+\tilde{\mathcal{T}}_s\tilde{\mathcal{T}}_h\right)[\boldsymbol{J}](\boldsymbol{r},t)=\left(\mathcal{T}_s^2+\tilde{\mathcal{T}}_h\tilde{\mathcal{T}}_s+\tilde{\mathcal{T}}_s\tilde{\mathcal{T}}_h\right)[\partial_t\boldsymbol{J}](\boldsymbol{r},t)=0. \tag{4.42}$$

Once (4.40) is enstablished for static currents and since $\partial_t\boldsymbol{J}(\boldsymbol{r},t)$ is static

$$\tilde{\mathcal{T}}_h\tilde{\mathcal{T}}_s[\partial_t\boldsymbol{J}](\boldsymbol{r},t)=0\Rightarrow\partial_t\boldsymbol{J}(\boldsymbol{r},t)=0\Rightarrow\boldsymbol{J}(\boldsymbol{r},t)\,\text{is static.} \tag{4.43}$$

To demonstrate (4.40) for static $\boldsymbol{J}(\boldsymbol{r})$, note that for such current $\mathcal{T}_s^2[\boldsymbol{J}](\boldsymbol{r})=0$. Condition $\left(\tilde{\mathcal{T}}_h\tilde{\mathcal{T}}_s+\tilde{\mathcal{T}}_s\tilde{\mathcal{T}}_h\right)[\boldsymbol{J}](\boldsymbol{r})=0$ implies

$$\nabla_s\cdot\left(\tilde{\mathcal{T}}_h\tilde{\mathcal{T}}_s+\tilde{\mathcal{T}}_s\tilde{\mathcal{T}}_h\right)[\boldsymbol{J}](\boldsymbol{r})=0 \tag{4.44}$$

and (since $\nabla_s\cdot\tilde{\mathcal{T}}_h\tilde{\mathcal{T}}_s[\boldsymbol{J}](\boldsymbol{r})=0$)

$$\nabla_s\cdot\tilde{\mathcal{T}}_s\tilde{\mathcal{T}}_h[\boldsymbol{J}](\boldsymbol{r})=0. \tag{4.45}$$

To proceed, the following lemma, proven at the end of this section, is needed.

Lemma: Given a simply connected surface Γ*, the operator* $\tilde{\mathcal{T}}_s$ *defined on* Γ *in (4.32), and a static tangential vector field* $\boldsymbol{f}(\boldsymbol{r})$ *with* $\nabla_s \cdot \boldsymbol{f}(\boldsymbol{r}) = 0$*, it follows that if* $\nabla_s \cdot \tilde{\mathcal{T}}_s[\boldsymbol{f}](\boldsymbol{r}) = 0$ *then* $\boldsymbol{f}(\boldsymbol{r}) = 0$*.*

Since $\nabla_s \cdot \tilde{\mathcal{T}}_h[\boldsymbol{J}](\boldsymbol{r}) = 0$, the lemma can be applied to (4.45) with $\boldsymbol{f}(\boldsymbol{r}) = \tilde{\mathcal{T}}_h[\boldsymbol{J}](\boldsymbol{r})$, yielding

$$\boldsymbol{f}(\boldsymbol{r}) = \tilde{\mathcal{T}}_h[\boldsymbol{J}](\boldsymbol{r}) = \frac{c}{4\pi}\hat{\boldsymbol{n}} \times \int_\Gamma dS' \nabla \frac{\nabla'_s \cdot \boldsymbol{J}(\boldsymbol{r}')}{R} = 0 \Rightarrow \int_\Gamma dS' \frac{\nabla'_s \cdot \boldsymbol{J}(\boldsymbol{r}')}{R} = const. \tag{4.46}$$

Note that

$$const = \int_\Gamma dS' \frac{\nabla'_s \cdot \boldsymbol{J}(\boldsymbol{r}')}{R} \propto \frac{1}{C} \int_\Gamma \nabla'_s \cdot \boldsymbol{J}(\boldsymbol{r}') dS' = 0 \tag{4.47}$$

where C is the (always positive) capacitance of Γ. Equations (4.47) and (4.46) imply

$$\nabla_s \cdot \boldsymbol{J}(\boldsymbol{r}) = 0 \tag{4.48}$$

from which it follows that $\tilde{\mathcal{T}}_s \tilde{\mathcal{T}}_h[\boldsymbol{J}](\boldsymbol{r}) = 0$. It only remains to be shown that $\tilde{\mathcal{T}}_h \tilde{\mathcal{T}}_s[\boldsymbol{J}](\boldsymbol{r}) = 0$ (with $\nabla_s \cdot \boldsymbol{J}(\boldsymbol{r}) = 0$) implies $\boldsymbol{J}(\boldsymbol{r}) = 0$. To this end, note that

$$\tilde{\mathcal{T}}_h \tilde{\mathcal{T}}_s[\boldsymbol{J}](\boldsymbol{r}) = \hat{\boldsymbol{n}} \times \int_\Gamma dS' \nabla \frac{\nabla'_s \cdot \tilde{\mathcal{T}}_s[\boldsymbol{J}](\boldsymbol{r}')}{R} = 0 \Rightarrow \int_\Gamma dS' \frac{\nabla'_s \cdot \tilde{\mathcal{T}}_s[\boldsymbol{J}](\boldsymbol{r}')}{R} = const. \tag{4.49}$$

A line of reasoning similar to that in (4.47) implies

$$\nabla_s \cdot \tilde{\mathcal{T}}_s[\boldsymbol{J}](\boldsymbol{r}) = 0. \tag{4.50}$$

It is now sufficient to reapply the lemma with $\boldsymbol{f}(\boldsymbol{r}) = \boldsymbol{J}(\boldsymbol{r})$ (recall that $\nabla_s \cdot \boldsymbol{J}(\boldsymbol{r}) = 0$) to obtain $\boldsymbol{J}(\boldsymbol{r}) = 0$. This proves that (4.31) is immune to DC instabilities.

4.2.1 Proof of the Lemma

Proof. Denote with Ω^+ and Ω^- the external and internal regions in which Γ divides $\mathbb{R}^3$. Define the vector field

$$\boldsymbol{h}(\boldsymbol{r}) = -\frac{1}{4\pi c}\nabla \times \int_\Gamma \mathrm{d}S' \frac{\boldsymbol{f}(\boldsymbol{r}')}{R} \tag{4.51}$$

and note that since $\nabla_s \cdot \boldsymbol{f}(\boldsymbol{r}) = 0$, $\boldsymbol{h}$ satisfies the Maxwell equations like the static magnetic field does. In particular, from the jump conditions of the second layer potentials [14], it follows that

$$\lim_{\boldsymbol{r}\to\boldsymbol{r}_0^+} \boldsymbol{h}(\boldsymbol{r}) - \lim_{\boldsymbol{r}\to\boldsymbol{r}_0^-} \boldsymbol{h}(\boldsymbol{r}) = \hat{\boldsymbol{n}}_{\boldsymbol{r}} \times \boldsymbol{f}(\boldsymbol{r}_0) \tag{4.52}$$

where the two limits are taken from Ω^+ and Ω^- respectively and $\boldsymbol{r}_0 \in \Gamma$. Moreover recall that $1/R = 1/\left|\boldsymbol{r} - \boldsymbol{r}'\right|$ satisfies

$$\nabla^2 \frac{1}{R} = \delta(\boldsymbol{r} - \boldsymbol{r'}). \tag{4.53}$$

From this it follows that inside and outside Γ

$$\nabla \times \boldsymbol{h}(\boldsymbol{r}) = 0 \tag{4.54}$$

thus

$$\boldsymbol{h}(\boldsymbol{r}) = \nabla\phi(\boldsymbol{r}) \quad \text{in } \Omega^+ \cup \Omega^- \tag{4.55}$$

where $\phi(\boldsymbol{r})$ is a scalar field.

Note that

$$\nabla \cdot \boldsymbol{h}(\boldsymbol{r}) = 0 \quad \text{in } \Omega^+ \cup \Omega^- \tag{4.56}$$

thus

$$\nabla^2\phi(\boldsymbol{r}) = 0 \quad \text{in } \Omega^+ \cup \Omega^- \tag{4.57}$$

The condition $\nabla_s \cdot \tilde{\mathcal{T}}_s[\boldsymbol{f}](\boldsymbol{r}) = 0$ and (4.55) imply

$$\nabla_s \cdot \tilde{\mathcal{T}}_s[\boldsymbol{f}](\boldsymbol{r}) = \hat{\boldsymbol{n}}_{\boldsymbol{r}} \cdot \boldsymbol{h}(\boldsymbol{r}) = \frac{\partial \phi}{\partial n}(\boldsymbol{r}) = 0 \tag{4.58}$$

that together with (4.57) and since Γ is simply connected gives

$$\phi(\boldsymbol{r}) = const \quad \text{in } \Omega^+ \cup \Omega^- \tag{4.59}$$

thus

$$\boldsymbol{h}(\boldsymbol{r}) = 0 \quad \text{in } \Omega^+ \cup \Omega^- \tag{4.60}$$

From (4.52) it follows $\boldsymbol{f}(\boldsymbol{r}) = 0 \quad \forall \boldsymbol{r} \in \Gamma$ which concludes the proof. □

4.3 A resonance free equation

It is well-known that MOT resonances can be avoided by using TDCFIEs, like [44]

$$\left\{ \alpha \hat{\boldsymbol{n}}_{\boldsymbol{r}} \times \dot{\mathcal{T}} + \frac{\dot{\mathcal{I}}}{2} + \dot{\mathcal{K}} \right\} [\boldsymbol{J}](\boldsymbol{r}, t) = \left\{ -\frac{\alpha}{\eta} \hat{\boldsymbol{n}}_{\boldsymbol{r}} \times \hat{\boldsymbol{n}}_{\boldsymbol{r}} \times \dot{\boldsymbol{E}}^i(\boldsymbol{r}, t) + \hat{\boldsymbol{n}}_{\boldsymbol{r}} \times \dot{\boldsymbol{H}}^i(\boldsymbol{r}, t) \right\}. \tag{4.61}$$

Here α is a positive constant, $\boldsymbol{H}^i(\boldsymbol{r}, t)$ is the incident magnetic field, and $\mathcal{K}$ is defined as

$$\mathcal{K}[\boldsymbol{F}](\boldsymbol{r}, t) = -\hat{\boldsymbol{n}} \times \frac{1}{4\pi} \int_\Gamma dS' \nabla \times \frac{\boldsymbol{F}(\boldsymbol{r}', t - R/c)}{R}. \tag{4.62}$$

Equation (4.61) can be discretized just like TDEFIE; the discretized TDCFIE reads

$$\left(\alpha \dot{\bar{\mathbf{T}}} + \frac{\dot{\bar{\mathbf{I}}}}{2} + \dot{\bar{\mathbf{K}}} \right) \bar{\mathbf{J}} = \alpha \dot{\bar{\mathbf{E}}} + \dot{\bar{\mathbf{H}}}. \tag{4.63}$$

where $\dot{\bar{\mathbf{T}}}$ is defined in Section 4.1,

$$\dot{\bar{\mathbf{K}}} = \begin{pmatrix} \dot{\bar{\mathbf{K}}}_0 & & & \\ \dot{\bar{\mathbf{K}}}_1 & \dot{\bar{\mathbf{K}}}_0 & & \\ \dot{\bar{\mathbf{K}}}_2 & \dot{\bar{\mathbf{K}}}_1 & \dot{\bar{\mathbf{K}}}_0 & \\ \vdots & \vdots & \vdots & \ddots \end{pmatrix}, \tag{4.64}$$

and

$$\dot{\bar{\bar{\mathbf{I}}}} = \begin{pmatrix} \dot{\bar{\bar{\mathbf{I}}}}_0 & & & \\ \dot{\bar{\bar{\mathbf{I}}}}_1 & \dot{\bar{\bar{\mathbf{I}}}}_0 & & \\ \dot{\bar{\bar{\mathbf{I}}}}_2 & \dot{\bar{\bar{\mathbf{I}}}}_1 & \dot{\bar{\bar{\mathbf{I}}}}_0 & \\ \vdots & \vdots & \vdots & \ddots \end{pmatrix}, \tag{4.65}$$

with

$$\begin{aligned} (\dot{\bar{\bar{\mathbf{K}}}}_k)_{m,n} &= \left\langle \delta(t - j\Delta t) \boldsymbol{f}_m^{RWG}(\boldsymbol{r}) \, |\mathcal{K}| \, T_{j-k}^{LAG}(t) \boldsymbol{f}_n^{RWG}(\boldsymbol{r}) \right\rangle \\ &= -\frac{1}{4\pi} \int_\Gamma dS \boldsymbol{f}_m^{RWG}(\boldsymbol{r}) \cdot \hat{\boldsymbol{n}}_{\boldsymbol{r}} \times \int_\Gamma dS' \nabla \times \frac{\boldsymbol{f}_n^{RWG}(\boldsymbol{r}') \dot{T}^{LAG}(k\Delta t - R/c)}{R}, \end{aligned} \tag{4.66}$$

and

$$\begin{aligned} (\dot{\bar{\bar{\mathbf{I}}}}_k)_{m,n} &= \left\langle \delta(t - j\Delta t) \boldsymbol{f}_m^{RWG}(\boldsymbol{r}) \, |\mathcal{I}| \, T_{j-k}^{LAG}(t) \boldsymbol{f}_n^{RWG}(\boldsymbol{r}) \right\rangle \\ &= -\frac{T^{LAG}(k\Delta t)}{4\pi} \int_\Gamma dS \boldsymbol{f}_m^{RWG}(\boldsymbol{r}) \cdot \boldsymbol{f}_n^{RWG}(\boldsymbol{r}). \end{aligned} \tag{4.67}$$

Unfortunately the condition number of the system matrix in (4.63) grows linearly with the inverse of the average edge length in the mesh, this due to the discontinuous nature of $\dot{\mathcal{T}}$ [16]. Since $\frac{\dot{\mathcal{I}}}{2} + \dot{\mathcal{K}}$ is a continuous operator, the discontinuity of $\dot{\mathcal{T}}$ is inherited by $\left(\alpha \hat{\boldsymbol{n}}_{\boldsymbol{r}} \times \dot{\mathcal{T}} + \frac{\dot{\mathcal{I}}}{2} + \dot{\mathcal{K}}\right)$, which explains the behavior of the condition number. As explained in [16], the operator $\dot{\mathcal{T}}^2$ is continuous, consequently it is tempting to modify (4.61) into

$$\left\{ \alpha \dot{\mathcal{T}}^2 + \frac{\dot{\mathcal{I}}}{2} + \dot{\mathcal{K}} \right\} [\boldsymbol{J}](\boldsymbol{r}, t) = \left\{ -\frac{\alpha}{\eta} \dot{\mathcal{T}} [\hat{\boldsymbol{n}}_{\boldsymbol{r}} \times \dot{\boldsymbol{E}}^i](\boldsymbol{r}, t) + \hat{\boldsymbol{n}}_{\boldsymbol{r}} \times \dot{\boldsymbol{H}}^i(\boldsymbol{r}, t) \right\}. \tag{4.68}$$

Unfortunately, the frequency domain counterpart of (4.68) still supports spurious resonances [2], and this behavior is inherited by (4.68) as

$$\dot{\mathcal{T}}^2 = \left(\frac{\dot{\mathcal{I}}}{2} - \dot{\mathcal{K}} \right) \left(\frac{\dot{\mathcal{I}}}{2} + \dot{\mathcal{K}} \right). \tag{4.69}$$

In other words $\dot{\mathcal{T}}^2$ shares its eigenvectors with $\left(\frac{\dot{\mathcal{I}}}{2}+\dot{\mathcal{K}}\right)$ and consequently (4.68) remains a resonant equation. In the frequency domain this problem has been solved by using localized EFIE operators [2, 52, 8]. This suggests that $\dot{\mathcal{T}}^2$ in (4.68) should be replaced by the product $\dot{\mathcal{T}}_{loc}\dot{\mathcal{T}}$, where $\dot{\mathcal{T}}_{loc}$ is a properly modified version of $\dot{\mathcal{T}}$ so that

1. $\dot{\mathcal{T}}_{loc}\dot{\mathcal{T}}$ maintains the regular behavior of $\dot{\mathcal{T}}^2$, and
2. $\dot{\mathcal{T}}_{loc}\dot{\mathcal{T}}$ does not share eigenvectors with $\left(\frac{\dot{\mathcal{I}}}{2}+\dot{\mathcal{K}}\right)$.

This desired localization can be achieved by using the operator $\mathcal{T}_{loc}$ defined as

$$\mathcal{T}_{loc}\left[\boldsymbol{F}\right](\boldsymbol{r},t) = -\frac{1}{4\pi c}\hat{\boldsymbol{n}}\times\int_{\Gamma} dS' \frac{\ddot{\boldsymbol{F}}(\boldsymbol{r}',t)}{R} + \frac{c}{4\pi}\hat{\boldsymbol{n}}\times\int_{\Gamma} dS' \nabla \frac{\nabla'_s\cdot\boldsymbol{F}(\boldsymbol{r}',t)}{R}. \tag{4.70}$$

This operator can be considered a localized TDEFIE operator in the sense that the integral kernel involves the static Green function $1/R$, which does not allow for radiation. Therefore, a current localized to a region is mapped by $\mathcal{T}_{loc}$ into a field that is still local to that region.

Equation (4.70) is discretized as[1]

$$\dot{\bar{\bar{\mathbf{T}}}}_{loc} = \begin{pmatrix} \dot{\bar{\bar{\mathbf{T}}}}_0 & & & \\ & \dot{\bar{\bar{\mathbf{T}}}}_0 & & \\ & & \dot{\bar{\bar{\mathbf{T}}}}_0 & \\ & & & \ddots \end{pmatrix}, \tag{4.71}$$

where

$$\begin{aligned} (\dot{\bar{\bar{\mathbf{T}}}}_0)_{m,n} &= \left\langle \delta(t)\hat{\boldsymbol{n}}\times\boldsymbol{f}_m^{RWG}(\boldsymbol{r})\left|\mathcal{T}_{loc}\right|T_{j-k}^{LAG}(t)\boldsymbol{f}_n^{RWG}(\boldsymbol{r})\right\rangle \\ &= -\frac{1}{4\pi c}\iint_{\Gamma^2} dSdS' \boldsymbol{f}_m^{RWG}(\boldsymbol{r})\cdot\boldsymbol{f}_n^{RWG}(\boldsymbol{r}')\frac{\ddot{T}^{LAG}(-R/c)}{R} \\ &\quad -\frac{c}{4\pi}\iint_{\Gamma^2} dSdS' \nabla_s\cdot\boldsymbol{f}_m^{RWG}(\boldsymbol{r})\nabla'_s\cdot\boldsymbol{f}_n^{RWG}(\boldsymbol{r}')\frac{T^{LAG}(-R/c)}{R} \end{aligned} \tag{4.72}$$

[1]The discretization of (4.70) is only approximately diagonal, however for the purposes of this paragraph, it is advantageous to neglect the non-diagonal blocks

and the discretized $\mathcal{T}_{loc}\dot{\mathcal{T}}$ is

$$\dot{\bar{\bar{\mathbf{T}}}}_{loc}\bar{\bar{\mathbf{G}}}^{-1}\dot{\bar{\bar{\mathbf{T}}}} = \begin{pmatrix} \dot{\bar{\bar{\mathbf{T}}}}_0\bar{\bar{\mathbf{G}}}_0^{-1}\dot{\bar{\bar{\mathbf{T}}}}_0 & & & \\ \dot{\bar{\bar{\mathbf{T}}}}_0\bar{\bar{\mathbf{G}}}_0^{-1}\dot{\bar{\bar{\mathbf{T}}}}_1 & \dot{\bar{\bar{\mathbf{T}}}}_0\bar{\bar{\mathbf{G}}}_0^{-1}\dot{\bar{\bar{\mathbf{T}}}}_0 & & \\ \dot{\bar{\bar{\mathbf{T}}}}_0\bar{\bar{\mathbf{G}}}_0^{-1}\dot{\bar{\bar{\mathbf{T}}}}_2 & \dot{\bar{\bar{\mathbf{T}}}}_0\bar{\bar{\mathbf{G}}}_0^{-1}\dot{\bar{\bar{\mathbf{T}}}}_1 & \dot{\bar{\bar{\mathbf{T}}}}_0\bar{\bar{\mathbf{G}}}_0^{-1}\dot{\bar{\bar{\mathbf{T}}}}_0 & \\ \vdots & \vdots & \vdots & \ddots \end{pmatrix}. \tag{4.73}$$

Note that the companion matrix of $\mathcal{T}_{loc}\mathcal{T}$ is

$$\begin{aligned} &\left(\dot{\bar{\bar{\mathbf{T}}}}_{loc}\bar{\bar{\mathbf{G}}}^{-1}\dot{\bar{\bar{\mathbf{T}}}}\right)_C = \\ &\begin{pmatrix} -\left(\dot{\bar{\bar{\mathbf{T}}}}_0\bar{\bar{\mathbf{G}}}_0^{-1}\right)^{-1}\dot{\bar{\bar{\mathbf{T}}}}_0\bar{\bar{\mathbf{G}}}_0^{-1}\dot{\bar{\bar{\mathbf{T}}}}_1 & -\left(\dot{\bar{\bar{\mathbf{T}}}}_0\bar{\bar{\mathbf{G}}}_0^{-1}\right)^{-1}\dot{\bar{\bar{\mathbf{T}}}}_0\bar{\bar{\mathbf{G}}}_0^{-1}\dot{\bar{\bar{\mathbf{T}}}}_2 & -\left(\dot{\bar{\bar{\mathbf{T}}}}_0\bar{\bar{\mathbf{G}}}_0^{-1}\right)^{-1}\dot{\bar{\bar{\mathbf{T}}}}_0\bar{\bar{\mathbf{G}}}_0^{-1}\dot{\bar{\bar{\mathbf{T}}}}_3 & \cdots \\ \bar{\bar{\mathbf{I}}} & \bar{\bar{\mathbf{I}}} & \bar{\bar{\mathbf{I}}} & \ddots \end{pmatrix} \\ &\equiv \dot{\bar{\bar{\mathbf{T}}}}_C, \end{aligned} \tag{4.74}$$

Moreover the ordinary spectrum of $\dot{\bar{\bar{\mathbf{T}}}}_{loc}\bar{\bar{\mathbf{G}}}^{-1}\dot{\bar{\bar{\mathbf{T}}}}$ equals that of $\dot{\bar{\bar{\mathbf{T}}}}^2$. In other words, the matrix $\left(\dot{\bar{\bar{\mathbf{T}}}}_{loc}\bar{\bar{\mathbf{G}}}^{-1}\dot{\bar{\bar{\mathbf{T}}}}\right)$ shares its ordinary spectrum with $\dot{\bar{\bar{\mathbf{T}}}}^2$ (thus ensuring fast convergence rates for the solution of (4.75)) and its polynomial spectrum with $\dot{\bar{\bar{\mathbf{T}}}}$ (thus ensuring that its resonances differ from those of $\frac{\dot{\bar{\bar{\mathbf{I}}}}}{2} - \dot{\bar{\bar{\mathbf{K}}}}$; in other words the conditions 1) and 2) are satisfied.

The proposed Calderón preconditioned TDCFIE therefore is

$$\left\{\alpha\mathcal{T}_{loc}\dot{\mathcal{T}} + \frac{\dot{\mathcal{I}}}{2} + \dot{\mathcal{K}}\right\}[\boldsymbol{J}](\boldsymbol{r},t) = -\frac{\alpha}{\eta}\mathcal{T}_{loc}\left[\hat{\boldsymbol{n}}_{\boldsymbol{r}} \times \dot{\boldsymbol{E}}^i\right](\boldsymbol{r},t) + \hat{\boldsymbol{n}}_{\boldsymbol{r}} \times \dot{\boldsymbol{H}}^i(\boldsymbol{r},t). \tag{4.75}$$

This equation, upon discretization reads

$$\left(\alpha\dot{\bar{\bar{\mathbf{T}}}}_{loc}\bar{\bar{\mathbf{G}}}^{-1}\dot{\bar{\bar{\mathbf{T}}}} + \frac{\dot{\bar{\bar{\mathbf{I}}}}}{2} + \dot{\bar{\bar{\mathbf{K}}}}\right)\bar{\mathbf{J}} = -\alpha\dot{\bar{\bar{\mathbf{T}}}}_{loc}\bar{\bar{\mathbf{G}}}^{-1}\dot{\bar{\bar{\mathbf{E}}}} + \dot{\bar{\bar{\mathbf{H}}}}. \tag{4.76}$$

4.4 Numerical Results

The dottrick TDEFIE (4.32) and the Calderón preconditioned TDCFIE (4.76) have been tested on the three structures of Fig. 4.2(a-c) : a sphere, an hollow

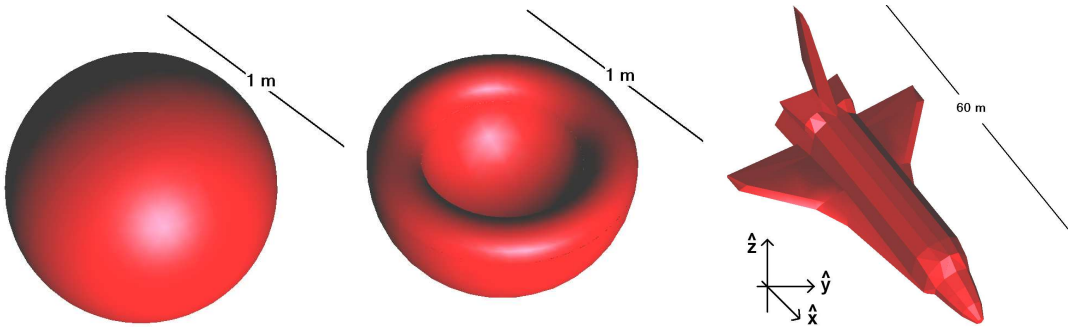

(a) Sphere (b) Hollow hemisphere (c) Space shuttle

Figure 4.2: Test Structures

	$\hat{\boldsymbol{p}}$	$\hat{\boldsymbol{k}}$	T[meter]	t_0[seconds]	Δt[seconds]
Sphere	$\hat{\boldsymbol{x}}$	$\hat{\boldsymbol{z}}$	40.0	60.0	1.0 / c
Hollow hemisphere	$\hat{\boldsymbol{y}}$	$\hat{\boldsymbol{x}}$	56.0	92.0	1.4
Space shuttle	$\hat{\boldsymbol{z}}$	$\hat{\boldsymbol{x}}$	160.0	248.0	4.0

Table 4.1: Parameters used in testing the dottrick EFIE

hemisphere, and a model of the space shuttle. For all numerical experiments the structures were excited by an incident field of the form

$$\boldsymbol{E}^i(\boldsymbol{r},t) = \frac{4}{T\sqrt{\pi}}\hat{\boldsymbol{p}}e^{-\gamma^2} \tag{4.77}$$

with

$$\gamma = \frac{4}{T}\left(c\,(t-t_0) - \hat{\boldsymbol{k}}\cdot\boldsymbol{r}\right). \tag{4.78}$$

In this equation, $\hat{\boldsymbol{p}}$ is the polarization of the incident wave, $\hat{\boldsymbol{k}}$ is the direction in which the wave is traveling, T is a measure for the spatial width of the pulse, and t_0 is the time of its arrival at the origin. The parameters used in the numerical experiments are shown in Tables 4.1 and 4.2.

4.4.1 DC instabilities

For the sphere, the current obtained with the dottrick TDEFIE (4.32) is plotted in Fig. 4.3 and compared to the one obtained with the differentiated TDEFIE (4.17).

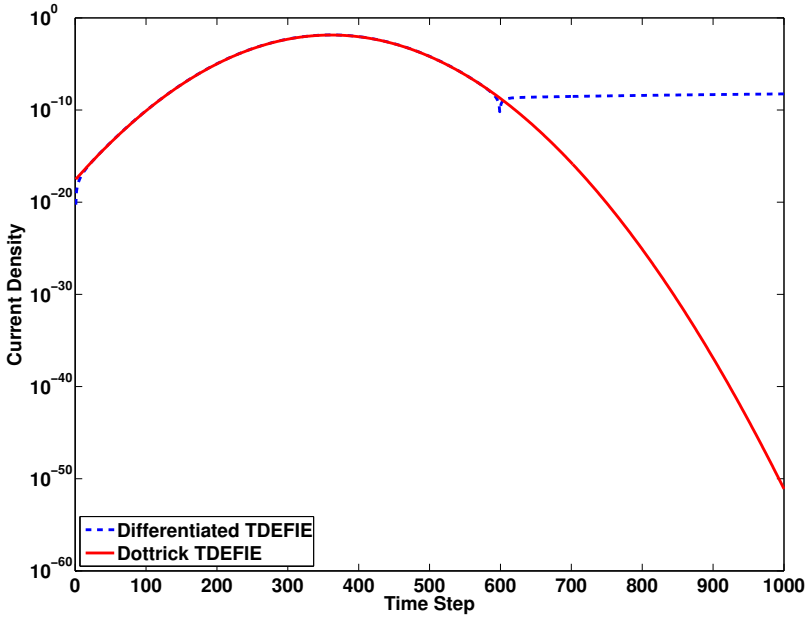

Figure 4.3: Currents on a sphere obtained with the dottrick TDEFIE and with the differentiated TDEFIE versus the time step.

It is evident that the DC instabilities apparent in the solution of the differentiated TDEFIE are not present in the solution of the dottrick TDEFIE. This is confirmed by Figs. 4.4(a-b), where the polynomial eigenvalues of both equations are depicted. Note the absence in Fig. 4.4(a) of the cluster of poles around $1 + 0i$.

A similar analysis has been performed for the hollow hemisphere and the model of the shuttle. The currents and the polynomial eigenvalues for the hollow hemisphere are plotted in Fig. 4.5 and 4.6(a-b), while for the shuttle they are in Figs. 4.7 and 4.8(a-b). All these plots demonstrate the effectiveness of the dottrick TDEFIE.

4.4.2 Resonant Instabilities

For the sphere, the currents obtained with the differentiated Calderón preconditioned TDCFIE (4.75) are plotted in Fig. 4.9 and compared to those obtained with the differentiated TDEFIE (4.17). The parameters used in the simulations can be found in Table 4.2.

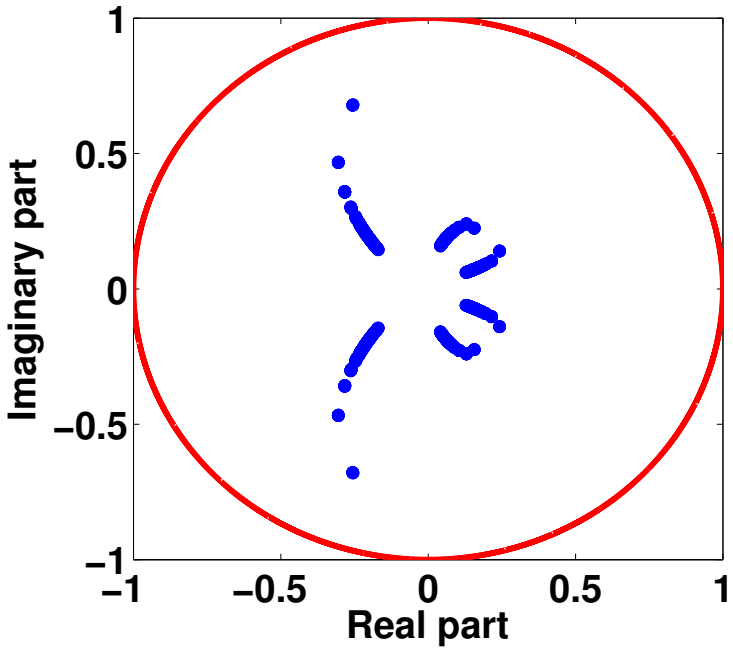

(a)

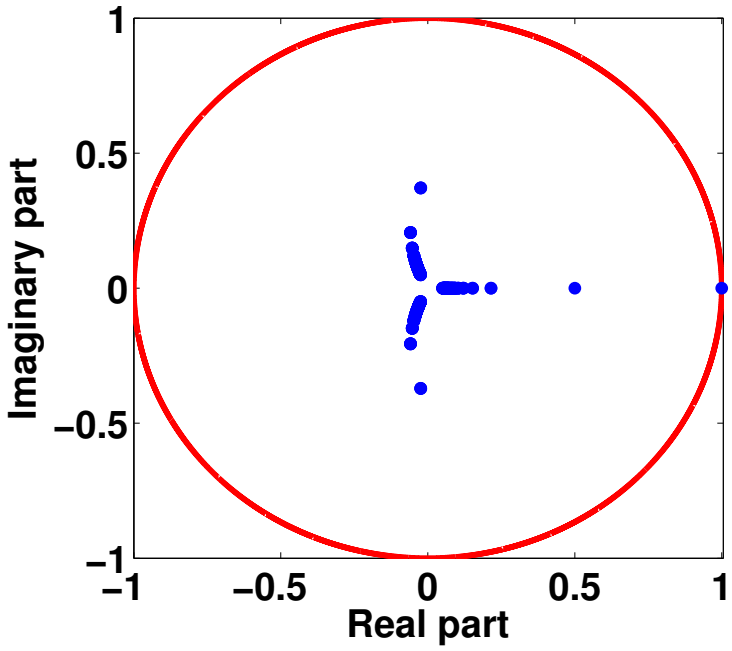

(b)

Figure 4.4: Polynomial eigenvalues of TDEFIE (a) and of the differentiated TDEFIE (b) for the sphere.

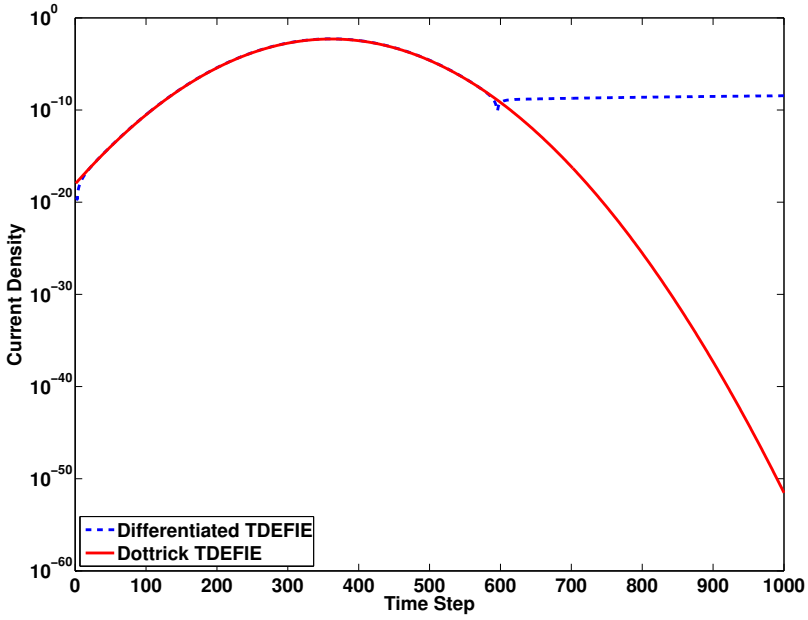

Figure 4.5: Currents on a hollow hemisphere obtained with the dottrick TDEFIE and with the differentiated TDEFIE versus the time step.

From the current plot, it can be seen that the solution of the TDEFIE is corrupted by a spurious mode. The solution of the Calderón preconditioned TDCFIE is free from this mode. In Figs. 4.10(a-b), the polynomial eigenvalues of both equations are plotted. These plots explain the differences in the solution of the TDEFIE and the Calderón preconditioned TDCFIE. In the polynomial eigenvalue plot of the TDEFIE a family of resonant poles resides near the unit circle. In the polynomial eigenvalue plot of the Calderón preconditioned TDCFIE these poles are contracted away from the unit circle.

A similar analysis has been performed for the hollow hemisphere and the model of the shuttle. The currents are plotted in Figs. 4.11 and 4.12. In all these cases the current graph shows proof of the effectiveness of the CP-CFIE. No polynomial eigenvalue plots are shown since the eigenvalue problems involved are too large to tackle using conventional solvers.

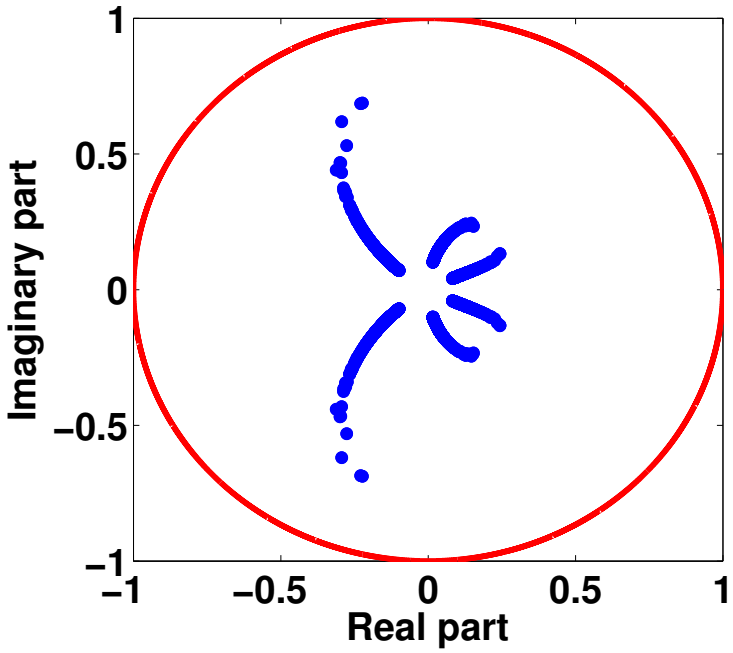

(a) Polynomial eigenvalues of the dottrick TDEFIE

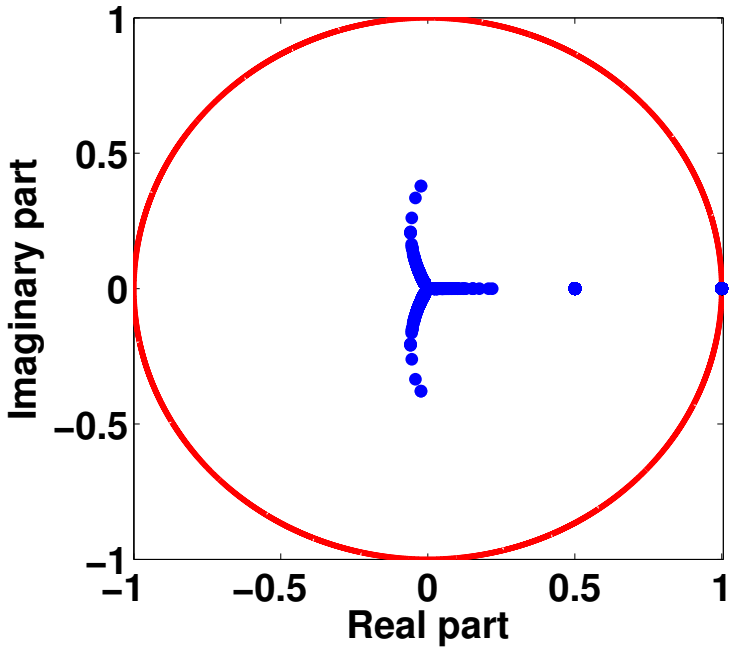

(b) Polynomial eigenvalues of the differentiated TDEFIE

Figure 4.6: Polynomial eigenvalues of TDEFIE and of the differentiated TDEFIE in the case of the hollow hemisphere.

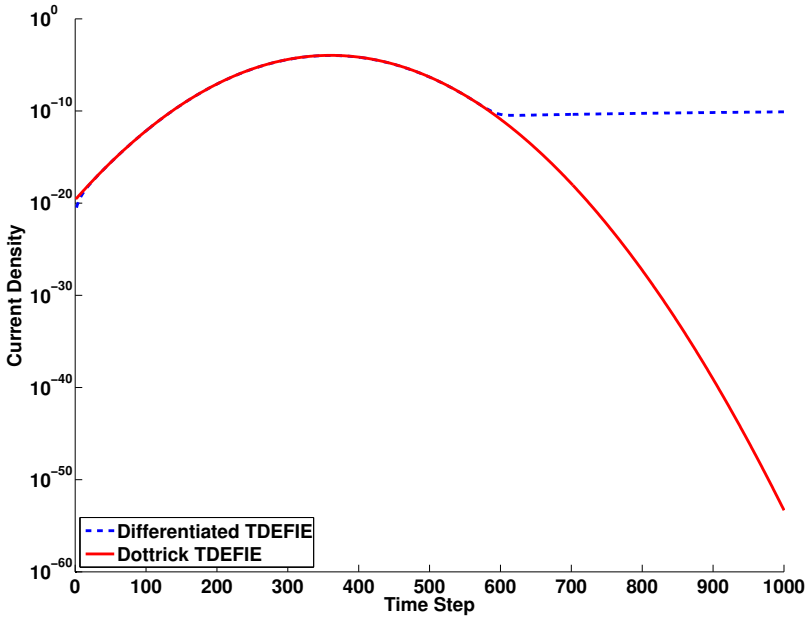

Figure 4.7: Currents on a shuttle obtained with the dottrick TDEFIE and with the differentiated TDEFIE versus the time step.

	$\hat{\boldsymbol{p}}$	$\hat{\boldsymbol{k}}$	T[meter]	t_0[seconds]	Δt[seconds]
Sphere	$\hat{\boldsymbol{x}}$	$\hat{\boldsymbol{z}}$	40.0	60.0	1.0 / c
Hollow hemisphere	$\hat{\boldsymbol{y}}$	$\hat{\boldsymbol{x}}$	56.0	92.0	1.4
Space shuttle	$\hat{\boldsymbol{z}}$	$\hat{\boldsymbol{x}}$	160.0	248.0	4.0

Table 4.2: Parameters used in testing the CP-CFIE

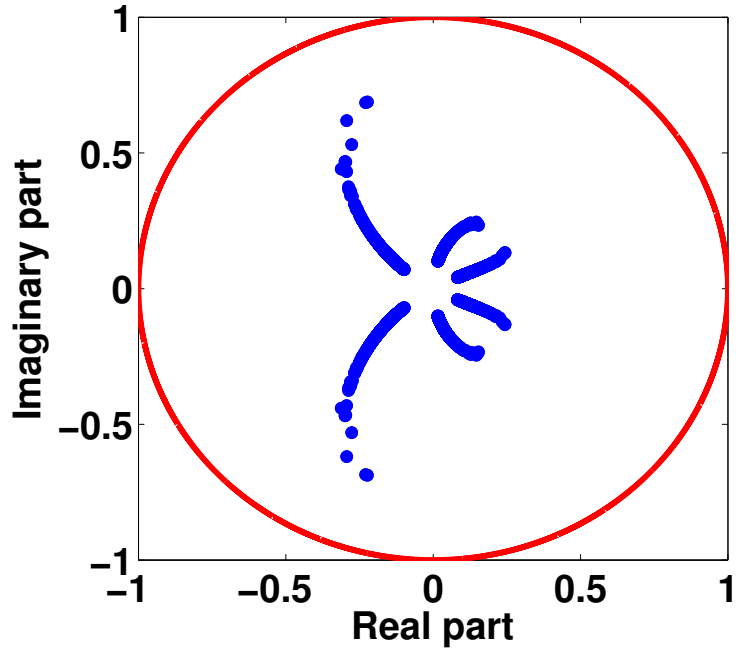

(a)

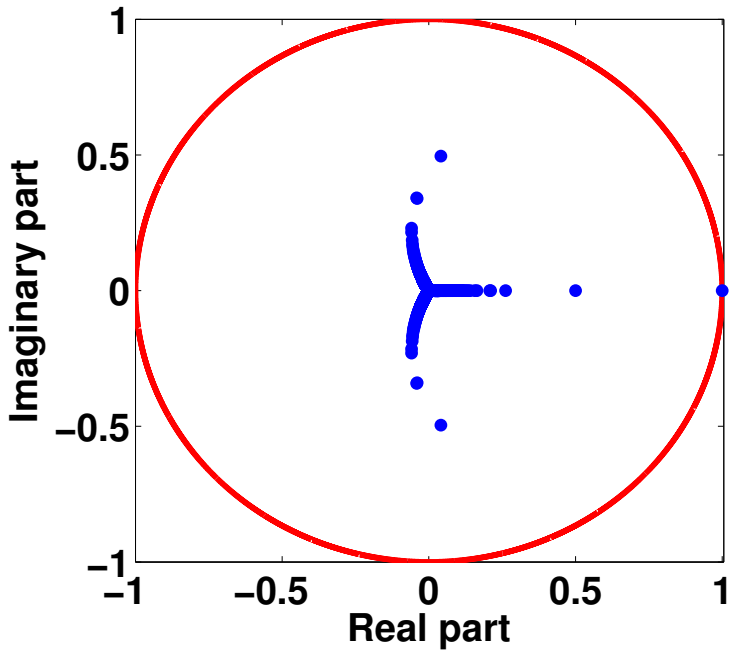

(b)

Figure 4.8: Polynomial eigenvalues of TDEFIE (a) and of the differentiated TDEFIE (b) for the shuttle.

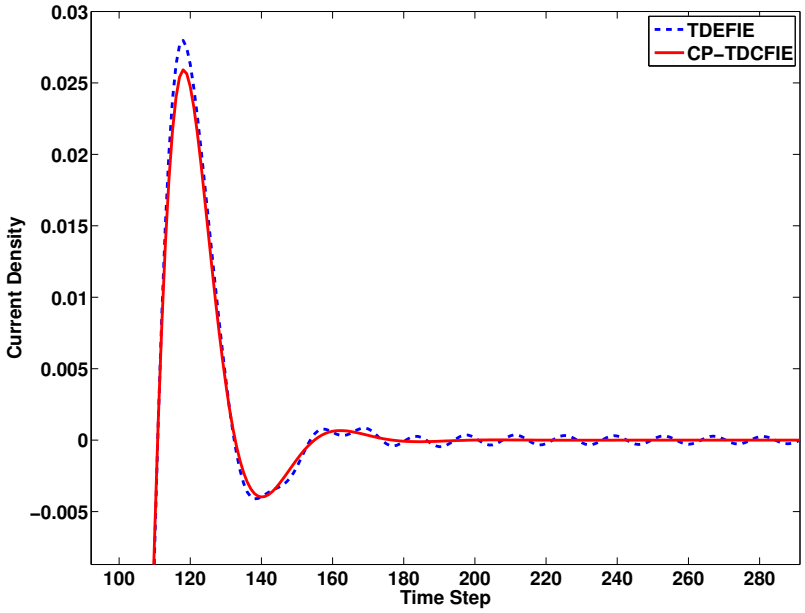

Figure 4.9: Currents on the sphere obtained with the Calderón preconditioned TDCFIE and with the differentiated TDEFIE versus the time step.

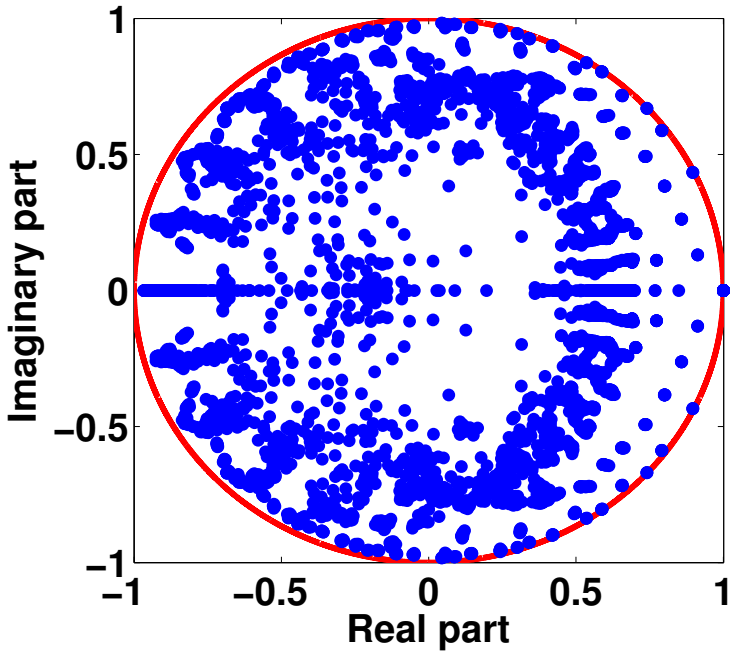

(a)

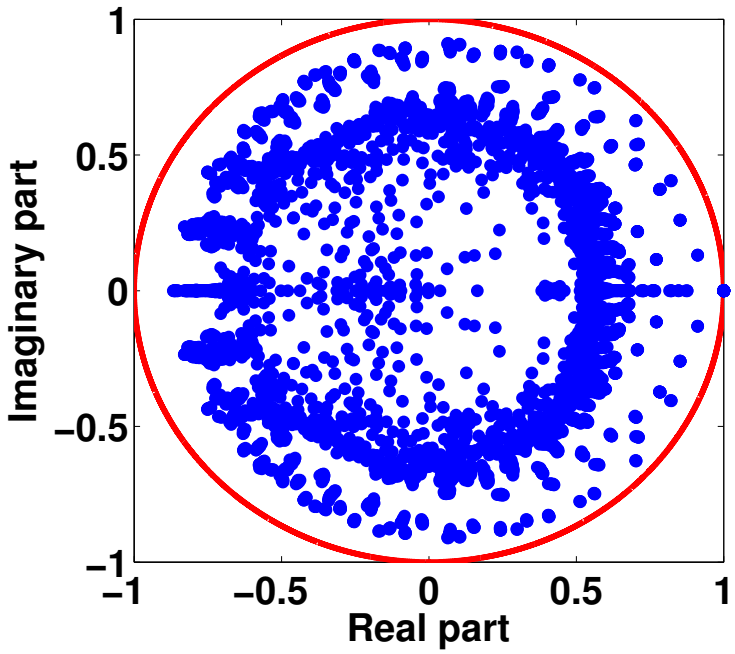

(b)

Figure 4.10: Polynomial eigenvalues of TDEFIE (a) and of the differentiated Calderón preconditioned TDCFIE (b) for the sphere.

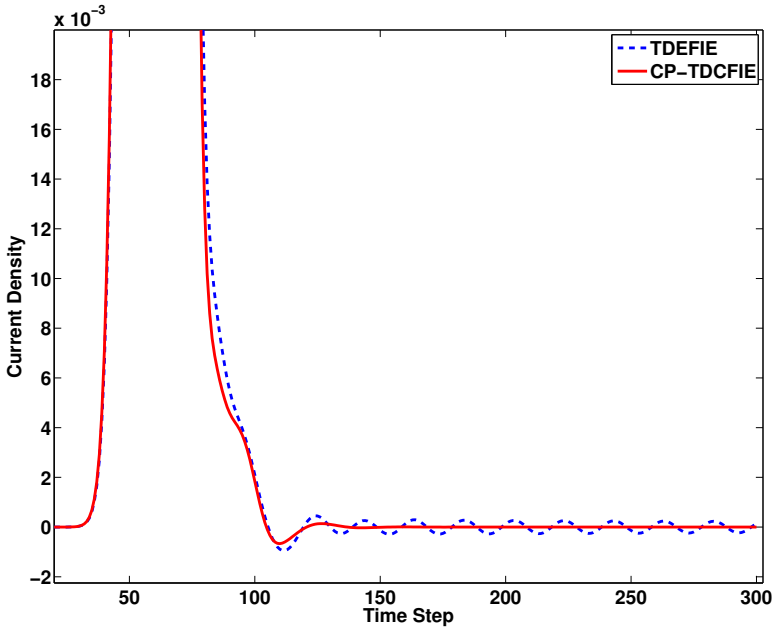

Figure 4.11: Currents on the hollow hemisphere obtained with the Calderón preconditioned TDCFIE and with the differentiated TDEFIE versus the time step.

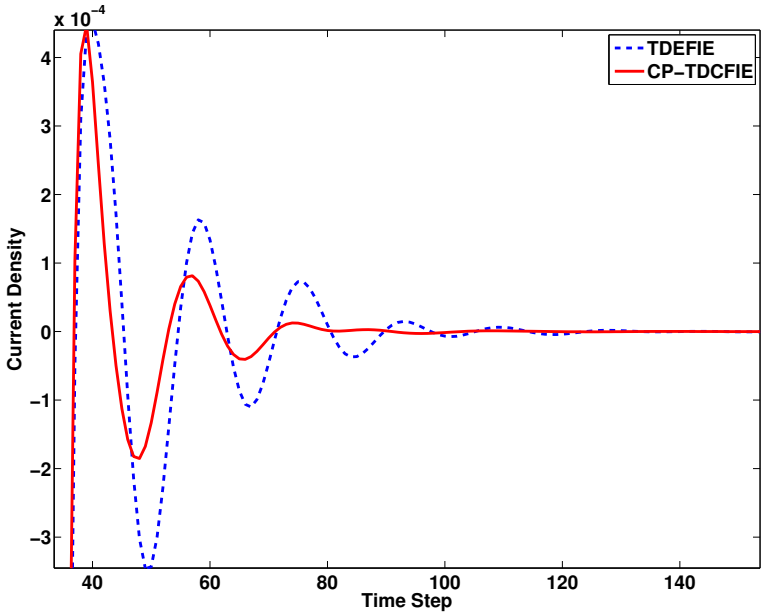

Figure 4.12: Currents on the shuttle obtained with the Calderón preconditioned TDCFIE and with the differentiated TDEFIE versus the time step.

CHAPTER V

A Marching-On-in-Time Hierarchical Scheme for the Time Domain Electric Field Integral Equation

Marching on in time TD-EFIE solvers, as seen in Chapter IV, time advance electric surface current densities by iteratively solving sparse systems of equations at each and every time step. These solvers, which are applicable to both open and closed surfaces, use spatial meshes that only need to abide by two constraints: they must resolve (i) the shortest wavelength in the excitation and (ii) the surface's geometric features. When constraint (i) drives mesh construction – this often happens when analyzing scattering from relatively smooth surfaces subject to wideband excitations – the MOT system matrix tends to be well-conditioned and the number of iterations per time step small. In contrast, when constraint (ii) drives mesh construction – this often happens when analyzing quasi-static field interactions with geometrically intricate surfaces subject to low-frequency excitations – the MOT system matrix tends to be ill-conditioned and the number of iterations per time step large. In this scenario, the MOT system matrix' condition number grows without bound as the time step size increases, severely limiting the solver's applicability to the analysis of quasi-static field interactions. This time domain low-frequency breakdown phenomenon can be mitigated in part by using appropriately scaled loop-star/tree bases [10, 54, 56, 48], which have been shown to effectively cap the MOT system matrix' condition number

as the time step size increases. Unfortunately, when these loop-star/tree bases are used on complex meshes, this cap often is prohibitively high and the iterative solution of the MOT system remains impractical [20].

This chapter presents a time domain hierarchical scheme that can be applied to arbitrary topologies giving rise to MOT TD-EFIE systems that are immune from time domain low-frequency breakdown and are rapidly converging. The development of the method is accompanied by an in-depth analysis of time domain low-frequency breakdown phenomena, which explains the poor performance of standard loop-star methods and justifies the effectiveness of the proposed method.

5.1 Formulation

Let Γ and $\hat{\boldsymbol{n}}_{\boldsymbol{r}}$ denote the surface of a PEC object and its unit normal at $\boldsymbol{r}$, respectively. Assume that Γ resides in a homogeneous medium with electric permittivity ϵ and magnetic permeability μ, and is illuminated by an electric field $\boldsymbol{E}^i(\boldsymbol{r},t)$ that is (essentially) bandlimited to temporal frequency f_{max} and vanishingly small $\forall \boldsymbol{r} \in \Gamma$ for $t \leq 0$. The electric surface current density $\boldsymbol{J}(\boldsymbol{r},t)$ induced on Γ in response to this excitation produces the scattered field [6]

$$\boldsymbol{E}^s(\boldsymbol{r},t) = -\mu \dot{\boldsymbol{A}}(\boldsymbol{J},\boldsymbol{r},t) - \nabla\phi(\boldsymbol{J},\boldsymbol{r},t), \tag{5.1}$$

where $\boldsymbol{A}(\boldsymbol{J},\boldsymbol{r},t)$ and $\phi(\boldsymbol{J},\boldsymbol{r},t)$ are the vector and scalar potentials given by

$$\boldsymbol{A}(\boldsymbol{J},\boldsymbol{r},t) = \int_\Gamma \frac{\boldsymbol{J}(\boldsymbol{r}', t - |\boldsymbol{r}-\boldsymbol{r}'|/c)}{4\pi\,|\boldsymbol{r}-\boldsymbol{r}'|}\,\mathrm{d}\boldsymbol{r}', \tag{5.2}$$

and

$$\phi(\boldsymbol{J},\boldsymbol{r},t) = -\int_\Gamma \frac{1}{4\pi\epsilon\,|\boldsymbol{r}-\boldsymbol{r}'|}\int_0^{t-|\boldsymbol{r}-\boldsymbol{r}'|/c} \nabla\cdot\boldsymbol{J}(\boldsymbol{r}',t')\,\mathrm{d}t'\,\mathrm{d}\boldsymbol{r}', \tag{5.3}$$

and $c = 1/\sqrt{\epsilon\mu}$ is the speed of light. The components tangential to Γ of $\boldsymbol{E}^s(\boldsymbol{r},t)$ and $\boldsymbol{E}^i(\boldsymbol{r},t)$ cancel one another, or

$$-\hat{\boldsymbol{n}}_{\boldsymbol{r}} \times \hat{\boldsymbol{n}}_{\boldsymbol{r}} \times \boldsymbol{E}^s(\boldsymbol{r},t) = \hat{\boldsymbol{n}}_{\boldsymbol{r}} \times \hat{\boldsymbol{n}}_{\boldsymbol{r}} \times \boldsymbol{E}^i(\boldsymbol{r},t) \quad \boldsymbol{r} \in \Gamma, \forall t > 0. \tag{5.4}$$

Taking the time derivative of (5.4), and using (5.1) yields the following TD-EFIE in $\boldsymbol{J}(\boldsymbol{r},t)$:

$$\hat{\boldsymbol{n}}_{\boldsymbol{r}} \times \hat{\boldsymbol{n}}_{\boldsymbol{r}} \times \Big(\mu\ddot{\boldsymbol{A}}(\boldsymbol{J},\boldsymbol{r},t) + \nabla\dot{\phi}(\boldsymbol{J},\boldsymbol{r},t)\Big) = \hat{\boldsymbol{n}}_{\boldsymbol{r}} \times \hat{\boldsymbol{n}}_{\boldsymbol{r}} \times \dot{\boldsymbol{E}}^i(\boldsymbol{r},t) \quad \forall \boldsymbol{r} \in \Gamma, \forall t. \tag{5.5}$$

(The extra time derivative cancels the (computationally costly) temporal integration in (5.3), thus avoiding the need to keep track of charges on Γ.)

To numerically solve (5.5), Γ is approximated by a mesh of planar triangles and the current density $\boldsymbol{J}(\boldsymbol{r},t)$ is approximated as

$$\boldsymbol{J}(\boldsymbol{r},t) \approx \sum_{j=1}^{N_t}\sum_{n=1}^{N_s} I_{j,n} T_j(t) \boldsymbol{f}_n(\boldsymbol{r}). \tag{5.6}$$

Here $\boldsymbol{f}_n(\boldsymbol{r})$, $n = 1,\ldots,N_s$, are Rao-Wilton-Glisson (RWG) basis functions [39] defined on the mesh's N_s interior edges and $T_j(t)$, $j = 1,\ldots,N_t$, are higher-order polynomial interpolants [22] satisfying $T_j(t) = T\left(t - j\Delta t\right)$ with $T(t) = 0\ \forall t < -\Delta t$. Here Δt denotes the time step size, which is related to the maximum frequency f_{max} as

$$\Delta t = \frac{1}{\alpha f_{max}}, \tag{5.7}$$

with (typically) $10 \leq \alpha \leq 20$. To determine the expansions coefficients $I_{j,n}$, (5.6) is substituted into (5.5), and the resulting equation is spatial Galerkin tested at time $t_i = i\Delta t$ yielding

$$\bar{\bar{\mathbf{Z}}}_0 \bar{\mathbf{I}}_i = \bar{\mathbf{V}}_i - \sum_{k=1}^{i-1} \bar{\bar{\mathbf{Z}}}_k \bar{\mathbf{I}}_{i-k}, \quad i = 1\ldots, N_t \tag{5.8}$$

where

$$\{\bar{\bar{\mathbf{Z}}}_k\}_{m,n} = \underbrace{\left\langle \boldsymbol{f}_m(\boldsymbol{r}), \hat{\boldsymbol{n}}_{\boldsymbol{r}} \times \hat{\boldsymbol{n}}_{\boldsymbol{r}} \times \left(\mu \ddot{\boldsymbol{A}}(\boldsymbol{f}_n \cdot T_k, \boldsymbol{r}, t)\right)\right\rangle\Big|_{t=0}}_{O(\frac{1}{\Delta t^2})} + \underbrace{\left\langle \boldsymbol{f}_m(\boldsymbol{r}), \hat{\boldsymbol{n}}_{\boldsymbol{r}} \times \hat{\boldsymbol{n}}_{\boldsymbol{r}} \times \left(\nabla \dot{\phi}(\boldsymbol{f}_n \cdot T_k, \boldsymbol{r}, t)\right)\right\rangle\Big|_{t=0}}_{O(1)}, \tag{5.9}$$

$$\{\bar{\mathbf{I}}_i\}_n = I_{i,n}, \quad \bar{\mathbf{I}}_i = \mathbf{0} \quad \text{if } i < 0, \tag{5.10}$$

$$\{\bar{\mathbf{V}}_i\}_m = \left\langle \boldsymbol{f}_m(\boldsymbol{r}), \hat{\boldsymbol{n}}_{\boldsymbol{r}} \times \hat{\boldsymbol{n}}_{\boldsymbol{r}} \times \dot{\boldsymbol{E}}^i(\boldsymbol{r}, t)\right\rangle\Big|_{t=t_i}, \tag{5.11}$$

with $\langle \boldsymbol{a}(\boldsymbol{r}, t), \boldsymbol{b}(\boldsymbol{r}, t)\rangle = \int_\Gamma \boldsymbol{a}(\boldsymbol{r}, t) \cdot \boldsymbol{b}(\boldsymbol{r}, t)\, \mathrm{d}\boldsymbol{r}$. Note that vector potential contributions to $\{\bar{\bar{\mathbf{Z}}}_k\}_{m,n}$ scale as $O(1/\Delta t^2)$ as $\Delta t \to \infty$; this behavior is due to the double temporal differentiation of $\boldsymbol{A}(\boldsymbol{J}, \boldsymbol{r}, t)$ in (5.9). Scalar potential contributions to $\{\bar{\bar{\mathbf{Z}}}_k\}_{m,n}$, in contrast, scale as $O(1)$ as $\Delta t \to \infty$; this behavior is due to the combined action of the temporal differentiation on $\phi(\boldsymbol{J}, \boldsymbol{r}, t)$ and the temporal integration of $\boldsymbol{J}(\boldsymbol{r}, t)$ in (5.3). Equation (5.8) is the discrete counterpart of (5.5) and is solved for current coefficient vector $\bar{\mathbf{I}}_i$ after the current coefficient vectors $\bar{\mathbf{I}}_j,\ j = 0, \ldots, i-1$ have been obtained. This recursive procedure is termed MOT [7].

5.2 Time domain low-frequency breakdown

For large N_s (5.8) only can be solved iteratively. The number of iterations required to achieve a prescribed accuracy in the iterative solution of (5.8) is dictated by the condition number of the MOT system matrix $\bar{\bar{\mathbf{Z}}}_0$[1]. A high condition number typically implies a large number of iterations. "Time domain low-frequency breakdown" refers to increases in $\bar{\bar{\mathbf{Z}}}_0$'s condition number when the time step size $\Delta t \to \infty$ (or equivalently when the maximum frequency $f_{max} \to 0$, hence the name). Just like its well-studied frequency domain counterpart [54, 56, 48], time domain low-frequency

[1]The condition number of a matrix is the ratio of its largest and smallest singular values [26].

breakdown is due to the divergent behavior of the vector and scalar potential contributions to the (MOT) system matrix as $f_{max} \to 0$ ($\Delta t \to \infty$).

The time domain low-frequency breakdown phenomenon is easily understood by studying MOT systems obtained by discretizing TD-EFIE (5.5) using loop-star basis functions [56, 48]. To simplify the presentation, it is assumed that Γ is connected and without holes; our results however remain valid even if these assumptions are violated. The set of loop functions $\Lambda = \{\boldsymbol{\Lambda}_n, n = 1, \ldots, N_l\}$ spans the space of solenoidal functions expandable by RWG functions. One loop function is associated with each of the mesh's N_l vertices. Loop function $\boldsymbol{\Lambda}_n, n = 1, \ldots, N_l$, is expressed as

$$\boldsymbol{\Lambda}_n(\boldsymbol{r}) = \sum_{p=1}^{N_n} \lambda_{n,p} \boldsymbol{f}_{n,p}(\boldsymbol{r}), \quad n = 1, \ldots, N_l \tag{5.12}$$

where the sum is over the N_n RWG functions $\boldsymbol{f}_{n,p}(\boldsymbol{r}), p = 1, \ldots, N_n$, defined on the N_n edges that share internal node n, and the coefficients $\lambda_{n,p}, p = 1 \ldots N_n$, are chosen such that $\boldsymbol{\Lambda}_n$ is solenoidal, viz. [48]

$$\nabla_s \cdot \boldsymbol{\Lambda}_n(\boldsymbol{r}) = 0. \tag{5.13}$$

The set of nonsolenoidal functions $\Sigma = \{\boldsymbol{\Sigma}_n, n = 1, \ldots, N_s - N_l\}$ complements Λ in such a way that each RWG can be written as a unique linear combination of functions in Λ and Σ. The set of star functions Σ^S [54, 48] represents a *possible* choice for Σ; star functions are defined on all cells but cell of the mesh as

$$\boldsymbol{\Sigma}_n^S(\boldsymbol{r}) = \sum_{p=1}^{N_n'} \sigma_{n,p} \boldsymbol{f}_{n,p}(\boldsymbol{r}) \quad n = 1, \ldots, N_s - N_l, \tag{5.14}$$

where the sum is over the N_n' RWG functions that share cell c_n ($1 \leq N_n \leq 3$) and the coefficients $\sigma_{n,p}, p = 1 \ldots N_n'$, equal $1/l_{n,p}$ or $-1/l_{n,p}$ with $l_{n,p}$ the length of the edge on which $\boldsymbol{f}_{n,p}(\boldsymbol{r})$ is defined, this in order to ensure that all currents $\sigma_{n,p}\boldsymbol{f}_{n,p}(\boldsymbol{r})$ flow "out of" cell c_n. The coefficients $\{\lambda_{n,p}\}, n = 1, \ldots, N_l$ and $\{\sigma_{n,p}\}, n = 1, \ldots, N_s - N_l$

can be arranged on the columns of a RWG to loop-star transformation matrix $\bar{\bar{\mathbf{T}}}$. Define the impedance matrix $\bar{\bar{\mathbf{Z}}}_0^{LS}$ with respect to the loop-star basis as

$$\bar{\bar{\mathbf{Z}}}_0^{LS} = \bar{\bar{\mathbf{T}}}^T \bar{\bar{\mathbf{Z}}}_0 \bar{\bar{\mathbf{T}}} = \begin{pmatrix} \bar{\bar{\mathbf{Z}}}_0^{\Lambda\Lambda} & \bar{\bar{\mathbf{Z}}}_0^{\Lambda\Sigma^S} \\ \bar{\bar{\mathbf{Z}}}_0^{\Sigma^S\Lambda} & \bar{\bar{\mathbf{Z}}}_0^{\Sigma^S\Sigma^S} \end{pmatrix}. \tag{5.15}$$

where

$$\{\bar{\bar{\mathbf{Z}}}_0^{\Lambda\Lambda}\}_{m,n} = \left\langle \boldsymbol{\Lambda}_m(\boldsymbol{r}), \hat{\boldsymbol{n}}_{\boldsymbol{r}} \times \hat{\boldsymbol{n}}_{\boldsymbol{r}} \times \left(\mu \ddot{\boldsymbol{A}}(\boldsymbol{\Lambda}_n \cdot T_0, \boldsymbol{r}, t)\right) \right\rangle \Big|_{t=0} = O\left(\frac{1}{\Delta^2 t}\right), \tag{5.16}$$

$$\{\bar{\bar{\mathbf{Z}}}_0^{\Lambda\Sigma^S}\}_{m,n} = \left\langle \boldsymbol{\Lambda}_m(\boldsymbol{r}), \hat{\boldsymbol{n}}_{\boldsymbol{r}} \times \hat{\boldsymbol{n}}_{\boldsymbol{r}} \times \left(\mu \ddot{\boldsymbol{A}}(\boldsymbol{\Sigma}_n^S \cdot T_0, \boldsymbol{r}, t)\right) \right\rangle \Big|_{t=0} = O\left(\frac{1}{\Delta^2 t}\right), \tag{5.17}$$

$$\{\bar{\bar{\mathbf{Z}}}_0^{\Sigma^S\Lambda}\}_{m,n} = \left\langle \boldsymbol{\Sigma}_m^S(\boldsymbol{r}), \hat{\boldsymbol{n}}_{\boldsymbol{r}} \times \hat{\boldsymbol{n}}_{\boldsymbol{r}} \times \left(\mu \ddot{\boldsymbol{A}}(\boldsymbol{\Lambda}_n \cdot T_0, \boldsymbol{r}, t)\right) \right\rangle \Big|_{t=0} = O\left(\frac{1}{\Delta^2 t}\right), \tag{5.18}$$

$$\{\bar{\bar{\mathbf{Z}}}_0^{\Sigma^S\Sigma^S}\}_{m,n} = \underbrace{\left\langle \boldsymbol{\Sigma}_m^S(\boldsymbol{r}), \hat{\boldsymbol{n}}_{\boldsymbol{r}} \times \hat{\boldsymbol{n}}_{\boldsymbol{r}} \times \left(\mu \ddot{\boldsymbol{A}}(\boldsymbol{\Sigma}_n^S \cdot T_0, \boldsymbol{r}, t)\right) \right\rangle \Big|_{t=0}}_{O(\frac{1}{\Delta t^2})} + \tag{5.19}$$

$$+ \underbrace{\left\langle \boldsymbol{\Sigma}_m^S(\boldsymbol{r}), \hat{\boldsymbol{n}}_{\boldsymbol{r}} \times \hat{\boldsymbol{n}}_{\boldsymbol{r}} \times \left(\nabla \dot{\phi}(\boldsymbol{\Sigma}_n^S \cdot T_0, \boldsymbol{r}, t)\right) \right\rangle \Big|_{t=0}}_{O(1)} = O(1).$$

Analyzing the conditioning of $\bar{\bar{\mathbf{Z}}}_0$ in (5.8) when $\Delta t \to 0$ is equivalent to analyzing the conditioning of $\bar{\bar{\mathbf{Z}}}_0^{LS}$ in (5.15). Indeed, the condition numbers $k(\bar{\bar{\mathbf{Z}}}_0)$ and $k(\bar{\bar{\mathbf{Z}}}_0^{LS})$ of $\bar{\bar{\mathbf{Z}}}_0$ and $\bar{\bar{\mathbf{Z}}}_0^{LS}$ are related as [26]

$$\frac{k(\bar{\bar{\mathbf{Z}}}_0^{LS})}{k^2(\bar{\bar{\mathbf{T}}})} \leq k(\bar{\bar{\mathbf{Z}}}_0) \leq k(\bar{\bar{\mathbf{Z}}}_0^{LS}) k^2(\bar{\bar{\mathbf{T}}}) \tag{5.20}$$

where $k(\bar{\bar{\mathbf{T}}})$ is the condition number of $\bar{\bar{\mathbf{T}}}$. Since $\bar{\bar{\mathbf{T}}}$ is independent of Δt, so is $k(\bar{\bar{\mathbf{T}}})$; hence (5.20) implies that the asymptotic behavior of $k(\bar{\bar{\mathbf{Z}}}_0^{LS})$ and $k(\bar{\bar{\mathbf{Z}}}_0)$ for $\Delta t \to \infty$ are the same.

It therefore follows from (5.16)-(5.19) and the Gerschgorin's disk theorem (Section 5.5) that

$$k(\bar{\bar{\mathbf{Z}}}_0^{LS}) = O(\Delta t^2) \quad \text{as } \Delta t \to \infty \tag{5.21}$$

and from (5.20) that

$$k(\bar{\bar{\mathbf{Z}}}_0) = O(\Delta t^2) \quad \text{as } \Delta t \to \infty. \tag{5.22}$$

5.3 Hierarchical Regularization of the TD-EFIE

Ill-conditioned linear systems often can be regularized by an appropriate basis transformation. For the above MOT TD-EFIE solver, such transformation is realized by defining the auxiliary matrices and vectors

$$\bar{\bar{\mathbf{Z}}}_k^{\bullet} = \bar{\bar{\mathbf{P}}}^T \bar{\bar{\mathbf{Z}}}_k \bar{\bar{\mathbf{P}}}, \tag{5.23}$$

$$\bar{\mathbf{I}}_i^{\bullet} = \bar{\bar{\mathbf{P}}}^{-1} \bar{\mathbf{I}}_i, \tag{5.24}$$

$$\bar{\mathbf{V}}_i^{\bullet} = \bar{\bar{\mathbf{P}}}^T \bar{\mathbf{V}}_i, \tag{5.25}$$

with $\bar{\bar{\mathbf{P}}}$ an invertible transformation matrix. Use of (5.23)-(5.25) in (5.8) yelds

$$\bar{\bar{\mathbf{Z}}}_0^{\bullet} \bar{\mathbf{I}}_i^{\bullet} = \bar{\mathbf{V}}_i^{\bullet} - \sum_{k=1}^{i-1} \bar{\bar{\mathbf{Z}}}_k^{\bullet} \bar{\mathbf{I}}_{i-k}^{\bullet}, \tag{5.26}$$

which can still be solved by MOT for the auxiliary unknown $\bar{\mathbf{I}}_i^{\bullet}$. The original solution $\bar{\mathbf{I}}_i = \bar{\bar{\mathbf{P}}} \bar{\mathbf{I}}_i^{\bullet}$ is easily recovered.

A first attempt at mitigating time domain low-frequency breakdown is to choose as $\bar{\bar{\mathbf{P}}}$ the weighted RWG-to-loop-star transformation matrix

$$\bar{\bar{\mathbf{P}}} = \left(\sqrt{\bar{\bar{\mathbf{D}}}} \right)^{-1} \bar{\bar{\mathbf{T}}} \tag{5.27}$$

where

$$\bar{\bar{\mathbf{D}}} = \begin{pmatrix} \bar{\bar{\mathbf{D}}}^{\Lambda\Lambda} & \\ & \bar{\bar{\mathbf{D}}}^{\Sigma^S\Sigma^S} \end{pmatrix}. \tag{5.28}$$

Here $\bar{\bar{\mathbf{D}}}^{\Lambda\Lambda}$ and $\bar{\bar{\mathbf{D}}}^{\Sigma^S\Sigma^S}$ contains the diagonal of $\bar{\bar{\mathbf{Z}}}^{\Lambda\Lambda}$ and $\bar{\bar{\mathbf{Z}}}^{\Sigma^S\Sigma^S}$ respectively

$$\left(\bar{\bar{\mathbf{D}}}^{\Lambda\Lambda} \right)_{m,n} = \begin{cases} \left(\bar{\bar{\mathbf{Z}}}^{\Lambda\Lambda} \right)_{m,n} = O\left(\frac{1}{\Delta t^2} \right) & \text{when } m = n \\ 0 & \text{otherwise} \end{cases}, \tag{5.29}$$

$$\left(\bar{\bar{\mathbf{D}}}^{\Sigma^S\Sigma^S} \right)_{m,n} = \begin{cases} \left(\bar{\bar{\mathbf{Z}}}^{\Sigma^S\Sigma^S} \right)_{m,n} = O\left(1 \right) & \text{when } m = n \\ 0 & \text{otherwise} \end{cases}. \tag{5.30}$$

With this choice of $\bar{\bar{\mathbf{P}}}$, it follows from (5.15) and (5.23) that

$$\bar{\bar{\mathbf{Z}}}_0^{\bullet} = \begin{pmatrix} \left(\sqrt{\bar{\bar{\mathbf{D}}}^{\Lambda\Lambda}}\right)^{-1} \bar{\bar{\mathbf{Z}}}_0^{\Lambda\Lambda} \left(\sqrt{\bar{\bar{\mathbf{D}}}^{\Lambda\Lambda}}\right)^{-1} & \left(\sqrt{\bar{\bar{\mathbf{D}}}^{\Lambda\Lambda}}\right)^{-1} \bar{\bar{\mathbf{Z}}}_0^{\Lambda\Sigma^S} \left(\sqrt{\bar{\bar{\mathbf{D}}}^{\Sigma^S\Sigma^S}}\right)^{-1} \\ \left(\sqrt{\bar{\bar{\mathbf{D}}}^{\Sigma^S\Sigma^S}}\right)^{-1} \bar{\bar{\mathbf{Z}}}_0^{\Sigma^S\Lambda} \left(\sqrt{\bar{\bar{\mathbf{D}}}^{\Lambda\Lambda}}\right)^{-1} & \left(\sqrt{\bar{\bar{\mathbf{D}}}^{\Sigma^S\Sigma^S}}\right)^{-1} \bar{\bar{\mathbf{Z}}}_0^{\Sigma^S\Sigma^S} \left(\sqrt{\bar{\bar{\mathbf{D}}}^{\Sigma^S\Sigma^S}}\right)^{-1} \end{pmatrix}. \tag{5.31}$$

It is easily verified that when $\Delta t \to \infty$

$$\left(\sqrt{\bar{\bar{\mathbf{D}}}^{\Lambda\Lambda}}\right)^{-1} \bar{\bar{\mathbf{Z}}}_0^{\Lambda\Lambda} \left(\sqrt{\bar{\bar{\mathbf{D}}}^{\Lambda\Lambda}}\right)^{-1} = O(1) \tag{5.32}$$

$$\left(\sqrt{\bar{\bar{\mathbf{D}}}^{\Lambda\Lambda}}\right)^{-1} \bar{\bar{\mathbf{Z}}}_0^{\Lambda\Sigma^S} \left(\sqrt{\bar{\bar{\mathbf{D}}}^{\Sigma^S\Sigma^S}}\right)^{-1} = O(1/\Delta t) \tag{5.33}$$

$$\left(\sqrt{\bar{\bar{\mathbf{D}}}^{\Sigma^S\Sigma^S}}\right)^{-1} \bar{\bar{\mathbf{Z}}}_0^{\Sigma^S\Lambda} \left(\sqrt{\bar{\bar{\mathbf{D}}}^{\Lambda\Lambda}}\right)^{-1} = O(1/\Delta t) \tag{5.34}$$

$$\left(\sqrt{\bar{\bar{\mathbf{D}}}^{\Sigma^S\Sigma^S}}\right)^{-1} \bar{\bar{\mathbf{Z}}}_0^{\Sigma^S\Sigma^S} \left(\sqrt{\bar{\bar{\mathbf{D}}}^{\Sigma^S\Sigma^S}}\right)^{-1} = O(1). \tag{5.35}$$

It therefore follows from the Gerschgorin's disk theorem (Section 5.5) that

$$k(\bar{\bar{\mathbf{Z}}}_0^{\bullet}) = O(1) \quad \text{as } \Delta t \to \infty. \tag{5.36}$$

Unfortunately, the condition number $k(\bar{\bar{\mathbf{Z}}}_0^{\bullet})$, though independent of Δt, often remains very high when N_s is large [20, 4]. When this happens, the iterative solution of (5.26) remains impractical. The high value of $k(\bar{\bar{\mathbf{Z}}}_0^{\bullet})$ in (5.36) is due to the presence of the hypersingular term $\nabla\dot{\phi}(\boldsymbol{J}, \boldsymbol{r}, t)$ in (5.5). In fact the asymptotic behavior of (5.16), (5.33), and (5.34) dictate that the spectrum of $\left(\sqrt{\bar{\bar{\mathbf{D}}}^{\Sigma^S\Sigma^S}}\right)^{-1} \bar{\bar{\mathbf{Z}}}_0^{\Sigma^S\Sigma^S} \left(\sqrt{\bar{\bar{\mathbf{D}}}^{\Sigma^S\Sigma^S}}\right)^{-1}$ is to be found unaltered into the spectrum of $\bar{\bar{\mathbf{Z}}}_0^{\bullet}$ as $\Delta t \to \infty$. Since the symmetric multiplication by the star-star diagonal matrix $\left(\sqrt{\bar{\bar{\mathbf{D}}}^{\Sigma^S\Sigma^S}}\right)^{-1}$ does not perturb the spectrum of $\bar{\bar{\mathbf{Z}}}_0^{\Sigma^S\Sigma^S}$, this matrix will have the same spectral behavior than that of $\left(\sqrt{\bar{\bar{\mathbf{D}}}^{\Sigma^S\Sigma^S}}\right)^{-1} \bar{\bar{\mathbf{Z}}}_0^{\Sigma^S\Sigma^S} \left(\sqrt{\bar{\bar{\mathbf{D}}}^{\Sigma^S\Sigma^S}}\right)^{-1}$. That said, the spectrum of $\bar{\bar{\mathbf{Z}}}_0^{\Sigma^S\Sigma^S}$ is more easily analyzed. Indeed a closer look at (5.19) shows that as $\Delta t \to \infty$

$$\left(\bar{\bar{\mathbf{Z}}}_0^{\Sigma^S\Sigma^S}\right)_{m,n} = -\left\langle \nabla \cdot \boldsymbol{\Sigma}_m^S(\boldsymbol{r}), \int_\Gamma \frac{T(-|\boldsymbol{r}-\boldsymbol{r}'|/c)}{4\pi\epsilon\,|\boldsymbol{r}-\boldsymbol{r}'|} \nabla \cdot \boldsymbol{\Sigma}_n^S(\boldsymbol{r}')\,\mathrm{d}\boldsymbol{r}' \right\rangle + O\left(\frac{1}{\Delta t^2}\right). \tag{5.37}$$

Hence $\bar{\bar{\mathbf{Z}}}_0^{\Sigma^S\Sigma^S}$ can be thought of as an interaction matrix resulting from discretizing a single layer potential with a weakly singular non-oscillating kernel $\frac{T(-|\boldsymbol{r}-\boldsymbol{r}'|/c)}{4\pi\epsilon|\boldsymbol{r}-\boldsymbol{r}'|}$ using the scalar basis $\nabla\cdot\boldsymbol{\Sigma}^S(\boldsymbol{r})$. The spectral properties of this weakly singular single layer potential result in the ill-conditioning of $\bar{\bar{\mathbf{Z}}}^{\Sigma^S\Sigma^S}$ [36]. This ill-conditioning carries over to $\bar{\bar{\mathbf{Z}}}_0^{\bullet}$.

To remedy this situation, note that the arguments leading to (5.36) do not rely on the fact that star basis functions have been used as nonsolenoidal basis $\boldsymbol{\Sigma}$. In other words, provided that the solenoidal basis $\boldsymbol{\Lambda}$ is used in the (weighted) change of basis matrix $\bar{\bar{\mathbf{P}}}$, the condition number of $\bar{\bar{\mathbf{Z}}}_0^{\bullet}$ will be asymptotically constant as $\Delta t\to\infty$. The value of this constant, however, will be dependent on the choice of the nonsolenoidal basis $\boldsymbol{\Sigma}$. Also note that hierarchical bases are well-known to regularize integral operators with non-oscillating kernels [17]. A second attempt at mitigating time domain low-frequency breakdown therefore is to choose $\bar{\bar{\mathbf{P}}}$ as in (5.27), but with the transformation matrix $\bar{\bar{\mathbf{T}}}$ (and the diagonal preconditioner) constructed using a nonsolenoidal hierarchical basis $\boldsymbol{\Sigma}^H$. This hierarchical basis will be described below. The charge functions $\nabla\cdot\boldsymbol{\Sigma}^H$ will represent a (scalar) hierarchical basis, capable of regularizing $\bar{\bar{\mathbf{Z}}}^{\Sigma^H\Sigma^H}$. Use of this basis will significantly reduce the constant but high condition number obtained when using the standard loop-star basis.

The construction of the basis follows a three step procedure comprising the creation of a hierarchy of meshes, the definition of generalized RWG functions on them, and the construction of the nonsolenoidal basis functions.

5.3.1 Hierarchy of Meshes

A hierarchy of meshes is obtained by recursively grouping cells of the *original* level-0 mesh that approximates Γ (Fig. 5.1). The grouping is performed in such a way that the "macro-cells" comprising the level-l mesh occupy roughly four times

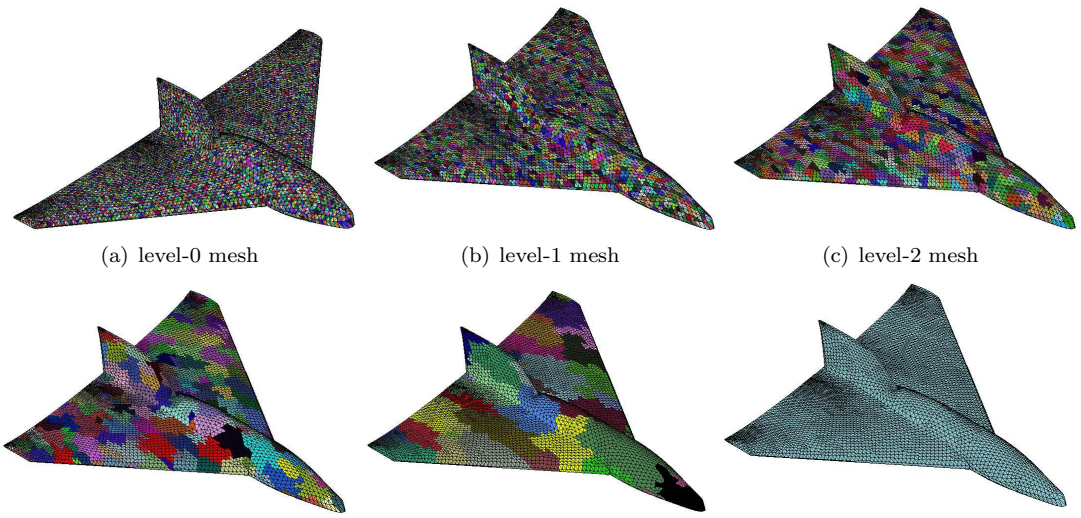

(a) level-0 mesh (b) level-1 mesh (c) level-2 mesh

(d) level-3 mesh (e) level-4 mesh (f) level-5 mesh (comprising only one cell)

Figure 5.1: Example of the grouping procedure: the cells are subsequently grouped to obtain a hierarchy of meshes. In this example the maximum level l_{max} is equal to 5.

the area of level-$(l-1)$ (macro-)cells.

The grouping stops at level l_{max} when a single cell comprising the entire structure is obtained. In practice, the grouping of cells can be achieved in several ways; the procedure used here relies on an oct-tree-based aggregation of cells in the level-0 mesh [11].

5.3.2 Generalized RWGs

Given two adjacent cells, c_1 and c_2 of a level-l mesh with $l \neq 0, l \neq l_{max}$, a "generalized RWG" connecting c_1 and c_2 is defined as a function $\boldsymbol{f}(\boldsymbol{r})$ for which $\nabla_s \cdot \boldsymbol{f}(\boldsymbol{r})$ equals 1 on c_1 and -1 on c_2. To recursively express the level l generalized RWG function $\boldsymbol{f}(\boldsymbol{r})$ as a linear combination of standard RWG functions defined on the level-0 mesh consider the cells of the level-$(l-1)$ mesh that are subcells of c_1 and c_2 (Fig. 5.2(b)). Assume that the level-$(l-1)$ generalized RWGs $\boldsymbol{f}_i(\boldsymbol{r})$, $i = 1, 2, \ldots$, defined between adjacent subcells already have been expressed as linear combinations of standard RWG functions on the level-0 mesh. The function $\boldsymbol{f}(\boldsymbol{r})$ is expressed as

a linear combination of the functions $\boldsymbol{f}_i(\boldsymbol{r})$ as

$$\boldsymbol{f}(\boldsymbol{r}) = \sum_i \alpha_i \boldsymbol{f}_i(\boldsymbol{r}). \tag{5.38}$$

Since the $\boldsymbol{f}_i(\boldsymbol{r})$ are linear combinations of standard RWGs, so will be $\boldsymbol{f}(\boldsymbol{r})$. The coefficients α_i in (5.38) can be obtained by enforcing the condition

$$\sum_i \alpha_i \nabla_s \cdot \boldsymbol{f}_i(\boldsymbol{r}) = \nabla_s \cdot \boldsymbol{f}(\boldsymbol{r}) = \begin{cases} 1 & \boldsymbol{r} \in c_1 \\ -1 & \boldsymbol{r} \in c_2 \end{cases}. \tag{5.39}$$

on each cell of level-$(l-1)$ mesh and inverting the linear system obtained in this way in the least square sense [26].

As an example, consider the two level-2 cells c_1 and c_2 depicted in Fig. 5.2(a). Twelve generalized RWGs $\boldsymbol{f}_i(\boldsymbol{r})$ can be defined on their seven subcells (identified with capital letters A through H) (Fig. 5.2(b)). The linear system to be inverted to obtain these coefficients is

$$\begin{cases} \nabla \cdot \boldsymbol{f}_1(\boldsymbol{r})\alpha_1 + \nabla \cdot \boldsymbol{f}_3(\boldsymbol{r})\alpha_3 + \nabla \cdot \boldsymbol{f}_7(\boldsymbol{r})\alpha_7 = 1 \quad \text{on A} \\ \nabla \cdot \boldsymbol{f}_1(\boldsymbol{r})\alpha_2 + \nabla \cdot \boldsymbol{f}_2(\boldsymbol{r})\alpha_2 = 1 \quad \text{on B} \\ \nabla \cdot \boldsymbol{f}_2(\boldsymbol{r})\alpha_2 + \nabla \cdot \boldsymbol{f}_3(\boldsymbol{r})\alpha_3 + \nabla \cdot \boldsymbol{f}_4(\boldsymbol{r})\alpha_4 + \nabla \cdot \boldsymbol{f}_5(\boldsymbol{r})\alpha_5 = 1 \quad \text{on C} \\ \nabla \cdot \boldsymbol{f}_4(\boldsymbol{r})\alpha_4 = 1 \quad \text{on D} \\ \nabla \cdot \boldsymbol{f}_8(\boldsymbol{r})\alpha_8 + \nabla \cdot \boldsymbol{f}_9(\boldsymbol{r})\alpha_9 = -1 \quad \text{on E} \\ \nabla \cdot \boldsymbol{f}_6(\boldsymbol{r})\alpha_6 + \nabla \cdot \boldsymbol{f}_7(\boldsymbol{r})\alpha_7 + \nabla \cdot \boldsymbol{f}_9(\boldsymbol{r})\alpha_9 + \\ \quad + \nabla \cdot \boldsymbol{f}_{10}(\boldsymbol{r})\alpha_{10} + \nabla \cdot \boldsymbol{f}_{11}(\boldsymbol{r})\alpha_{11} = -1 \quad \text{on F} \\ \nabla \cdot \boldsymbol{f}_{10}(\boldsymbol{r})\alpha_{10} + \nabla \cdot \boldsymbol{f}_{12}(\boldsymbol{r})\alpha_{12} = -1 \quad \text{on G} \\ \nabla \cdot \boldsymbol{f}_3(\boldsymbol{r})\alpha_3 + \nabla \cdot \boldsymbol{f}_{11}(\boldsymbol{r})\alpha_{11} + \nabla \cdot \boldsymbol{f}_{12}(\boldsymbol{r})\alpha_{12} = -1 \quad \text{on H} \end{cases}.$$

Since the functions $\boldsymbol{f}_i(\boldsymbol{r})$ are assumed to be generalized RWGs – $\nabla_s \cdot \boldsymbol{f}_i(\boldsymbol{r}) = \pm 1$ on

each participating subcell with random polarity– (5.40) can be rewritten as

$$\begin{pmatrix} 1 & 0 & 1 & 0 & 0 & 0 & 1 & 1 & 0 & 0 & 0 & 0 \\ -1 & 1 & 0 & 0 & 0 & 0 & 0 & 0 & 0 & 0 & 0 & 0 \\ 0 & -1 & -1 & 1 & 1 & 1 & 0 & 0 & 0 & 0 & 0 & 0 \\ 0 & 0 & 0 & -1 & 0 & 0 & 0 & 0 & 0 & 0 & 0 & 0 \\ 0 & 0 & 0 & 0 & 0 & 0 & 0 & -1 & 1 & 0 & 0 & 0 \\ 0 & 0 & 0 & 0 & 0 & -1 & -1 & 0 & -1 & 1 & 1 & 0 \\ 0 & 0 & 0 & 0 & 0 & 0 & 0 & 0 & 0 & -1 & 0 & 1 \\ 0 & 0 & 0 & 0 & -1 & 0 & 0 & 0 & 0 & 0 & -1 & -1 \end{pmatrix} \begin{pmatrix} \alpha_1 \\ \alpha_2 \\ \alpha_3 \\ \alpha_4 \\ \alpha_5 \\ \alpha_6 \\ \alpha_7 \\ \alpha_8 \\ \alpha_9 \\ \alpha_{10} \\ \alpha_{11} \\ \alpha_{12} \end{pmatrix} = \begin{pmatrix} 1 \\ 1 \\ 1 \\ 1 \\ -1 \\ -1 \\ -1 \\ -1 \end{pmatrix}. \tag{5.40}$$

The least-square inversion of the rectangular matrix in the LHS of (5.40) yields the desired coefficients α_i. To express $\boldsymbol{f}(\boldsymbol{r})$ as a linear combination of RWG functions on the level-0 mesh, the same procedure has to be applied recursively to each $\boldsymbol{f}_i(\boldsymbol{r})$, $i = 1, \ldots, 12$. From the first column of the matrix in (5.40) it is clear that $\nabla \cdot \boldsymbol{f}_1(\boldsymbol{r})$ has been assumed 1 on A and -1 on B. This condition is enforced in the subcells of A and B. Twelve functions $\boldsymbol{f}_p(\boldsymbol{r})$, $p = \mathrm{I}, \ldots, \mathrm{XII}$ can be defined between these two cells (Fig. 5.2(c)); therefore

$$\left\{ \begin{array}{rcll} \nabla \cdot \boldsymbol{f}_I(\boldsymbol{r})\beta_I & = & 1 \quad \text{on a} & \\ \nabla \cdot \boldsymbol{f}_I(\boldsymbol{r})\beta_I + \nabla \cdot \boldsymbol{f}_{II}(\boldsymbol{r})\beta_{II} + \nabla \cdot \boldsymbol{f}_{III}(\boldsymbol{r})\beta_{III} & = & 1 \quad \text{on b} & \\ \nabla \cdot \boldsymbol{f}_{III}(\boldsymbol{r})\beta_{III} + \nabla \cdot \boldsymbol{f}_{IV}(\boldsymbol{r})\beta_{IV} & = & 1 \quad \text{on c} & A \\ \nabla \cdot \boldsymbol{f}_{II}(\boldsymbol{r})\beta_{II} + \nabla \cdot \boldsymbol{f}_{IV}(\boldsymbol{r})\beta_{IV} & = & 1 \quad \text{on d} & \\ \nabla \cdot \boldsymbol{f}_{IV}(\boldsymbol{r})\beta_{IV} + \nabla \cdot \boldsymbol{f}_{V}(\boldsymbol{r})\beta_{V} & = & 1 \quad \text{on e} & \\ \nabla \cdot \boldsymbol{f}_V(\boldsymbol{r})\beta_V + \nabla \cdot \boldsymbol{f}_{XI}(\boldsymbol{r})\beta_{XI} + \nabla \cdot \boldsymbol{f}_{XII}(\boldsymbol{r})\beta_{XII} & = & -1 \quad \text{on f} & \\ \nabla \cdot \boldsymbol{f}_X(\boldsymbol{r})\beta_X + \nabla \cdot \boldsymbol{f}_{XI}(\boldsymbol{r})\beta_{XI} & = & -1 \quad \text{on g} & \\ \nabla \cdot \boldsymbol{f}_{IX}(\boldsymbol{r})\beta_{IX} + \nabla \cdot \boldsymbol{f}_{X}(\boldsymbol{r})\beta_{X} & = & -1 \quad \text{on h} & B \\ \nabla \cdot \boldsymbol{f}_{VIII}(\boldsymbol{r})\beta_{VIII} + \nabla \cdot \boldsymbol{f}_{IX}(\boldsymbol{r})\beta_{IX} & = & -1 \quad \text{on i} & \\ \nabla \cdot \boldsymbol{f}_{VII}(\boldsymbol{r})\beta_{VII} + \nabla \cdot \boldsymbol{f}_{VIII}(\boldsymbol{r})\beta_{VIII} & = & -1 \quad \text{on l} & \\ \nabla \cdot \boldsymbol{f}_{VI}(\boldsymbol{r})\beta_{VI} + \nabla \cdot \boldsymbol{f}_{VII}(\boldsymbol{r})\beta_{VII} & = & -1 \quad \text{on m} & \end{array} \right. . \tag{5.41}$$

The conditions in (5.41) corresponds to the linear system

$$\begin{pmatrix} 1 & 0 & 0 & 0 & 0 & 0 & 0 & 0 & 0 & 0 & 0 & 0 \\ -1 & 1 & 1 & 0 & 0 & 0 & 0 & 0 & 0 & 0 & 0 & 0 \\ 0 & 0 & -1 & 0 & 0 & 1 & 0 & 0 & 0 & 0 & 0 & 0 \\ 0 & -1 & 0 & 1 & 0 & 0 & 0 & 0 & 0 & 0 & 0 & 0 \\ 0 & 0 & 0 & -1 & 1 & 0 & 0 & 0 & 0 & 0 & 0 & 0 \\ 0 & 0 & 0 & 0 & -1 & 0 & 0 & 0 & 0 & 0 & 1 & 1 \\ 0 & 0 & 0 & 0 & 0 & 0 & 0 & 0 & 0 & -1 & -1 & 0 \\ 0 & 0 & 0 & 0 & 0 & 0 & 0 & 0 & -1 & 1 & 0 & 0 \\ 0 & 0 & 0 & 0 & 0 & 0 & 0 & 1 & 1 & 0 & 0 & 0 \\ 0 & 0 & 0 & 0 & 0 & 0 & 1 & -1 & 0 & 0 & 0 & 0 \\ 0 & 0 & 0 & 0 & 0 & -1 & -1 & 0 & 0 & 0 & 0 & -1 \end{pmatrix} \begin{pmatrix} \beta_1 \\ \beta_2 \\ \beta_3 \\ \beta_4 \\ \beta_5 \\ \beta_6 \\ \beta_7 \\ \beta_8 \\ \beta_9 \\ \beta_{10} \\ \beta_{11} \\ \beta_{12} \end{pmatrix} = \begin{pmatrix} 1 \\ 1 \\ 1 \\ 1 \\ 1 \\ -1 \\ -1 \\ -1 \\ -1 \\ -1 \\ -1 \end{pmatrix}. \tag{5.42}$$

that can be inverted in the least square sense to obtain the coefficients βs. Note that since the subcells a,b, . . . ,m belong to the level-0 mesh, the functions $\boldsymbol{f}_I(\boldsymbol{r}), \ldots, \boldsymbol{f}_{XII}(\boldsymbol{r})$ are standard RWG functions. In other words, the function $\boldsymbol{f}_1(\boldsymbol{r})$ is expressed in terms of standard RWGs via the coefficients βs. In a similar way the standard RWG coefficients for the functions $\boldsymbol{f}_i(\boldsymbol{r})$, $i = 2, \ldots, 12$ are obtained. The recursive process stops since the level-0 mesh has been reached. The standard RWG coefficients of the function $\boldsymbol{f}(\boldsymbol{r})$ in terms of the standard RWG basis can now be explicitly obtained from expansion (5.38).

5.3.3 Construction of the Set of Hierarchical Nonsolenoidal Basis Functions $\{\boldsymbol{\Sigma}_p^H\}$

The proposed set of hierarchical nonsolenoidal basis functions is constructed by repeating the following procedure for all cells c at levels $0 < l < l_{max}$:

(i) Consider the generalized RWGs defined between cells of level-$(l-1)$ mesh included in c; let N_f denote their number (Fig.5.3(b)). Define the charge overlap matrix $\bar{\bar{\mathbf{C}}}$ as

$$\left(\bar{\bar{\mathbf{C}}}\right)_{i,j} = \left\langle \nabla_s \cdot \boldsymbol{f}_i(\boldsymbol{r}), \nabla_s \cdot \boldsymbol{f}_j(\boldsymbol{r}) \right\rangle \quad i, j = 1, \ldots, N_f. \tag{5.43}$$

(ii) Next, compute the singular value decomposition [26] of $\bar{\bar{\mathbf{C}}}$

$$\bar{\bar{\mathbf{C}}} = \bar{\bar{\mathbf{V}}}^T \bar{\bar{\mathbf{S}}} \bar{\bar{\mathbf{V}}}. \tag{5.44}$$

(iii) Let $\bar{\bar{\mathbf{V}}}'$ be the matrix containing the columns of $\bar{\bar{\mathbf{V}}}$ corresponding to non zero singular values in $\bar{\bar{\mathbf{S}}}$. The matrix $\bar{\bar{\mathbf{V}}}'$ implements a change of basis from the functions

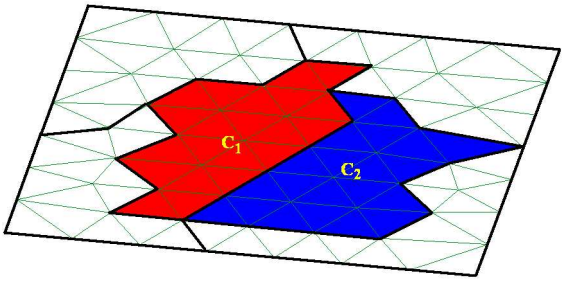

(a) Cells c_1 and c_2 of level $l = 2$

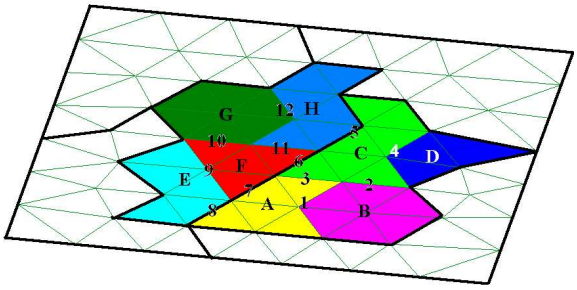

(b) Cells of level $l = 1$ and functions in the cells c_1 and c_2

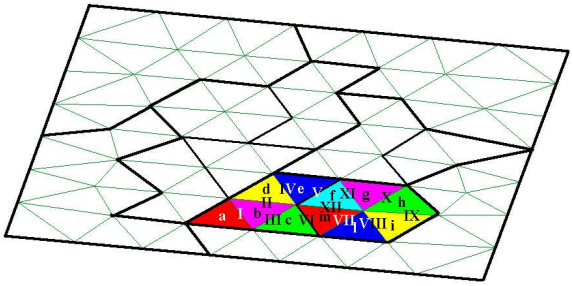

(c) Cells of level $l = 0$ and functions in the cells A and B

Figure 5.2: Cells and functions used in the recursive definition of the generalized RWG $\boldsymbol{f}(\boldsymbol{r})$ defined between the cells c_1 and c_2

$\boldsymbol{f}_i(\boldsymbol{r})$ to new functions $\boldsymbol{\Sigma}_i^H(\boldsymbol{r})$ defined as

$$\boldsymbol{\Sigma}_i^H(\boldsymbol{r}) = \sum_{j=1}^{N_f} \left(\bar{\bar{\mathbf{V}}}'\right)_{i,j} \boldsymbol{f}_j(\boldsymbol{r}). \tag{5.45}$$

The charge overlap matrix $\bar{\bar{\mathbf{C}}}^H$ in this new basis is diagonal:

$$\left(\bar{\bar{\mathbf{C}}}^H\right)_{i,j} = \left\langle \nabla_s \cdot \boldsymbol{\Sigma}_i^H, \nabla_s \cdot \boldsymbol{\Sigma}_j^H \right\rangle = \left(\bar{\bar{\mathbf{S}}}\right)_{i,j}. \tag{5.46}$$

All functions $\boldsymbol{\Sigma}_i^H(\boldsymbol{r})$ obtained in this way are added to $\boldsymbol{\Sigma}^H$. In the example of Fig.5.3, the matrix $\bar{\bar{\mathbf{C}}}$ is

$$\bar{\bar{\mathbf{C}}} = \begin{pmatrix} 2 & 1 & 1 & 0 \\ 1 & 2 & 1 & -1 \\ 1 & 1 & 2 & 1 \\ 0 & -1 & 1 & 2 \end{pmatrix} = \bar{\bar{\mathbf{V}}}^T \begin{pmatrix} 4 & 0 & 0 & 0 \\ 0 & 3 & 0 & 0 \\ 0 & 0 & 1 & 0 \\ 0 & 0 & 0 & 0 \end{pmatrix} \bar{\bar{\mathbf{V}}} \tag{5.47}$$

with

$$\bar{\bar{\mathbf{V}}} = \begin{pmatrix} -0.5774 & 0.0000 & 0.8165 & -0.0000 \\ -0.5774 & 0.4082 & -0.4082 & 0.5774 \\ -0.5774 & -0.4082 & -0.4082 & -0.5774 \\ 0.0000 & -0.8165 & 0.0000 & 0.5774 \end{pmatrix}, \tag{5.48}$$

and

$$\bar{\bar{\mathbf{V}}}' = \begin{pmatrix} -0.5774 & 0.0000 & 0.8165 \\ -0.5774 & 0.4082 & -0.4082 \\ -0.5774 & -0.4082 & -0.4082 \\ 0.0000 & -0.8165 & 0.0000 \end{pmatrix}. \tag{5.49}$$

The functions $\boldsymbol{\Sigma}_i^H(\boldsymbol{r})$ are

$$\boldsymbol{\Sigma}_1^H(\boldsymbol{r}) = -0.5774\boldsymbol{f}_1(\boldsymbol{r}) - 0.5774\boldsymbol{f}_2(\boldsymbol{r}) - 0.5774\boldsymbol{f}_3(\boldsymbol{r}) \tag{5.50}$$

$$\boldsymbol{\Sigma}_2^H(\boldsymbol{r}) = 0.4082\boldsymbol{f}_2(\boldsymbol{r}) - 0.4082\boldsymbol{f}_3(\boldsymbol{r}) - 0.8165\boldsymbol{f}_4(\boldsymbol{r}) \tag{5.51}$$

$$\boldsymbol{\Sigma}_3^H(\boldsymbol{r}) = 0.8165\boldsymbol{f}_1(\boldsymbol{r}) - 0.4082\boldsymbol{f}_2(\boldsymbol{r}) - 0.4082\boldsymbol{f}_3(\boldsymbol{r}). \tag{5.52}$$

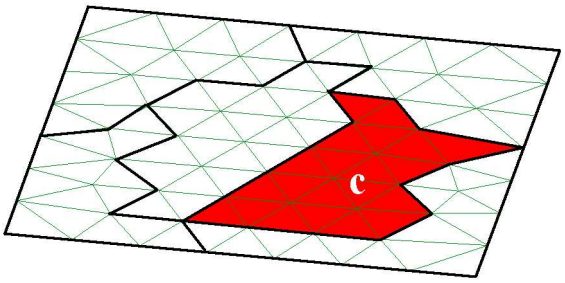

(a) Cell c of level $l = 2$

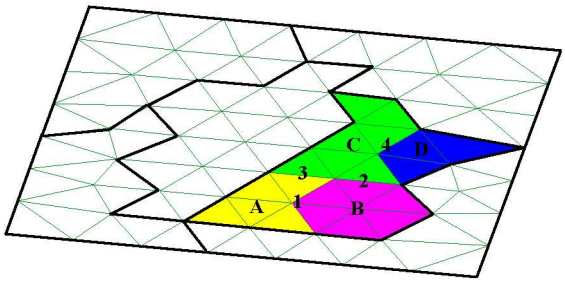

(b) Subcells of c at level $l = 1$ and generalized RWG functions 1 through 4 contained in cell c

Figure 5.3: Cells and functions used in the recursive definition of the hierarchical nonsolenoidal functions $\mathbf{\Sigma}_i^H(\boldsymbol{r})$ in the cell c

Note that these functions are nonsolenoidal by definition, since they correspond to non-null singular values of the overlap charge matrix. The set $\mathbf{\Sigma}^H$ constructed using the above procedure complements $\mathbf{\Lambda}$ since, by construction, all functions in $\mathbf{\Sigma}^H$ are linearly independent and their charge spans that of the level-0 RWG functions. Since the functions $\mathbf{\Sigma}_i^H$ are defined on cells of all levels $l = 1, \ldots, l_{max}$, they represent a hierarchical basis suitable for regularizing the MOT system matrix.

5.3.4 Computational Cost

In this subsection it is shown that the hierarchical basis can be obtained in $O(N_s \log N_s)$ operations. It is sufficient to estimate the total number of coefficients in the transformation matrix $\bar{\bar{\mathbf{P}}}$; the cost of obtaining the coefficients has the same asymptotic dependence on N_s.

For every level l, denote with $N_c(l)$ and $N_e(l)$ the number of cells and (generalized) RWG functions, respectively; $N_e(l_{max}) = 0$ and $N_e(0) = N_s$. To simplify the analysis

assume that the total number of cells of the initial mesh $N_c(0)$ is a multiple of four; then $N_c(l)$ and $N_e(l)$ can be estimated as

$$N_c(l) = 2^{2(l_{max}-l)} \tag{5.53}$$

and

$$N_e(l) = 4N_c(l+1) + 2N_e(l+1) = 4\left(2^{2(l_{max}-l)}\right) + 2N_e(l+1). \tag{5.54}$$

The difference equation (5.54) can be solved in $N_e(l)$ by enforcing the boundary condition $N_e(l_{max}) = 0$, obtaining

$$N_e(l) = 8\left(2^{2(l_{max}-l)} - 2^{(l_{max}-l)}\right). \tag{5.55}$$

Moreover from the condition $N_e(0) = N_s$ it follows that

$$l_{max} = \log_2\left(1 - \sqrt{\frac{N_s}{2} + 1}\right) - 1. \tag{5.56}$$

Therefore the total number of coefficients in $\bar{\bar{\mathbf{P}}}$ is

$$\begin{aligned} N_{coeff}^{\bar{\bar{\mathbf{P}}}} &= \sum_{l=0}^{l_{max}} N_e(l) \cdot N_e(l_{max}-l) = \sum_{l=0}^{l_{max}} \left(8\left(2^{2(l_{max}-l)} - 2^{(l_{max}-l)}\right)\right) \cdot \left(8\left(2^{2(l)} - 2^{(l)}\right)\right) \\ &= 64\left(3 + 2^{l_{max}}\left(l_{max} - 3\right) + l_{max}\right) 2^{l_{max}}. \end{aligned} \tag{5.57}$$

Substituting (5.56) in (5.57) yields

$$N_{coeff}^{\bar{\bar{\mathbf{P}}}} = 8\left(\left(8 + N_s - 4\sqrt{4 + 2N_s}\right)\left(\log_2\left(2 - \sqrt{4 + 2N_s}\right) - 2\right) - 3N_s\right), \tag{5.58}$$

and therefore

$$N_{coeff}^{\bar{\bar{\mathbf{P}}}} \sim 2^{7.5} N_s \log N_s \quad \text{as } N_s \to \infty, \tag{5.59}$$

which proves the initial statement.

5.3.5 A Note on the Computation of the Diagonal Matrix $\bar{\bar{\mathbf{D}}}$

The computation of the diagonal matrix $\bar{\bar{\mathbf{D}}}$

$$\bar{\bar{\mathbf{D}}} = \begin{pmatrix} \bar{\bar{\mathbf{D}}}^{\Lambda\Lambda} & \\ & \bar{\bar{\mathbf{D}}}^{\Sigma^H\Sigma^H} \end{pmatrix} \tag{5.60}$$

requires some care. The computation of $\bar{\bar{\mathbf{D}}}^{\Lambda\Lambda}$ is not problematic, in fact it can be achieved by extracting the loop-associated part of the diagonal of the matrix $\bar{\bar{\mathbf{T}}}^T\bar{\bar{\mathbf{Z}}}_0\bar{\bar{\mathbf{T}}}$ by performing the matrix-matrix multiplications in a way that accounts for the sparsity pattern of $\bar{\bar{\mathbf{T}}}$. Since the loop-associated columns of the matrix $\bar{\bar{\mathbf{T}}}$ contain only a constant number of nonzero elements, $\bar{\bar{\mathbf{D}}}^{\Lambda\Lambda}$ can be computed in $O(N_s)$ operations. As regards the cost of the computation of $\bar{\bar{\mathbf{D}}}^{\Sigma^H\Sigma^H}$, extracting the hierarchical basis-associated part of the diagonal of the matrix product $\bar{\bar{\mathbf{T}}}^T\bar{\bar{\mathbf{Z}}}_0\bar{\bar{\mathbf{T}}}$ by performing the matrix-matrix product would cost less than $O(32\cdot 2^{l_{max}}(3+l_{max})(3-32^{l_{max}})+l_{max}+2^{l_{max}}l_{max})) = O(N_s\log^2 N_s)$ operations. This assumes that a fast, "$N\log N$", matrix multiplication algorithm is used to multiply matrix elements of $\bar{\bar{\mathbf{Z}}}_0$. In practice the matrix-matrix product is not necessary, since only the magnitude of $\bar{\bar{\mathbf{D}}}^{\Sigma^H\Sigma^H}$ is of interest when preconditioning diagonally, and it can be estimated by extracting the hierarchical basis-associated part of $\bar{\bar{\mathbf{T}}}^T\bar{\bar{\mathbf{Z}}}_0^{near}\bar{\bar{\mathbf{T}}}$ [50], where $\bar{\bar{\mathbf{Z}}}_0^{near}$ is the near field part of the impedance matrix. In this way the computational cost is reduced to $O(N_s\log N_s)$. This is the solution adopted in the experiments described below.

5.4 Numerical Results

This section presents several examples that demonstrate the effectiveness of the hierarchical basis and its applicability to complex problems. Section 5.4.1 demonstrates the benefits of the proposed hierarchical regularization scheme through the analysis of scattering from a sphere. Sections 5.4.2 and 5.4.3 show the applicabil-

ity of the proposed scheme to more complicated and realistic problems through the scattering analysis of a delta wing and a ship, respectively.

The results presented here are obtained using a parallel time-domain adaptive-integral method (TD-AIM) accelerated TD-EFIE solver [55], which uses a transpose-free quasi-minimal residual (TFQMR)-based iterative solver [25] at every time step to solve the MOT system. The MOT systems are constructed using the hierarchical basis, the loop-star basis, or the standard RWG basis to allow for the comparison of these bases' convergence properties. In all simulations the excitation is a plane-wave propagating in the $\hat{\boldsymbol{k}}$ direction with a $\hat{\boldsymbol{p}}$ polarized electric field $\boldsymbol{E}^i(\boldsymbol{r},t) = \hat{\boldsymbol{p}}E_0G(t-\boldsymbol{r}\cdot\hat{\boldsymbol{k}}/c)$, where $G(t) = e^{-(t-t_p)^2/2\sigma^2}$ is a baseband Gaussian with duration $\sigma = 4/(\pi f_{max})$, and delay $t_p = 8\sigma$; with this choice of parameters, 99.98% of the power of $G(t)$ is within the frequency band $[-f_{max}, f_{max}]$. The time step depends only on f_{max} and is determined using (5.7) with $\alpha = 10$. All simulations were carried out on a cluster of dual-core 2.8-GHz AMD Opteron 2220 SE processors located at the Center for Advanced Computing at the University of Michigan.

5.4.1 Sphere

In this section, the effectiveness of the proposed scheme is demonstrated through the analysis of scattering from a sphere of radius $R = 1\,\mathrm{m}$ that is centered at the origin and excited by a plane wave with $\hat{\boldsymbol{k}} = -\hat{\boldsymbol{y}}$, $\hat{\boldsymbol{p}} = \hat{\boldsymbol{x}}$, and $E_0 = 1\,\mathrm{V/m}$. To construct the hierarchical basis, the procedure described in Section 5.3 is iterated seven times, resulting in a eight-level hierarchy. At level 0, $N_s = 22065$ basis functions are used; the maximum, minimum, and average RWG edge sizes are 9.26 cm, 1.94 cm, and 4.48 cm, respectively. A series of simulations is performed changing f_{max} from 37.5 MHz ($\Delta t = 2.67\,\mathrm{ns}$) to 31.25 KHz ($\Delta t = 3.2\,\mu\mathrm{s}$). Fig. 5.4(a) presents, for each value of $1/\Delta t$, the number of iterations required for the relative residual error of the

solutions of the MOT systems constructed using the hierarchical, loop-star, standard RWG, and the diagonally preconditioned RWG bases to reach 10^{-8}. Since these iteration counts are good indicators of the condition number, it is concluded that, when $\Delta t \to \infty$ ($f_{max} \to 0$), the matrices constructed using RWG and diagonally preconditioned RWGs become increasingly ill-conditioned, while the condition number of the matrix constructed using the loop-star basis reaches a constant but high value. The constant condition number of the matrix constructed using the hierarchical basis is noticeably lower than that of the one constructed using the loop-star basis. To demonstrate the accuracy of the proposed method, coefficients of the RWG basis function centered at $x = 0\,\mathrm{m}$, $y = 0.99985\,\mathrm{m}$, and $z = 0.012665$ obtained (during the simulation with $f_{max} = 9.375\,\mathrm{MHz}$) using the hierarchical basis and the diagonally preconditioned RWG basis are compared for all times in Fig. 5.4(b). The agreement in the current density (coefficient of the RWG basis function) shows that both schemes practically produce the same result.

5.4.2 Delta Wing

In this section the applicability of the proposed scheme to realistic structures is demonstrated through the analysis of scattering from a (UAV) delta wing (Fig. 5.5(a)). The delta wing is excited by a plane wave with $\hat{\boldsymbol{k}} = -\hat{\boldsymbol{y}}$, $\hat{\boldsymbol{p}} = \hat{\boldsymbol{z}}$, and $E_0 = 1\,\mathrm{V/m}$. To construct the hierarchical basis, the procedure described in Section 5.3 is iterated eight times, resulting in an nine-level hierarchy. At level 0, $N_s = 30309$ basis functions are used; the maximum, minimum, and average RWG edge sizes are 3.94 cm, 0.27 cm, and 1.24 cm respectively. A series of simulations is performed changing f_{max} from 200 MHz ($\Delta t = 0.5\,\mathrm{ns}$) to 97.65625 KHz ($\Delta t = 1.024\,\mu\mathrm{s}$). Fig. 5.5(b) presents, for each value of $1/\Delta t$, the number of iterations required for the relative residual error of the solutions of the MOT systems constructed using the hierarchi-

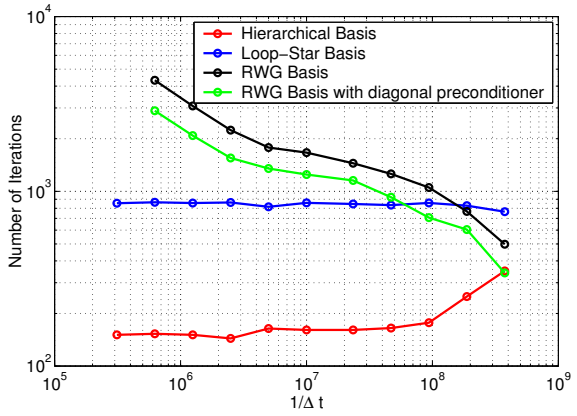

(a)

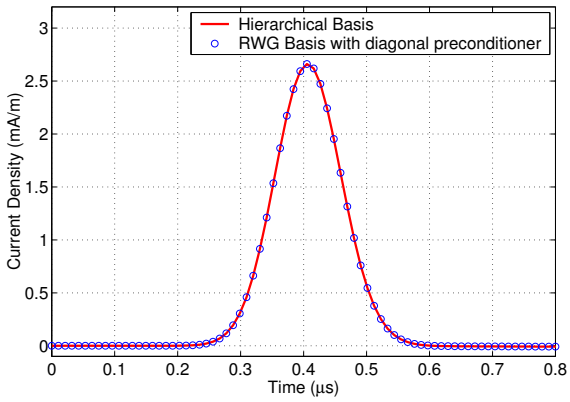

(b)

Figure 5.4: Analysis of scattering from a sphere. (a) Number of iterations for solving the MOT systems constructed using different bases and different values of Δt. (b) Current density at a point on the surface of the sphere obtained solving MOT systems constructed using hierarchical basis and RWG basis with diagonal preconditioner.

cal, loop-star, standard RWG, and diagonally preconditioned RWG basis to reach 10^{-8}. To demonstrate the accuracy of the proposed method, coefficients of an RWG basis function located on the nose of the delta wing obtained (during the simulation with $f_{max} = 50\,\text{MHz}$) solving MOT systems constructed using the hierarchical and diagonally preconditioned RWG basis are compared for all times in Fig. 5.5(c). The agreement in the current density (coefficient of the RWG basis function) shows that both schemes practically produce the same result. For completeness, Figs. 5.5(d)-5.5(f) show snapshots of the current density obtained (during the simulation with $f_{max} = 50\,\text{MHz}$) on delta wing's surface at $t = 25\Delta t$, $t = 35\Delta t$, and $t = 50\Delta t$.

5.4.3 Ship

In this section the applicability of proposed scheme to realistic structures is demonstrated through the analysis of scattering from a ship (Fig. 5.6(a)). The ship is excited by a plane wave with $\hat{\boldsymbol{k}} = -\hat{\boldsymbol{x}}$, $\hat{\boldsymbol{p}} = \hat{\boldsymbol{z}}$, and $E_0 = 1\,\text{V/m}$. To construct the hierarchical basis, the procedure described in Section 5.3 is iterated nine times, resulting in a ten-level hierarchy. At level 0, $N_s = 57427$ basis functions are used; the maximum, minimum, and average RWG edge sizes are 2.055 m, 0.0725 m, and 0.355 m respectively. A series of simulations is performed changing f_{max} from 16 MHz ($\Delta t = 6.25\,\text{ns}$) to 7.81 KHz ($\Delta t = 12.79\,\mu\text{s}$). Fig. 5.6(b) presents, for each value of $1/\Delta t$, the number of iterations required for the relative residual error of the solutions of the MOT systems constructed using the hierarchical, loop-star, standard RWG, and diagonally preconditioned RWG basis to reach 10^{-8}. To demonstrate the accuracy of the proposed method, coefficients of an RWG basis function located on the ship's radar obtained (during the simulation with $f_{max} = 2\,\text{MHz}$) solving MOT systems constructed using the hierarchical and diagonally preconditioned RWG basis are compared for all times in Fig. 5.6(c). The agreement in the current density

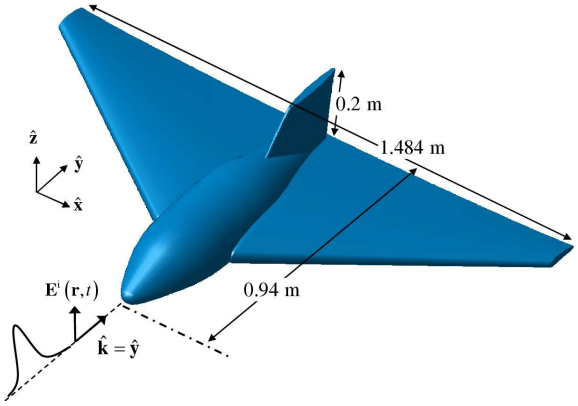

(a)

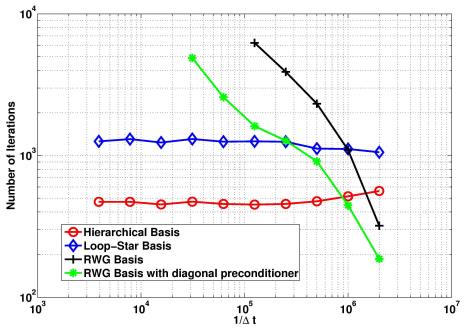

(b)

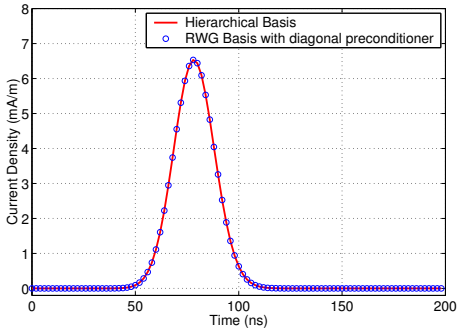

(c)

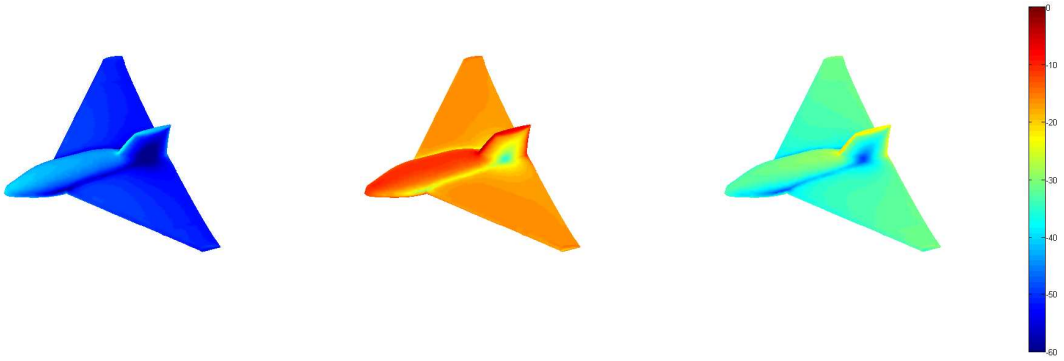

(d) (e) (f)

Figure 5.5: Analysis of scattering from a delta wing. (a) Geometry description and plane-wave excitation. (b) Number of iterations for solving the MOT systems constructed using different bases and different values of Δt. (c) Current density on the nose of the delta wing obtained solving MOT systems constructed using hierarchical basis and RWG basis with diagonal preconditioner. Snapshots of the current density on the surface of the delta wing at (d) $t = 25\Delta t$, (e) $t = 35\Delta t$, and (f) $t = 50\Delta t$ (in dB scale).

(coefficient of the RWG basis function) shows that both schemes practically produce the same result. For completeness, Figs. 5.6(d)- 5.6(f) show snapshots of the current density obtained (during the simulation with $f_{max} = 2\,\mathrm{MHz}$) on ship's surface at $t = 30\Delta t$, $t = 40\Delta t$, and $t = 50\Delta t$.

5.5 The use of the Gerschgorin's disk theorem

Let $\bar{\bar{\mathbf{Z}}} \in \mathbb{C}^{n\times n}$ *be an arbitrary square matrix and* $\bar{\bar{\mathbf{P}}} \in \mathbb{C}^{n\times n}$ *an arbitrary non singular matrix. Let*

$$\bar{\bar{\mathbf{A}}} = \bar{\bar{\mathbf{P}}}^{-1}\bar{\bar{\mathbf{Z}}}\bar{\bar{\mathbf{P}}} \tag{5.61}$$

and

$$a_{ij} = \left(\bar{\bar{\mathbf{A}}}\right)_{i,j}. \tag{5.62}$$

Define the i-th Gershgorin disk

$$D_i = \left\{ x \in \mathbb{C} / \left| x - a_{ii} \right| < \sum_{j=1, j\neq i}^{n} |a_{ij}| \right\} \tag{5.63}$$

then the eigenvalues of $\bar{\bar{\mathbf{Z}}}$ *are contained, in the complex plane, in the union set of the Gershgorin disks* $\bigcup_{i=1}^{n} D_i$*. Moreover if the union set of* m *Gershgorin disks (with* $m < n$*) is disjoint from the union set of the remaining* $m - n$ *Gershgorin disks, then exactly* m *eigenvalues of* $\bar{\bar{\mathbf{Z}}}$ *are contained in the first set and the remaining* $m - n$ *eigenvalues are contained in the other.* A proof of this theorem can be found in [47].

The Gerschgorin's disk theorem can be used to prove (5.21) as follows: define the matrix $\left(\bar{\bar{\mathbf{Z}}}_0^{\Sigma^S\Sigma^S}\right)_{static}$ as the limit as $\Delta t \to \infty$ of the matrix $\bar{\bar{\mathbf{Z}}}_0^{\Sigma^S\Sigma^S}$

$$\left(\bar{\bar{\mathbf{Z}}}_0^{\Sigma^S\Sigma^S}\right)_{static} = \lim_{\Delta t\to\infty} \bar{\bar{\mathbf{Z}}}_0^{\Sigma^S\Sigma^S}. \tag{5.64}$$

Assume that the matrix $\left(\bar{\bar{\mathbf{Z}}}_0^{\Sigma^S\Sigma^S}\right)_{static}$ is diagonalizable, if this assumption does not hold then use of the Jordan canonical forms [47] and minor modifications are necessary to the arguments that follow. Denote with $\bar{\bar{\mathbf{P}}}^{\Sigma^S\Sigma^S}$ the orthogonal matrix that

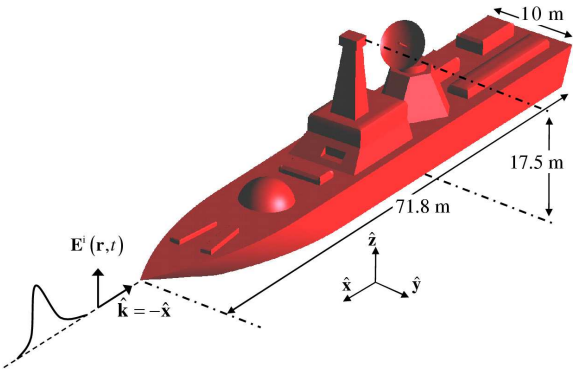

(a)

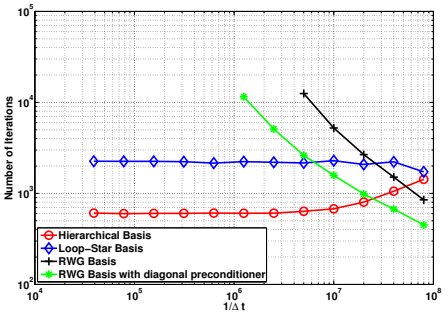

(b)

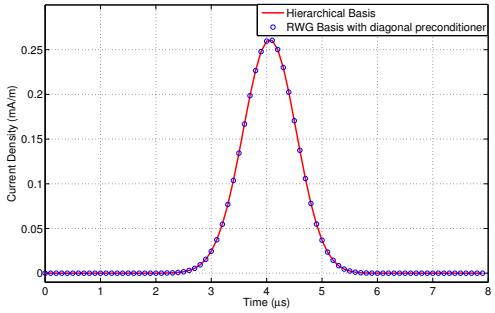

(c)

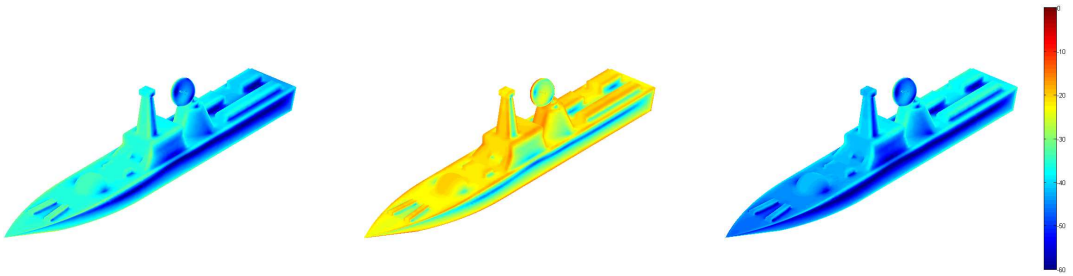

(d) (e) (f)

Figure 5.6: Analysis of scattering from a ship. (a) Geometry description and plane-wave excitation. (b) Number of iterations for solving the MOT systems constructed using different bases and different values of Δt. (c) Current density on the ship's radar obtained solving MOT systems constructed using hierarchical basis and RWG basis with diagonal preconditioner. Snapshots of the current density on the surface of the ship at (d) $t = 30\Delta t$, (e) $t = 40\Delta t$, and (f) $t = 50\Delta t$ (in dB scale).

diagonalizes $\left(\bar{\bar{\mathbf{Z}}}_0^{\Sigma^S\Sigma^S}\right)_{static}$, i.e.

$$\left(\bar{\bar{\mathbf{P}}}^{\Sigma^S\Sigma^S}\right)^{-1}\left(\bar{\bar{\mathbf{Z}}}_0^{\Sigma^S\Sigma^S}\right)_{static}\bar{\bar{\mathbf{P}}}^{\Sigma^S\Sigma^S}=\mathrm{diag}[\lambda_1,\lambda_2,\ldots,\lambda_{N_s-N_l}] \tag{5.65}$$

where $\lambda_i, i=1,\ldots,N_s-N_l$ are the eigenvalues of $\left(\bar{\bar{\mathbf{Z}}}_0^{\Sigma^S\Sigma^S}\right)_{static}$. Define the matrix $\bar{\bar{\mathbf{A}}}$

$$\bar{\bar{\mathbf{A}}} = \begin{pmatrix} \bar{\bar{\mathbf{I}}} & \\ & \left(\bar{\bar{\mathbf{P}}}^{\Sigma^S\Sigma^S}\right)^{-1} \end{pmatrix} \bar{\bar{\mathbf{Z}}}_0^{LS} \begin{pmatrix} \bar{\bar{\mathbf{I}}} & \\ & \left(\bar{\bar{\mathbf{P}}}^{\Sigma^S\Sigma^S}\right) \end{pmatrix} \tag{5.66}$$

$$= \begin{pmatrix} \bar{\bar{\mathbf{Z}}}^{\Lambda\Lambda} & \bar{\bar{\mathbf{Z}}}_0^{\Lambda\Sigma^S}\bar{\bar{\mathbf{P}}}^{\Sigma^S\Sigma^S} \\ \left(\bar{\bar{\mathbf{P}}}^{\Sigma^S\Sigma^S}\right)^{-1}\bar{\bar{\mathbf{Z}}}_0^{\Sigma^S\Lambda} & \mathrm{diag}[\lambda_1,\lambda_2,\ldots,\lambda_{N_s-N_l}] \end{pmatrix}. \tag{5.67}$$

The Gerschgorin's disks associated with the matrix $\bar{\bar{\mathbf{A}}}$ belong to two families. The first family contains the disks associated with the first N_l rows of the matrix $\bar{\bar{\mathbf{A}}}$; these disks' centers and radii are

$$c_i=\left(\bar{\bar{\mathbf{Z}}}^{\Lambda\Lambda}\right)_{ii}=O\left(\frac{1}{\Delta t^2}\right),\Delta t\to\infty \tag{5.68}$$

and

$$r_i=\sum_{j=1,j\neq i}^{n}|(\,\bar{\bar{\mathbf{Z}}}_0^{\Lambda\Sigma^S}\bar{\bar{\mathbf{P}}}^{\Sigma^S\Sigma^S}\,)_{i,j}|=O\left(\frac{1}{\Delta t^2}\right),\Delta t\to\infty \tag{5.69}$$

$i=1,\ldots,N_l$, where (5.16) and (5.17) have been used. In other words the Gerschgorin disks associated with the first N_l rows of the matrix $\bar{\bar{\mathbf{A}}}$ collapse to the origin when $\Delta t\to\infty$.

The second family of disks contains the ones associated with the remaining N_s-N_l rows, these disks have centers

$$c_i=\lambda_i=O(1),\Delta t\to\infty \tag{5.70}$$

and radii

$$r_i=\sum_{j=1,j\neq i}^{n}\left|\left(\bar{\bar{\mathbf{P}}}^{\Sigma^S\Sigma^S}\right)_{i,j}\bar{\bar{\mathbf{Z}}}_0^{\Sigma^S\Lambda}\right|=O\left(\frac{1}{\Delta t^2}\right),\Delta t\to\infty \tag{5.71}$$

$i = N_{l+1}, \ldots, N_s$. In other words this second family of disks collapses to their centers λ_i when $\Delta t \to \infty$. Note that λ_i are Δt independent and different from zero (this since $\left(\bar{\bar{\mathbf{Z}}}_0^{\Sigma^S \Sigma^S}\right)_{static}$ is invertible).

From the considerations above is follows that for $\Delta t \to \infty$ the two families of disks are disjoint. Thus the Gerschgorin's disk theorem ensures that N_l eigenvalues will go to zero as fast as $1/\Delta t^2, \Delta t \to \infty$ and the remaining will converge to Δt-independent values λ_i. This proves equation (5.21).

A similar argument validates equation (5.36).

CHAPTER VI

Conclusions and Future Work

Continuously accelerating technological progress has resulted in a heightened demand for efficient and accurate simulation techniques that permit first-pass design of increasingly complex electronic and electromagnetic systems. Whenever in the past boundary element (or integral equation) methods provided a convincing answer to the many application-inspired problems posed by its practitioners, more and more frequently the techniques described in the archival literature prove to be inadequate to properly address the increased complexity and challenges introduced by modern scientific and engineering problems.

6.1 Summary

This thesis presented numerical techniques capable of efficiently and accurately handling common to severely pathological problems on which standard integral equation techniques for analyzing electromagnetic phenomena fail.

Chapter II presented a multiplicative preconditioner for the frequency domain EFIE leveraging the Calderón identities; the preconditioner ensures fast convergence rates of the associated MoM iterative solver even when applied to dense meshes. The resulting integral equation tool is capable of analyzing geometrically highly detailed structures as well as pathological geometries such as tips and corners that prevent

the application of previously developed techniques. Numerical results have confirmed the effectiveness of the proposed preconditioner and its applicability to the analysis of electromagnetic interactions with complex and realistic structures.

When dealing with closed structures the use of the frequency domain CFIEs often is preferred over that of EFIEs. The problem of preconditioning the CFIE is addressed in Chapter III, where a regularized CFIE has been presented. The regularization is achieved by analytically inverting the CFIE hypersingular part, and this without negative repercussions on computational complexity. Numerical results have been presented that show that the proposed equation is resonant free and immune from the dense-discretization breakdown and related ill-conditioning phenomena.

Novel time domain integral equations to solve stability problems inherent to time domain EFIEs have been presented in Chapter IV. The theoretical arguments proving the effectiveness of the new equations proposed have been shown along with numerical results confirming the equations' theoretically predicted behavior.

The time domain low-frequency breakdown problem has been addressed in Chapter V where a hierarchical basis to discretize the TD-EFIE has been presented. The basis gives rise to a linear system that is immune from time domain low-frequency breakdown even for complex meshes. The basis functions are expressed as linear combinations of standard RWGs, and generated on arbitrary triangular meshes without any restriction. The analysis of the time domain low frequency breakdown phenomena presented in the chapter explained the limited efficacy of the techniques adopted in the literature and justified the use of the proposed approach. Numerical results that show the beneficial impact of the proposed basis on the simulation of realistic structures were presented.

6.2 Future Work

The research presented in this thesis will continue on several fronts. The techniques detailed in Chapter II can be applied to the discretization of 3D combined field integral equations and integrated with the new operatorial identities developed in Chapter III. Moreover many numerical tools can benefit from the use of the Calderón techniques developed in this work. The list includes, but it is not limited to, the majority of boundary element formulations for analyzing scattering from homogeneous dielectric bodies, the regularization of the integral part of boundary/finite elements hybrid solvers, and the smoothing of integral operators arising in inverse scattering theory. Finally the techniques presented here can be extended to include junctions, higher order basis functions, and singular current elements, and can be interfaced with mixed volume/surface integral equation solvers.

6.3 Contributions

This thesis resulted in the following contributions:

Journal Papers

1. F. P. Andriulli and E. Michielssen. A Regularized Combined Field Integral Equation for Scattering from 2D Perfectly Electric Conducting Objects. *IEEE Trans. Antennas Propagation*, 55(9):2522–2529, 2007.

2. F. P. Andriulli, H. Bagci, F. Vipiana, G. Vecchi, and E. Michielssen. A Marching-On-in-Time Hierarchical Scheme for the Time Domain Electric Field Integral Equation. *IEEE Trans. Antennas Propagation*, 55(12):3734–3738, 2007.

3. F. P. Andriulli, K. Cools, H. Bagci, F. Olyslager, A. Buffa, S. Christiansen, and E. Michielssen. A Multiplicative Calderon Preconditioner for the Electric Field Integral Equation. *Accepted for publication to appear on IEEE Trans. on Antennas and Propagat., special issue on Large and Multiscale Computational Electromagnetics* , 2007.

4. F. P. Andriulli, H. Bagci, F. Vipiana, G. Vecchi, and E. Michielssen. Hierarchical Regularization of the Time Domain Electric Field Integral Equation. *Submitted to IEEE Transactions on Antennas and Propagation*, 2007.

5. K. Cools, F. P. Andriulli, F. Olyslager, and E. Michielssen. Time-Domain Calderón Identities and their Application to the Integral Equation Analysis of Scattering by PEC Objects, Part I: Preconditioning. *Submitted to IEEE Transactions on Antennas and Propagation*, 2008.

6. F. P. Andriulli, K. Cools, F. Olyslager, and E. Michielssen. Time-Domain Calderón Identities and their Application to the Integral Equation Analysis of Scattering by PEC Objects, Part II: Stabilization. *Submitted to IEEE Transactions on Antennas and Propagation*, 2008.

Conference Papers

7. F. Andriulli, E. Michielssen, *A $N\log^2(N)$ Factorization for the Plane Wave Scattering Matrix*. Proc. IEEE International Symposium on Antenna and Propagation, pp 4003 – 4006, July 2006

8. F. Andriulli, E. Michielssen, *A well-posed combined field integral equation for scattering from perfect electrically conducting objects*. Proc. IEEE International

Symposium on Antenna and Propagation, June 2007

9. F. Andriulli, H. Bagci, F. Vipiana, G. Vecchi, E. Michielssen, *Hierarchical Discretization of the Time Domain Electric Field Integral Equation*. Proc. IEEE International Symposium on Antenna and Propagation, June 2007

10. K. Cools, F. Andriulli, E. Michielssen, *Calderòn Preconditioned Time Domain Integral Equation Solvers*. Proc. IEEE International Symposium on Antenna and Propagation, June 2007

11. F. Andriulli, K. Cools, E. Michielssen, *Stable Time Domain Integral Equations Based on Calderòn Formulas*. Proc. IEEE International Symposium on Antenna and Propagation, June 2007

12. F. P. Andriulli, H. Bagci, F. Vipiana, G. Vecchi, and E. Michielssen, *A Parallel Hierarchical Solver for the Integral Equation Analysis of Low Frequency Devices*. Proc. IEEE Electrical Performance of Electronic Packaging, 2007

13. F. P. Andriulli, H. Bagci, F. Vipiana, G. Vecchi, and E. Michielssen. A Hierarchical Regularization of the Time Domain Electric Field Integral Equation. *Submitted to IEEE International Symposium on Antenna and Propagation*, 2008.

14. F. P. Andriulli, K. Cools, F. Olyslager, and E. Michielssen. The "dottrick TDEFIE": a DC stable integral equation for analyzing transient scattering from PEC bodies. *Submitted to IEEE International Symposium on Antenna and Propagation*, 2008.

15. F. P. Andriulli, K. Cools, H. Bagci, F. Olyslager, A. Buffa, S. Christiansen, and

E. Michielssen. A Multiplicative Calderón Preconditioner for the Electric Field Integral Equation. *Submitted to IEEE International Symposium on Antenna and Propagation*, 2008.

BIBLIOGRAPHY

BIBLIOGRAPHY

[1] M. Abramowitz and I. Stegun. *Handbook of mathematical functions*. Dover, 1965.

[2] R. J. Adams. Physical and analytical properties of a stabilized electric field integral equation. *IEEE Trans. Antennas Propagation*, 52(2):362–372, February 2004.

[3] F. Andriulli, A. Tabacco, and G.Vecchi. A Multiresolution Approach to the Electric Field Integral Equation in Antenna Problems. *SIAM J. Sci. Comput.*, 29(1):1–21, January 2007.

[4] F. P. Andriulli, H. Bagci, F. Vipiana, G. Vecchi, and E. Michielssen. A Marching-On-in-Time Hierarchical Scheme for the Time Domain Electric Field Integral Equation. *IEEE Trans. Antennas Propagation*, 55(12):3734–3738, 2007.

[5] O. Axelsson. *Iterative Solution Methods*. Cambridge University Press, Cambridge, 1994.

[6] C. Balanis. *Advanced Engineering Electromagnetics*. Wiley and sons, 1989.

[7] C. L. Bennett. *A technique for computing approximate impulse response for conducting bodies*. PhD thesis, Purdue Univ., West Lafayette, 1968.

[8] S. Borel, D. P. Levadoux, and F. Alouges. A new well-conditioned Integral formulation for Maxwell equations in three dimensions. *IEEE Trans. Antennas Propagation*, 53(9):2995–3004, September 2005.

[9] A. Buffa and S. Christiansen. A dual finite element complex on the barycentric refinement. *Comptes rendus. Mathmatique*, 360(6):461–464, 2005.

[10] N. W. Chen, K. Aygun, and E. Michielssen. Integral-equation-based analysis of transient scattering and radiation form conducting bodies at very low frequencies. *IEE Proc.-Microw. Antennas Propag.*, 148(6):381–387, October 2001.

[11] W. C. Chew, J.-M. Jin, E. Michielssen, and J. Song. *Fast and Efficient Alhorithms in Computaional Electrimagnetics*. ARTECH house, 2001.

[12] Snorre H. Christiansen and Jean-Claude Nedelec. A preconditioner for the electric field integral equation based on Calderon formulas. *SIAM journal on numerical analysis*, 40(3):1100–1135, 2003.

[13] R. Coifman, V. Rokhlin, and S. Wandzura. The fast multipole method for the wave equation: A pedestrian prescription. *IEEE Antennas and Propagation Magazine*, pages 7–12, 1993.

[14] D. Colton and R. Kress. *Integral Equation Methods in Scattering Theory*. Wiley, 1983.

[15] H. Contopanagos, B. Dembart, M. Epton, J.J. Ottusch, V. Rokhlin, J.L. Visher, and S. M. Wandzura. Well-Conditioned Boundary Integral Equations for Three-Dimensional Electromagnetic Scattering. *IEEE Trans. Antennas Propagation*, 50(12):1824–1930, December 2002.

[16] K. Cools, F. P. Andriulli, F. Olyslager, and E. Michielssen. Time-Domain Calderón Identities and their Application to the Integral Equation Analysis of Scattering by PEC Objects, Part I: Preconditioning. *Submitted to IEEE Transactions on Antennas and Propagation*, 2007.

[17] W. Dahmen. Wavelet and multiscale methods for operator equations. *Acta Numerica*, pages 55–228, 1997.

[18] S. J. Dodson, S.P. Walker, and M.J. Bluck. Implicitness and stability of time domain integral equation scattering analysis. *Applied Computational Electromagnetics Society Journal*, 13(3):291–301, 1998.

[19] E. Bleszynski and M. Bleszynski and T. Jaroszewicz. AIM: Adaptive integral methods for solving large-scale electrimagnetic scattering and radiation problems. *Radio Sci.*, 31(5):1225–1251, 1996.

[20] T. F. Eibert. Iterative-solver convergence for loop-star and loop-tree decompositions in method-of-moments solutions of the electric-field integral equation. *IEEE Antennas and Propagation Magazine*, 46(3):80–85, June 2004.

[21] A. A. Ergin, B. Shanker, and E. Michielssen. Fast evaluation of three-dimensional transient wave fields using diagonal translation operators. *J. Comp. Phys.*, 146(1):157–180, 1998.

[22] A. A. Ergin, B. Shanker, and E. Michielssen. Analysis of transient wave scattering from rigid bodies using a Burton-Miller approach. *Journal of the Acoustical Society of America*, 106(5):2396–2404, 1999.

[23] A. A. Ergin, B. Shanker, and E. Michielssen. Analysis of transient wave scattering from rigid bodies using a Burton-Muller approach. *J. Acoust. Soc. Am.*, 106:2396–2404, 1999.

[24] A. A. Ergin, B. Shanker, and E. Michielssen. The plane wave time domain algorithm for the fast analysis of transient wave phenomena. *IEEE Antennas and Propagation Magazine*, 41(4):39–52, 1999.

[25] R. W. Freund. A transpose-free quasi-minimal residual algorithm for non-hermitian linear systems. *SIAM J. Sci. Stat. Comput.*, 14(2):470–482, 1993.

[26] G. H. Golub and C. F. van Loan. *Matrix Computation*. Johns Hopkins U.P., Baltimore, 1989.

[27] R. D. Graglia, D. R. Wilton, and A. F. Peterson. Higher order interpolatory vector bases for computational electromagnetics. *IEEE Trans. Antennas Propagation*, 45:329–342, 1997.

[28] R. F. Harrington. *Field Computation by Moment Method*. IEEE press, 1993.

[29] G. C. Hsiao and R. E. Kleinman. Mathematical foundation for error estimation in numerical solution of integral equations in electromagnetics. *IEEE Trans. Antennas Propagation*, 45(3):316–328, March 1997.

[30] S. Lang. *Algebra*. Springer, 2005.

[31] C.-C. Lu and W.C. Chew. A multilevel algorithm for solving a boundary integral equation of wave scattering. *Microwave Opt. Technol. Lett.*, 7(10):466–470, 1994.

[32] J. R. Mautz and R. F. Harrington. H-field, E-field, and combined field solution for conducting bodies of revolution. *Archiv. f. Elektronik u. Ubertragungstechnik*, 32:159–164, 1978.

[33] E. Michielssen and A. Boag. A multilevel matrix decomposition algorithm for analyzing scattering from large structures. *IEEE Trans. Antennas Propagation*, 44(8):1086–1093, 1996.

[34] R. E. Mickens. *Difference Equations*. Chapman and Hall, 1991.

[35] R. Mittra. *Integral equation methods for transient scattering in Transient Electromagnetic Fields, L.B. Felsen Editor*. Springer Verlag: Berlin, 1976.

[36] J.-C. Nedéléc. *Acoustic and Electromagnetic Equations*. Springer, 2000.

[37] A. F. Peterson, S. L. Ray, and R. Mittra. *Computational Methods for Electromagnetics*. IEEE Press, 1998.

[38] G. Pisharody and D. S. Weile. Robust solution of time-domain integral equations using loop-tree decomposition and bandlimited extrapolation. *IEEE Trans. Antennas Propagation*, 53(6):2089–2098, 2005.

[39] S. M. Rao, D. R. Wilton, and A. W. Glisson. Elettromagnetic scattering by surfaces of arbitrary shape. *IEEE Trans. Antennas Propagation*, AP-30(3):409–418, May 1982.

[40] J. R. Rice. A theory of condition. *SIAM Numer. Anal.*, 3(2):287–310, 1966.

[41] V. Rokhlin. Rapid solutions of integral equations of scattering theory in two dimensions. *J. Comp. Phys.*, 86:414, 1990.

[42] B. P. Rynne. Stability and convergence of time marching methods in scattering problems. *IMA Journal of Appied Mathematics*, 35:297–310, 1985.

[43] B. P. Rynne and P.D. Smith. Stability of time marching algorithms for the electric field integral equation. *Journal of Electromagnetic Waves and Applications*, 4(12):1181–1205, 1990.

[44] B. Shanker, A. A. Ergin, K. Aygun, and E. Michielssen. Analysis of transient electromagnetic scattering from closed surfaces using a combined field integral equation. *IEEE Trans. Antennas Propagation*, 48(7):1064–1074, 2000.

[45] B. Shanker, A.A. Ergin, and E. Michielssen. The multilevel plane wave time domain algorithm for the fast analysis of transient scattering phenomena. *IEEE Antennas and Propagation Society International Symposium*, 1999.

[46] X. Q. Sheng, J. M. Jin, J. Song, and W. C. Chew. Solution of Combined Field Integral Equation Using Multilevel Fast Multiple Algorithm for Scattering. *IEEE Trans. Antennas Propagation*, 46:1718–1726, 1998.

[47] R. S. Varga. *Geršgorin and His Circles*. Springer, 2004.

[48] G. Vecchi. Loop star decomposition of basis functions in the discretization of the EFIE. *IEEE Trans. Antennas Propagation*, 47(2):339–346, February 1999.

[49] G. Vecchi, L. Matekovits, P. Pirinoli, and M. Orefice. A numerical regularization of the efie for three-dimensional planar structures in layered media. *Int. J. of Microw. and Mill. Wave Computer-aided Engineering*, 7:410–431, November 1997.

[50] P. De Vita, A. Freni, F. Vipiana, P. Pirinoli, and G. Vecchi. Fast Analysis of Large Finite Arrays With a Combined Multiresolution-SM/AIM Approach. *IEEE Trans. Antennas Propagation*, 54(12):3827–3832, 2006.

[51] S. P. Walker, M. J. Bluck, and I. Chatzis. The stability of integral equation time domain computations for three-dimensional scattering; similarities and differences between electrodynamic and elastodynamic computations. *International Journal for Numerical Methods in Engineering*, 15:459–474, 2000.

[52] D. S. Weile, G. Pisharody, N.-W. Chen, B. Shanker, and E. Michielssen. A novel scheme for the solution of the time-domain integral equations of electromagnetics. *IEEE Trans. Antennas Propagation*, 52(1):283–295, January 2004.

[53] D. S. Weile, B. Shanker, and E. Michielssen. An accurate scheme for the numerical solution of the time domain electric field integral equation. *IAntennas and Propagation Society International Symposium*, 2001.

[54] W. L. Wu, A. Glisson, and D. Kajfez. A study of two numerical solution procedures for the electric field integral equation at low frequency. *ACES J.*, 10(3):69–80, November 1995.

[55] A. Yilmaz, J. Jin, and E. Michielssen. TD-AIM: fast FFT-based time-domain integral equation solvers. *IEEE Trans. Antennas Propagation*, 2003.

[56] J. S. Zhao and W. C. Chew. Integral equation solution of maxwell's equations from zero frequency to microwave frequencies. *IEEE Trans. Antennas Propagation*, 48(10):1635–1645, October 2000.

[57] J.S. Zhao and W.C. Chew. Integral equation solution of Maxwell's equations from zero frequency to microwave frequencies. *IEEE Trans. Antennas Propagation*, 48(10):1635–1645, 2000.